Photophysical Characterization of Dynamically Linked Polymers for Self-Healing Applications

---

Dissertation

zur Erlangung des akademischen Grades

doctor rerum naturalium (Dr. rer. nat.)

vorgelegt dem Rat der

Chemisch-Geowissenschatlichen Fakultät

der

Friedrich-Schiller-Universität Jena

von

M.Sc. Mathias Micheel

geboren am 28. März 1989 in Gelsenkirchen-Buer

FRIEDRICH-SCHILLER-
UNIVERSITÄT
JENA

Gefördert durch die Deutsche Forschungsgemeinschaft im Rahmen des SPP 1568 „Design and Generic Principles of Self-healing Materials“.

Gutachter/in: 1. Prof. Dr. Benjamin Dietzek, Jena
2. Prof. Dr. Peter Gilch, Düsseldorf

Datum der Verteidigung: 13. März 2019

Table of Contents

List of Abbreviations

ACN	Acetonitrile
CARS	Coherent Anti-Stokes Raman Scattering
CV	Cyclovoltammogram
DAS	Decay Associated Spectrum
DCM	Dichloromethane
ESA	Excited State Absorption
FWHM	Full-Width-at-Half-Maximum
GSB	Ground-State Bleach
IC	Internal Conversion
ICT	Internal Charge Transfer
IR	Infrared (800 to 2500 nm)
IRF	Instrumental Response Function
ISC	Intersystem Crossing
IVR	Intramolecular Vibrational Redistribution
LE	Locally Excited State
LED	Light-Emitting Diode
NMR	Nuclear Magnetic Resonance
OAE	Oligo(arylene ethynylene)
PEG	Polyethylene Glycol
PMMA	Poly(methyl methacrylate)
PPE	Poly(phenylene ethynylene)
RET	Resonance Energy Transfer
SE	Stimulated Emission
SEC	Spectroelectrochemistry
TAAS	Transient Absorption Anisotropy Spectroscopy
TRANES	Time-Resolved Area Normalized Spectroscopy
TRES	Time-Resolved Emission Spectroscopy
UV	Ultraviolet (100 to 380 nm)
UV/Vis	Ultraviolet/Visible (380 to 800 nm)
VET	Intermolecular Vibrational Energy Transfer

List of Figures

Publications and Conference Contributions

Some of the results presented within this thesis have already been published in the following list of peer-reviewed journals or have been presented in the form of talks or posters at the designated conferences. Some results in this thesis were obtained during research projects in the course “MC1.3 Physikalische Chemie”.

Articles in peer-reviewed journals

1. **Micheel, M.**; Ahner, J.; Frey, M.; Neumann, C.; Hager, M.D.; Dietzek, B. Photophysics of a Bis-Furan Functionalized 4,7-Bis(Phenylethynyl)-2,1,3-Benzothiadiazole, a Building Block for Dynamic Polymers. *ChemPhotoChem*, **2019**, *3*, 54-60. https://doi.org/10.1002/cptc.201800149
2. Ahner, J.; **Micheel, M.**; Kötteritzsch, J.; Dietzek, B.; Hager, M.D. Thermally Triggered Optical Tuning of π-Conjugated Graft Copolymers Based on Reversible Diels-Alder Reaction. *RSC Adv.*, **2016**, *6*, 98221–98227. https://doi.org/10.1039/C6RA21536J
3. Ahner, J.; **Micheel, M.**; Enke, M.; Zechel, S.; Schubert, U.S.; Dietzek, B.; Hager, M.D. Directed Orientation of Oligo(Phenylene Ethynylene)s Using Ureas or Urethanes in Rod–Coil Copolymers. *Macromol. Chem. Phys.*, **2017**, *218*, 1700343. https://doi.org/10.1002/macp.201700343
4. Ahner, J.; **Micheel, M.**; Geitner, R.; Schmitt, M.; Popp, J.; Dietzek, B.; Hager, M.D. Self-Healing Functional Polymers: Optical Property Recovery of Conjugated Polymer Films by Uncatalyzed Imine Metathesis. *Macromolecules*, **2017**, *50*, 3789–3795. https://doi.org/10.1021/acs.macromol.6b02766

An up-to-date summary of the author’s publications can be found on ORCID (ORCID-iD 0000-0002-5017-3511).

Book Chapters

1. Ahner, J.; Bode, S.; **Micheel, M.**; Dietzek, B.; Hager, M.D. Self-Healing Functional Polymeric Materials. In *Self-healing Materials*; Advances in Polymer Science; Springer, Cham, **2015**; pp. 247–283. https://doi.org/10.1007/12_2015_333

Conference Contributions

1. Poster presentation. **Micheel, M**; Ahner, J.; Hager, M.D.; Dietzek, B. Self-healing of Conjugated Polymers by Reversible Imine Metathesis. *4th Doctoral Conference on Optics*. 2015
2. Talk. **Micheel, M**; Ahner, J.; Hager, M.D.; Dietzek, B. Self-healing of Conjugated Polymeric Materials. *Central European Conference on Photochemistry*. 2016
3. Poster presentation. **Micheel, M**; Ahner, J.; Hager, M.D.; Dietzek, B. Imine Metathesis as a New Pathway for Self-Healing Conjugated Polymers. *25. Lecture Conference on Photochemistry*. 2016
4. Invited Talk. **Micheel, M**; Ahner, J.; Hager, M.D.; Dietzek, B. Self-healing of Conjugated Polymeric Materials. *Institute of Physical Chemistry, Heinrich Heine University Düsseldorf*. 2016

Danksagung

Es kommt sehr selten vor, dass sich eine Doktorarbeit wie von Zauberhand ohne das Zutun vieler Leute selber schreibt. Leider war dies auch hier der Fall – oder doch eher glücklicherweise, denn es war mir eine Freude, mit den Leuten, die mir tatkräftig unter die Arme griffen, zusammenzuarbeiten. Diesen Leuten möchte ich hiermit meinen Dank aussprechen:

Zunächst muss (oder eher: will) ich Prof. Dr. Benjamin Dietzek für die Aufnahme in die Arbeitsgruppe, die fordernde Aufgabenstellung und die vielen tiefgehenden Fachgespräche danken. Das Vertrauen, das du mir entgegengebracht hast, hat mich zu dem Wissenschaftler gemacht, der ich jetzt bin – ehrlich gesagt bin ich mir unsicher, was das bedeutet. Ich denke, etwas Gutes.

Prof. Dr. Peter Gilch danke ich für die Zweitkorrektur und die tiefgehende Vorbereitung auf das Leben als Doktorand. Von dem Wissen, was ich in Düsseldorf angesammelt habe, zehre ich bis heute.

Ein ganz besonderer Dank gilt Dr. Johannes Ahner und Dr. Martin Hager für die erfolgreiche Kooperation im Rahmen des Selbstheilungsprojekts.

Den Werkstätten am IPHT und am IPC gebührt meine tiefe Dankbarkeit für das schnelle und kompetente Bearbeiten meiner dilettantischen Aufträge. Andreas Berger und Lutz Bach danke ich für ihre schnellen elekronischen Hilfsarbeiten, die ein ums andere Mal eine Messwoche retteten.

Besonders herzlich möchte ich mich bei den Mitgliedern der FA7 bedanken, die mir im besonderen Maße in allen Belangen innerhalb und außerhalb des Labors beistanden: Dr. Maria Wächtler, Dr. Martin Schulz und Dr. Denis Akimov. Dirk Müller gebührt ein gesonderter Dank für die vielen Stunden, die wir an etwaigen Spektrometerkalibrationen verbracht haben.

Auch bei allen anderen ehemaligen und momentanen Gruppenmitgliedern will ich mich erkenntlich zeigen, insbesondere bei meinem ehemligen Büronachbarn Dr. Maximilian Bräutigam, der mir eine schnelle Integration in die Gruppe erlaubte, sowie Dr. Joachim Kübel, von dem ich den Großteil meines Laborwissens erlangt habe. Ohne die Korrekturleser Sebastian Bold, Dr. Fisseha Bekele Legesse, Dr. Christian Reichardt, Kilian Schneider und Jens Tran wäre diese Arbeit wahrscheinlich noch fehlergespickter als sie ohnehin schon ist – danke dafür. Bei Ying Zhang bedanke ich mich herzlich für die Spektroelektrochemie in Kapitel 4 – Xièxiè! Auch bei allen Forschungspraktikanten – den Obsts, Jonas und Jooris, sowie Martha und Clara – will ich mich herzlich bedanken, es hat Spaß gemacht, mit euch zu arbeiten. Einen

speziellen Dank haben sich meine Bürokollegen Alex, Christian, Julian und Fisseha verdient, die diese Promotion erträglich gemacht haben. Danke, Jungs.

Zu guter Letzt will ich mich bei meiner Familie bedanken, die mich ja nicht mehr so oft zu Gesicht kriegt. Danke für das Vertrauen, das ihr mir entgegen bringt, und dass ihr mich in meiner Entscheidung, nach Jena zu ziehen, immer unterstützt habt. Und natürlich will ich mich bei Julia bedanken. Da du keinen schnulzigen Text möchtest (und dir immerhin schon zwei Musikalben gewidmet sind!), belasse ich es bei einem Dank fürs Korrekturlesen, das Verfassen des Absatzes über die Selbstheilung der Haut, sowie die Bereitstellung der Abbildungen 3.9 und 5.5. Ich liebe dich.

Nobody knows what entropy really is, so in a debate you will always have the advantage.

John von Neumann to fellow mathematician Claude Shannon

Chapter 1

Introduction

1.1 A Fatal Conclusion from Thermodynamics and its Solution

The second law of thermodynamics, which is one of the guiding principles of our macroscopic world, states in a definition given by Rudolf Clausius: "The entropy of the world strives towards a maximum." [1] In a very simple picture, as it is often used in a figurative sense, entropy can be seen as the degree of disorder in a system. The effects of this statement are all too obvious in our everyday life: once a glass bottle falls to the grounds it shatters, leaving dozens of shards of broken glass on the floor. The state of lower entropy – the intact glass – cannot be retained.

While unfortunate for somebody thirsting for a glass of water, the implications for industrial applications are of even graver consequence. Based on Clausius' statement and a popular version of Murphy's Law, "if something can go wrong, it will" [2], one could say: "Everything that can break will eventually break." Thus, as all man-made devices are susceptible to failure and breakage, the limiting factor for the lifespan of any device or tool is the time needed until one or all of its components lose their function. Even though this observation might be obvious, it needs to be explicitly stated, as it is the driving force behind all industrial and material science research. Ultimately, the goal of this research is to find new materials or methods, which prolong the lifespan of a given device.

Many materials are vital for a broad range of applications, but among all classes of materials, polymers have become one of the dominating. Because of the prevalence of these synthetic materials, some researchers even coined the term "polymer age" for the 20th and 21st century. [3,4] While initially only used as easy-to-process alternatives to natural resources, polymers have now found their way into every niche of civilization, from medical applications [5] to plastic electronics. [6] The development of increasingly more intelligent polymers, that will replace currently used materials, will only further fortify the leading role that polymers will play in the future. As such, prolonging the operating life expectancy of polymer based devices would ultimately result in an increase in their economic efficiency, as the interval between costly maintenance and partial or even complete replacement of components grows. Moreover, averting the decay of polymeric devices also has a huge ecological impact. In 2010, nearly 30,000 tons of plastic waste were produced world-wide, of which five to twelve thousand entered the

oceans [7], endangering maritime wildlife. Another study from 2013 estimated that by 2050, the world would hold 33 billion tons of plastic. [8] This is more than four times the combined mass of all humans that will have ever lived by then. [9,10] Longer-living polymer devices could in principle counteract this trend, as they lead to the generation of less waste.

So while the advantages of prolonging the lifespans of plastics are clear, how exactly does one proceed in doing so? The conventional approach employs more robust materials. In a very general sense, this approach is reflected in the early ages of civilization, when the advancement from the *stone age* over the *bronze age*

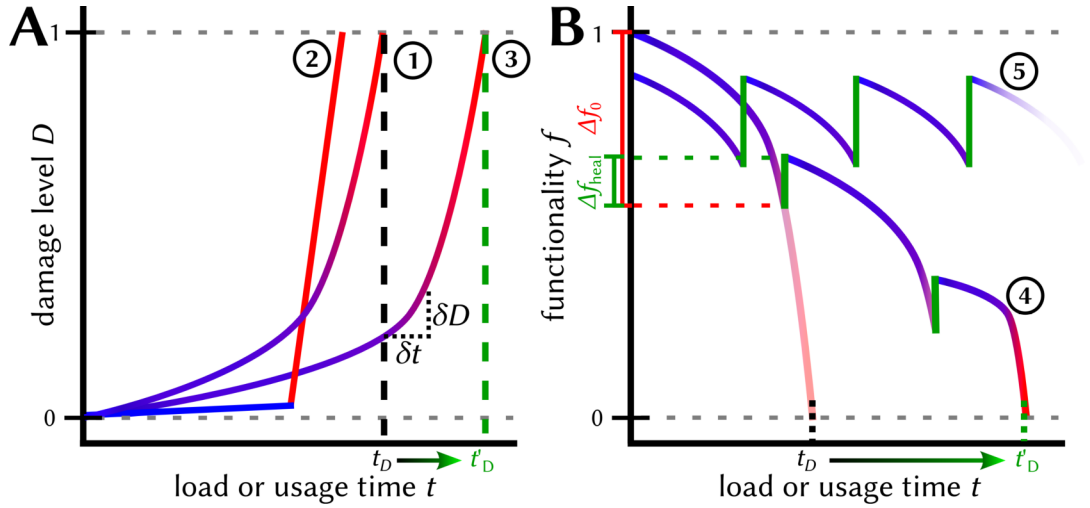

Figure 1.1: Comparison of the "damage prevention" and "damage management" design principles. (A) Damage level over time for three materials ①, ②, and ③ based purely on the prevention paradigm. The conventional material ① without enhancements breaks at the usage time t_D. Material ② has been reinforced, but its time of failure is ultimately smaller than that of ①. Material ③'s damage resilience has been improved, resulting in a higher usage time t'_D. In all three graphs, blue coloring indicates a small slope δD *vs.* δt, while red colouring stands for a big slope. (B) The change in functionality over time for self-healing materials ④ and ⑤. ④ is a material that is able to partially recover twice its functionality, resulting in an increased t'_D compared to the conventional material's t_D (indicated by the transparent line). The change in functionality of the damaged material Δf_0 and the healed material Δf_{heal}, which are used in the assessment of the healing efficiency η, are indicated at the abscissa. Ideal self-healing material ⑤ is able to infinitely recover its original functionality. Note that even though its initial functionality is lower that that of ④, its usage time is not influenced by the decrease in functionality. Figure partially based on similar figures in ref. [11].

to the *iron age* was driven by the respective name-giving material, which was more damage resilient than preceding one. More recently, a lot of work was done to improve the mechanical resistance to scratches on the surface or the tensile strength of polymer materials. Quantitatively, a mathematical description of this "damage prevention" [11] approach goes as follows: a material's performance is affected by the damage that was inflicted on it. The damage level D describes the relative extent of the accumulated damage due to load or simply due to usage time t, $D = 0$ for a virgin material and $D = 1$ for a material that has broken and would need replacement in a device. The material can now be characterized by two parameters:

- The time t_D at which the material breaks, $D(t_D) = 1$. Generally, the higher t_D, the better the material.
- The slope of the curve of damage over time, $\delta D/\delta t$. For classical materials, $\delta D/\delta t \geq 0$, since damage can only be accumulated and never be restored. More generalized, referring to the beginning of the chapter, the accumulation of damage reflects the increase in entropy of a given system. Thus, the change in entropy S is solely increasing, $dS \geq 0$. [12] A small slope is associated with a damage resistant material.

Three different examples following the "damage prevention" paradigm are displayed in Figure 1.1A to further illustrate these points. Material ① is conventionally designed, the curve of the accumulated damage is strictly monotonously rising up to the point of $D = 1$, failure of the material. In search of a more robust material, one might find material ②. Initially, its resistance towards damage is a lot higher than that of ①, but at some point, it quickly disintegrates (a practical example might be a rubber band which upon a certain accumulation of damage snaps and breaks). The smaller t_D makes ② the inferior material. On the other hand, material ③ exhibits a higher damage tolerance over its entire lifespan, even though it accumulates more damage than ② at early usage times. This is an important point to consider: in many research reports, only the initial value of a given functionality is indicated. However, evaluation of a material's performance has to keep the entire life cycle of a material in view and how the functionality changes over time.

1.2 From *Damage Management* to Self-Healing Polymers

Following the damage prevention principle led to an improvement of the lifespan of many devices. However, even in these improved materials, material failure is only a matter of time, as one can only design a material that is more resistant to damage, but not completely immune to it. A different approach, the "damage management" strategy [11], offers a different point of view on damaging events. Instead of

looking for ways to avoid damage, it aims at coping mechanisms to deal with the damage. In an everyday picture, this approach is very intuitive; we do not throw away a bicycle, when parts of it are damaged, but instead try to repair it and restore its original functionality. Even on the molecular scale, one can find many examples that follow this design strategy, namely self-healing mechanisms found in nature. Many natural materials are able to autonomously detect a damage and heal the damage. Examples of self-healing in nature include fissures in plant cells [13], fractures in bones [14], or natural cement used in Ancient Roman construction [15] (for an extensive overview of naturally occurring self-healing materials, see this recent review by Cremaldi and Bhushan [16]). Consequently, a lot of effort has been put into designing synthetic materials with bio-inspired self-healing capabilities. [13,16–19]

However, the transfer of naturally occurring self-healing mechanisms to synthetic materials is mainly hindered by two factors. First, these mechanisms, which have been brought to perfection in millennia of evolutionary progress, are too complex to be simply copied, too specialized to a specific environment to be generalized and to be used elsewhere, or proceed on timescales that might be considered uneconomic. [11,12,17] For instance, wound repair of damaged skin tissue is "one of the most complex biological processes that occur during human life." [20] The wound healing cascade involves different celltypes, which are highly specialized to their specific tasks and are precisely regulated by numerous effector proteins such as hormones, cytokines, or growth factors. In total, wound repair takes several weeks to be completed. [20,21]

The second factor is of thermodynamic nature. If damaging events cause an increase in entropy (*vide supra*), any healing event has to cause a decrease in entropy, as it increases the "orderliness" of a system. [12] This thermodynamically demanding condition has been described with the term "negative entropy". [17] As Erwin Schrödinger, who coined the term, noted in his book "What is Life?", negative entropy is nothing else than free energy ΔG. [22] The relationship between ΔG, the change of entropy ΔS, and the change of enthalpy ΔH is expressed by the Gibbs-Helmholtz equation:

$$\Delta G = \Delta H - T\,\Delta S \qquad \text{Eq. 1}$$

Here, T is the temperature. For any reaction to proceed, ΔG has to be negative. In natural systems, this is achieved *via* dissociation of chemical bonds, an exothermic ($\Delta H < 0$) process. [23] This exenthalpic contribution far outweighs the endoentropic process of order restoration, enabling the healing process. These chemical bonds are built up by external means, *e.g.*, light in the case of plants. [24]

In fact, all living beings have to uptake external energy to compensate for the "negative entropy".

In synthetic systems, the mechanism of energy distribution varies and depends on the underlying self-healing mechanism. Mainly, one classifies self-healing strategies by two criteria:

- Origin of the self-healing functionality. If self-healing is a material-inherent property, one speaks of intrinsic self-healing. If self-healing is achieved by reaction of or with another healing agent, one speaks of extrinsic self-healing.
- Autonomy of the self-healing event. Depending on whether the damage itself triggers the self-healing event or an external stimulus (heat, light, electric current, etc.) has to be applied, one differentiates between autonomous or non-autonomous self-healing.

No matter what the exact mechanism is, they all aim at decreasing the macroscale entropy S_{macro}, while increasing the net entropy of the system S_{net}. For instance, encapsulation of healing agents into polymers [25,26], ceramics [27,28], or metals [29,30] has become a prevalent approach towards self-healing. Once a crack disrupts the structural integrity of the material, these microcapsules also rupture, causing the release of the healing agents which then fills the rift in the material. As such, this approach is an example of an extrinsic (as self-healing is not a property of the material itself), autonomous (as the damage itself triggers healing) mechanism. The opening of the microcapsules contributes the entropy necessary for healing and re-organization of the material: on the mesoscale, the capsules are also aligned in a certain order. Destruction of said order delivers the entropic contribution S_{meso}, and if $S_{meso} > S_{macro}$, then healing occurs. [31] Of course, many other contributions to S_{net} may be of interest and have to be accounted for. [32,33] For instance, in polymer networks, the end-group and chain mobilities play crucial roles, as movement of polymer chains is restricted in solid matrices. [34] A measure of chain mobility of a polymer is its glass transition temperature T_g. At elevated temperatures, mobile chain ends are able to fill gaps induced by mechanical damages. Detailed discussions of the role of chain mobility in self-healing systems are available. [34,35] It has to be noted, that contributions of enthalpy have been rarely addressed in discussions on the thermodynamics of synthetic self-healing systems. Enthalpic contributions in self-healing systems might originate from reactive chain-ends, unoccupied supramolecular bonding sites, or reactive species generated during the damaging event. [35]

Having introduced this thermodynamic design challenge, the advantages of self-healing materials will be discussed next. In Figure 1.1B, the degradation curves of two materials with self-healing properties are displayed. Please note that here,

rather than the damage level D, the relative functionality f, $f = 1 - D$ is displayed.[1] Material ④'s performance is constantly degrading and, without any interference, would need replacement after time t_D. However, two healing events are triggered, greatly extending the lifetime of the material to t'_D. Quantification and assessment of the healing process is mainly delivered by two parameters:

- Number of healing events at a given location. Generally, the more healing events can be triggered, the better. In the case of capsule-based approaches, this is limited to a single healing event at a specific location, but the total number of healing events equals the number of capsules embedded. On the other hand, supramolecular mechanisms could be in principle used indefinitely.
- Determination of the healing efficiency η. It is calculated by comparison of the original, pre-damage functionality f_0, the functionality upon damage f_{damage}, and the functionality after healing f_{heal} (Eq. 2). [17] Normally, $0 \leq \eta \leq 1$, but there are reports of efficiencies exceeding 1, meaning that the healed material is even superior in quality than the virgin one. [36–39] In these reports, extrinsic self-healing mechanisms were employed. The rupture of, *e.g.*, microcapsules initiates the release of self-healing agents. These are able to fill microscopic gaps in the damaged material, which in turn makes the healed material even stronger than the original.

Both parameters are of equal importance and normally, η is given for each individual healing step.

$$\eta = \frac{f_{heal} - f_{damage}}{f_0 - f_{damage}} = \frac{\Delta f_{heal}}{\Delta f_0} \qquad \text{Eq. 2}$$

Let us now consider material ⑤. Its initial functionality is lower than that of ④ and it would under normal circumstances be considered the inferior material. However, it possesses infinite self-healing potential, $\eta = 1$, meaning that it can indefinitely restore its original functionality. As a consequence, it could in principle be used forever without restrictions – as such, it represents an ideal material.

1.3 Recovery of Functionality beyond Structural Integrity

The previous chapter, even though not explicitly stated, dealt with polymers that can heal mechanical damages. This reflects the current state of research, which is mostly occupied with the restoration of structural integrity of materials. However, many devices and materials exhibit functionalities, which decrease over time by

1 Healing efficiencies are almost exclusively calculated by directly looking at a material quality at a given time t Q_t, *e.g.*, its tensile strength, and comparing it to its original value Q_0. Then, $Q_t = f \cdot Q_0$.

different pathways, *e.g.*, photochemical or oxidative. For instance, in the field of optoelectronic devices, perovskite based solar cells have shown promising efficiencies, but their chemical degradation over time limits their implementation in industrial applications. [40] Similarly, organic optoelectronics can degrade photochemically [41,42], oxidatively [43], and thermally. [44] Ultimately, all these factors limit their operational lifetime, which has to be high in commercial materials. [45] Following the damage prevention approach, much work has been done to improve the stability of these devices. Introduction of a self-healing ability could in principle push the operational lifetimes even further.

However, healing of functionalities, *e.g.*, conductivity or optical activity, is still a relatively unexplored field, but is at the moment on the forefront of research on self-healing materials. This manifests in the publication of several review articles in recent years (for instance, Zhu *et al.* in 2014 [36], Ahner *et al.* in 2015 [47], Huynh *et al.* [48] and Ocheje *et al.* [49] in 2017, as well as Chen *et al.* [50] and Tan *et al.* [51] in 2018), which deliver an extensive overview of advancements in the field of materials that can restore functions beyond structural integrity, *e.g.*, conductivity.

In the field of self-healing photovoltaics, perovskite based solar-cells have been studied the most so far. Interestingly, all publications on this topic date back to 2016. Zhao *et al.* implemented a polyethylene glycol (PEG) scaffold into a perovskite based solar cell, improving its stability in very humid atmospheres due to the hydrophobic PEG chains: while the material initially degrades due to dissolution of the perovskite material, its initial properties are quickly restored once it is brought into a less humid atmosphere. The authors conclude, that hydrogen bonds between the perovskite material and PEG chains are responsible for the healing. These bonds quickly eliminate water molecules from the material, restoring the original perovskite. [52] Lang and coworkers demonstrated that perovskite cells have an inherently high resistance towards proton irradiation and can in addition autonomously heal radiation induced damages. [53] Nie *et al.* observed drops in the photocurrent of a perovskite based cell, which, when the solar cell was put in the dark, recovered to its initial value. [54] While the latter two cases technically count as self-healing, the recovery of function was phenomenological in nature and not (original) aim of the work.

Self-healing in organic optoelectronics, however, is even more at its infancy. Advances in the field of self-healing stretchable and semiconducting polymers have been summarized in a recent review article. [49] However, all the materials presented only show self-healing upon mechanical damage, while other commonly encountered damage sources, *i.e.*, photochemical and oxidative, could not be healed so far.

1.4 Spectroscopic Assessment of Self-Healing

Functional self-healing optoelectronics, while still in their infancy, are an emerging class of materials. However, the methodology in the self-healing community is equally nascent when it comes to their characterization. Reflecting the initial focus on recovery of structural integrity, most investigations in the field of self-healing relied (and still rely to this date) on optical microscopy to gain insight in healing events. Often, these experiments involve "scratch tests", *i.e.*, discrete cuts on the surface by a sharp knife, which are then subjected to the healing trigger. Microscopic images follow the healing process, at the end of which the scratch has vanished (or, if no healing occurred, has not vanished). Even though this approach allows for quantification of damaging and healing events, qualitative evaluations of self-healing experiments still prevail, simply showing microscopic images before and after healing. There have been efforts to design an experimental protocol, which delivers quantitative and reproducible results. [55–57]

As a matter of fact, the sole use of optical microscopy adds another problem, as highlighted by a recent study by Geitner and coworkers. [58] In their work, the authors presented a scratch healing test of an intrinsically self-healing polymer network, whose healing is monitored by two different methods, coherent anti-Stokes Raman scattering (CARS) and laser reflection microscopy. Notably, the CARS microscopic images revealed different stages of the healing process and different healing domains within the material, which would have simply been assigned to "(partially) healed" by means of the conventional microscopic approach. The introduction of new spectroscopic methods is thus expected to further the (molecular) understanding and facile assessment of the healing processes.

Vibrational spectroscopy, *i.e.*, infrared (IR) and Raman spectroscopy, is one of the spectroscopic methods which has already found wide acceptance within the self-healing community. [59] Its main advantages are that it is a non-invasive method and in addition allows for identification of the underlying self-healing mechanisms on a molecular scale. It has been extensively used to identify reaction intermediates in healing processes. [60–63] The Raman signal of the reactive bonds involved in the healing process, *e.g.*, double bonds used in Diels-Alder-based polymers, is traced as a function of damaging and healing time. Other spectroscopic approaches that have been employed so far are nuclear magnetic resonance (NMR) and broadband dielectric spectroscopy. [55] An overview of spectroscopic methods that have already found use in the study of self-healing materials is given in Figure 1.2.

Electronic *i.e.*, absorption and emission, spectroscopy is still relatively underrepresented in the field of self-healing material research. However, both would add valuable information on the systems under study: absorption spectroscopy reveals (indirect) information on structural integrity of materials on a molecular scale and can be used to quantify the concentration of an absorbing species, whereas emission spectroscopy is highly sensitive, possibly up to single photon detection, and can contain information on molecular surroundings of the emitting molecule. In particular in the field of organic electronics, these methods are already standard characterization techniques, so that their importance will grow once self-healing functionalities are incorporated in these materials. Some recent publications already hint at the power of UV/Vis spectroscopy for the detection of healing and damaging events. Ahner *et al.* implemented a histidine-like fluorescent marker in a self-healing system based on Zinc-histidine interactions. [64] The defective polymer network exhibited a decreased emission intensity, which increased again during the healing process. In a slightly similar approach, Gupta *et al.* demonstrated the crack-healing of a polymer by means of

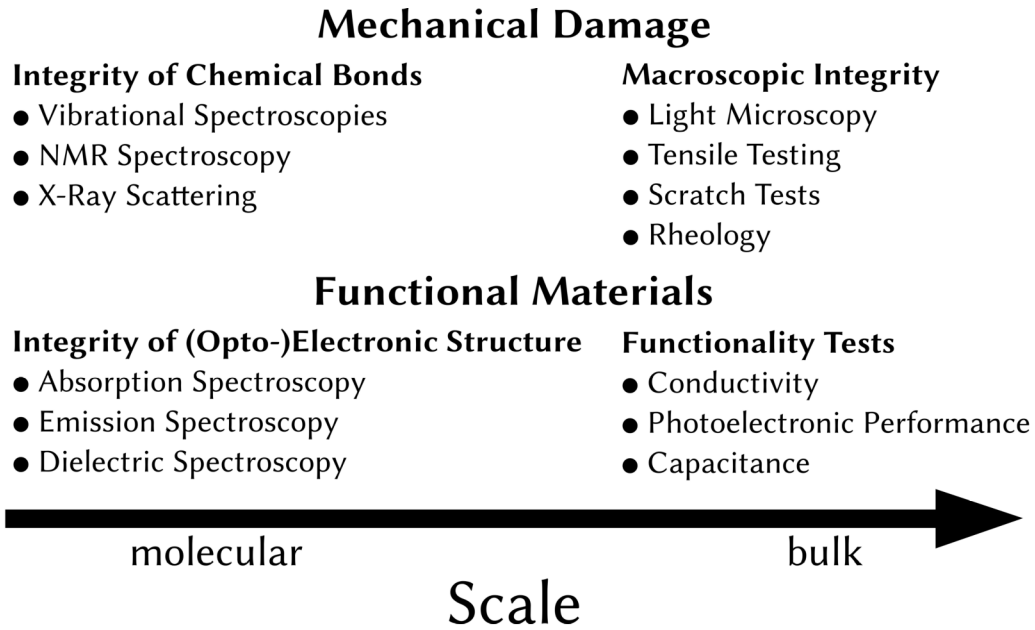

Figure 1.2: Spectroscopic methods currently employed in the research of self-healing materials. Here, these methods are qualitatively ordered by the scale they investigate and the class of materials they are used one. Note that these are not mutually exclusive to each other, as, for instance, vibrational spectroscopy might be used in the study of functional materials on larger scales by means of Raman microscopic methods.

CdS/CdSe nanoparticles. These particles autofluoresce and thus also indirectly serve as trackers of the healing process. [65]

Absorption has also already found extensive use to visualize self-healing – or rather the occurrence of damage. [66] Recently, an interesting approach using UV/Vis absorption in a self-healing material, that visualizes both the damaging as well as the healing event, was demonstrated in the group of Michael Kappl. [67] They designed a self-healing polymer based on microencapsulation of a healing agent and a dye, crystal violet lactone. While in the capsule, the dye is in an inactive form, *i.e.*, colorless, but as soon as it is released, it is converted in a form that shows strong absorption in the UV/Vis region ($\lambda_{max} \approx 600$ nm) due to interactions, *i.e.*, hydrogen bonds, with the outer shell medium. Next, the dye is converted again into its colorless form as it reacts with byproducts of the healing process. It has to be highlighted, though, that the change in absorption has only been used as a qualitative healing marker and no quantification of the healing process took place.

1.5 Dynamic Polymer Chemistry

The previous two chapters outlined examples of functional self-healing materials and how they are spectroscopically investigated. Next, a specific material class used in self-healing experiments is introduced. As outlined in 1.2, the number of possible healing events is one of the critical parameters in the design of self-healing polymers. Polymers exhibiting dynamic covalent bonds have already shown great potential for intrinsic self-healing, allowing for multiple healing cycles. [68,69] Jean-Marie Lehn, 1987 noble prize winner for his work on supramolecular chemistry [70], coined the term “dynamers” (*dyna*mic poly*mers*) for this class of material. [71] These polymers consist of repeating units, the unimers[2] [72], which are connected by reversible covalent or supramolecular bonds. These connections can be opened upon application of a trigger, e.g., heat or light, and the resulting “loose” unimers can reorganize. One differentiates in principle between three dynamer architectures: polymers with dynamic bonds in their main-chain, allowing for the design of dynamic copolymers; polymers with dynamic bonds attached to their side-chains, allowing for different kinds of functionalization; and polymer networks with multiple dynamic binding sites. [68,72]

Among the many reaction mechanisms in the field of reversible chemistry, Diels-Alder chemistry probably takes the top spot as the most often used one, in

2 The term unimer (from Latin *unus*, one, and Greek μέρος, *méros,* part) is used to contrast it with the commonly known term monomer (from Greek μόνος, *monos*, only). An unimer is the repeating unit of a dynamic polymer, but may consist of (non-dynamically bonded) oligomers.

particular with regards to self-healing. [73–75] In fact, it is probably also one of the oldest mechanisms in dynamic chemistry: its first use in a thermally reversible polymer network dates back to 1969 [76], making it an ancestor to Diels-Alder chemistry in currently utilized self-healing polymers. [77,78] The Diels-Alder reaction is a [4+2] cycloaddition, involving a diene (containing *four* conjugated π-electrons) and a dieneophile (a single carbon-carbon double bond with *two* π-electrons). The resulting Diels-Alder product is a six-member ring with one remaining double bond. Applying a different temperature can in turn trigger the retro-Diels-Alder reaction, which yields again the dienophile and diene educt. Accordingly, one can trigger healing of a damaged material, or more generally reshuffling of unimers within a polymer matrix, within different heating cycles. It is noteworthy that, even though Diels-Alder reactions can also be triggered photochemically, photochemical [4+2] cycloadditions are rare [79] and no example of them in the context of triggering self-healing is known to the author.

A field of research, which will prove vital in the design of functional intrinsically self-healing polymers, is the combination of dynamers and functional polymers. For instance, research on the introduction of optical properties, in particular fluorescence, into dynamers has been summarized under the term optodynamers [80], but it should be noted that the term is only rarely used outside the works of the group of Jean-Marie Lehn. The first investigation of an optodynamer was done by Ono *et al.*, who investigated the thermal exchange between two different, hydrazone-based, non-fluorescent polymers, one bearing a thiophene and the other bearing a phenyl moiety. [80] Superimposing two films of these polymers with catalytic amounts of pentadecafluorooctanic acid and subsequent heating at elevated temperatures produces emission in the domains of the superimposed films. This is due to rearrangement of the hydrazone-linked moieties, leading to a polymer with increased conjugation length, which fluoresces. While a few other examples of optodynamers are known [81], finding dynamic bonds which also change the optical properties of a polymer material remains an open field of work.

1.6 Outline of this Work

The previous chapters aimed at giving a rough outline on the current state of research on functional self-healing materials and dynamer chemistry, with a particular emphasis on optical properties deemed important for organic electronic devices. It is self-evident that all research on these topics is very much still in its infancy and their true potential has yet to be realized. This thesis addresses pressing questions on this matter, which up to now have remained open.

The crucial points tackled within this thesis are again schematically depicted in Figure 1.3. The structure of this thesis mirrors the three stages of self-healing experiments: (i) characterization of a virgin material (ii) characterization of a damage event and comparison of virgin and damaged materials and (iii) characterization of a virgin, a damage, and a self-healed material.

- In Chapter 3, the three most common dynamer architectures are characterized by their photophysical properties. In particular, their emissive behavior is investigated in detail and the relationship between polymer architecture and excited state dynamics unraveled. All conjugated polymers belong to the family of Arylene-Ethynylenes, highly fluorescent dyes with interesting excited state properties. Energy transfer studies and film characterization are central aspects of this chapter.
- Chapter 4 entails a detailed study on the photodegradation of a conjugated imine polymer, which contains different conjugated moieties commonly found in organic electronics. The importance of this study arises from the fact, that knowledge about degradation mechanisms is needed in order to tailor self-healing mechanisms. In this study, the influences of the solvent and different irradiation wavelengths on the photochemical pathways are analyzed.
- Finally, Chapter 5 presents a new optodynamer based on the imine metathesis reaction. For the first time, this mechanism is employed to induce an exchange between adjacent conjugated polymer chains. Utilization of this reaction mechanism leads to the first polymer, that can heal its conjugation, measured by the samples' absorbance, after it has been photochemically damaged.

This work aims at combining the fields of dynamic polymer and self-healing chemistry with conjugated organic molecules. The utilization of steady-state and time-resolved electronic spectroscopy aims at expanding the methodology currently employed in self-healing research.

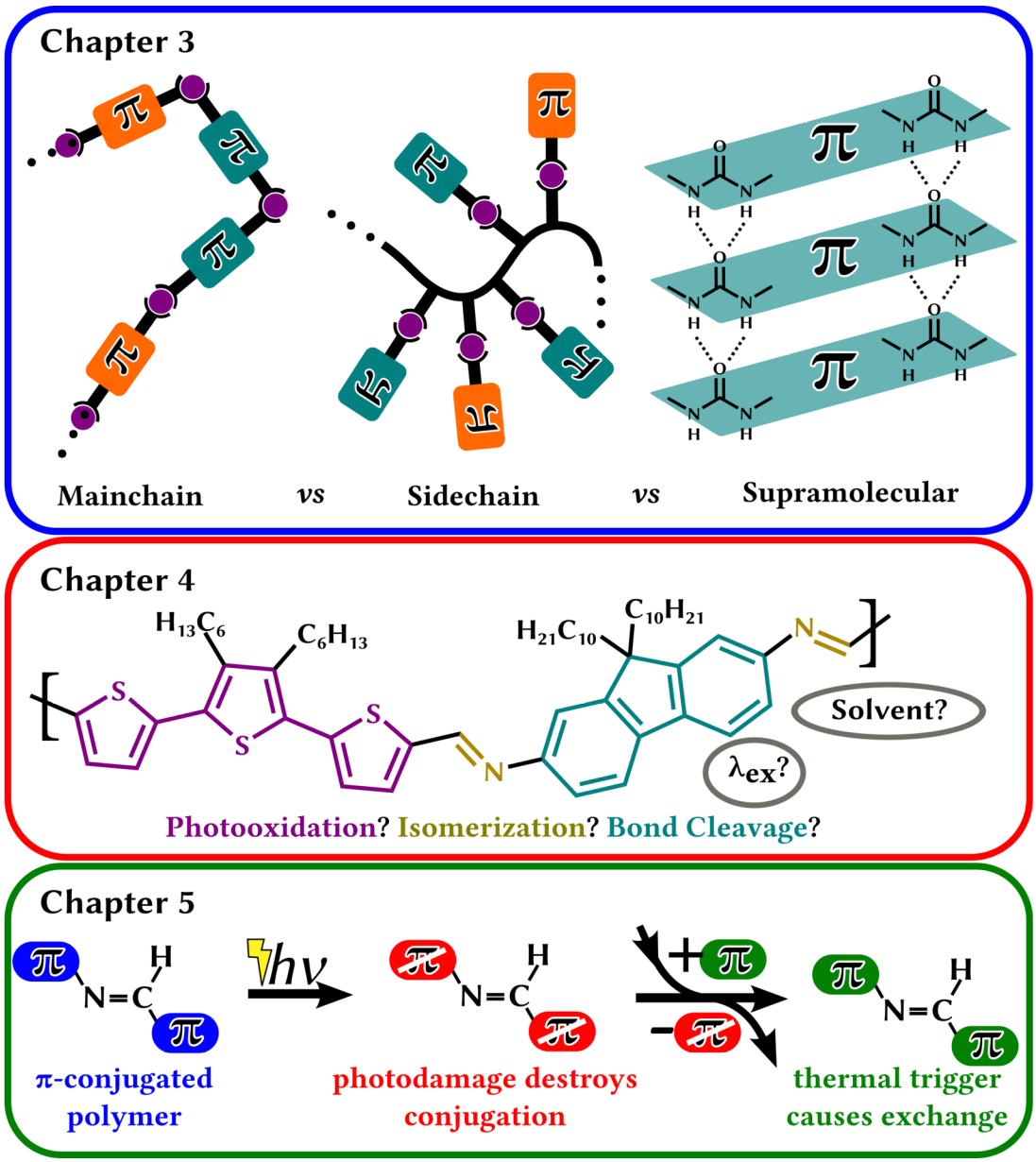

Figure 1.3: Schematic outline of this thesis' structure. In Chapter 3, three different dynamic architectures based on π-conjugated polymers are investigated with regards to their photophysics. In particular, their emissive properties will be thoroughly investigated. A case study on the photodegradation of a conjugated imine polymer is presented in Chapter 4. Finally, Chapter 5 introduces the first example of a conjugated polymer, that is able to restore its absorbance.

Chapter 2

Spectroscopic Methodology

UV/Vis spectroscopy, which covers a wavelength range of roughly 380-800 nm, is a powerful tool in studying the electronic and geometrical structure of a molecule, as its vibronic transitions[3] define its absorption and emission bands. Steady-state absorption spectra contain information on the electronic ground state, while emission and transient absorption spectroscopy are needed to decipher excited state properties, *e.g.*, the energetic levels or deactivation pathways of the electronically excited states. The sum of all photokinetic pathways, which eventually end again in the electronic ground-state, is called *photophysics* [79], whereas photoexcitation with the aim to yield a new chemical compound is called *photochemistry*. [82] For the purpose of this thesis, both terms are used interchangeably.[4] Knowledge about the timescale on which photophysical processes occur is vital, as the methods used to characterize these processes (and which will be described in the following sections) only deliver information on specific timeframes. The following sections will give a comprehensive outline on the processes relevant for this thesis, the timescales on which they occur, as well as the spectroscopic techniques employed in their investigation.

2.1 Timescales of Photophysical Processes

In general, processes following photoexcitation can be divided in those that cause an electronic state change and those that do not. Additionally, the state-changing processes can be further classified into radiative, causing an emission of a photon from an excited state, and non-radiative processes. Most of the processes upon photoexcitation described below generally obey a first-order rate law. Accordingly, the lifetime τ of a given excited state is defined as the time after which the concentration is reduced to e^{-1} of its initial value. For individual processes, it is more convenient to talk in terms of rate constants $k = \tau^{-1}$. In Figure 2.1, the majority of processes to be discussed in this thesis are displayed and ordered by their timescale.

3 A vibronic transition entails a change in both *vib*rational and elect*ronic* quantum numbers of a molecule.

4 The difference between both terms is (debatedly) purely semantic. Chemistry is the study of the reaction of one compound to another, which differ in their chemical and physical properties. The same could be applied to photoexcited molecules, which may behave very differently from their ground-state counterpart. The E/Z photoisomerism of a terminal unsubstituted alkene or photoacids illustrate this well.[83]

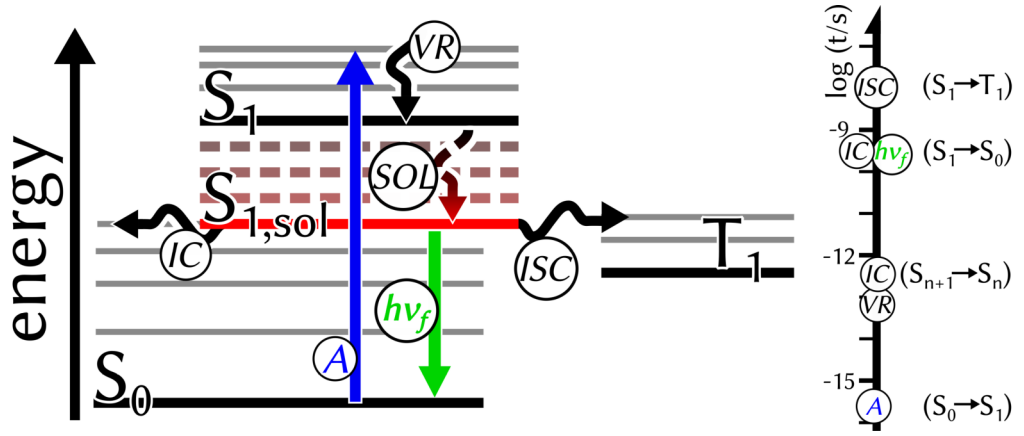

Figure 2.1: State diagram of the principal photophysical processes at the core of this thesis. Electronic states are highlighted in black and red, vibrational states in grey. Processes involving the absorption (A) or emission ($h\nu_f$) of a photon are depicted as straight lines, whereas the non-radiative processes of vibrational relaxation (VR), which entails intermolecular vibrational energy transfer (VET) and intramolecular vibrational redistribution (IVR) internal conversion (IC) and intersystem crossing (ISC) are shown as wavy lines. Additionally, dynamic solvation (SOL) from the original S_1 state (solid black) to the re-solvated $S_{1,sol}$ (solid red) state is shown. On the right, these processes are arranged according to the timescales typically found in organic molecules.

First, the processes, which do not result in a change of the electronic state involved, will be considered. Absorption of a photon, which occurs in under 10^{-15} s [79,84], results in the population of a vibrationally excited state of the electronically excited state. As the initially populated Franck-Condon state is sometimes called a *hot state*, the following processes are also often simply summarized under the term *cooling*. [84] This state is not in equilibrium with its environment and will dissipate its excess energy by different means. The exchange of energy with the surrounding medium, *i.e.*, the solvent, is called intermolecular vibrational energy transfer (VET). [85] The timescale for transferring a vibrational quantum from the excited molecule to the solution is in the order of vibrational periods of the molecule ν_{vib}. For instance, typical vibrational resonances exhibit wavenumbers ν_{vib} of ~100-3500 cm^{-1} [86], resulting in collision times with the solvent $t_{col} = (c \cdot \nu_{vib})^{-1}$ in the order of ~10-300 fs. Another possibility for vibrational relaxation is the intramolecular vibrational redistribution (IVR). Here, the energy localized in a high vibrational mode of the excited state is transferred to lower energy modes. The timescale for IVR for large chromophores (meaning larger than benzene) is in the order of 100 fs. [87]

Following the vibrational relaxation, the vibrational ground-state of an electronically excited state can be depopulated by many different decay channels,[5] which can be, as outlined above, classified into radiative and non-radiative pathways. Non-radiative pathways include internal conversion (IC), *i.e.*, the electronic transition between states of equal spin multiplicity, and intersystem crossing (ISC), *i.e.*, the electronic transition of states of differing spin multiplicity. Generally, the rate constant $k_{i\rightarrow f}$ for the non-radiative transition from an initial to a final state can be described by *Fermi's Golden Rule* (Eq. 3) [79,84], first coined by Dirac in 1927. [90]

$$k_{i\rightarrow f}=\frac{2\pi}{\hbar}\rho_f V_{if}^2 \qquad \text{Eq. 3}$$

Here, ρ_f denotes the number of vibronic levels of the final state, which match the energy of the initial state. Consequently, IC and ISC are isoenergetic processes. That is why they are sometimes called horizontal transitions, since they are displayed orthogonally to the energy axis in state diagrams.

The second term V_{if} is the vibronic coupling term between the initial and the final states [79], which includes a perturbation operator coupling nuclear to electronic motion and electron spin with orbital angular momentum for IC and ISC, respectively. However, for an estimation of the rate of these processes, one can much more easily rely on an empirically rule-of-thumb, based on the energy gap law. [91,92] It says that the rate of non-radiative processes k_{nr} decreases with an increasing energy difference ΔE between the two electronic states involved. This energy gap ΔE is usually determined by absorption and emission spectroscopy. For instance, ΔE in the case of the 0-0 transition is obtained at the intersection of the absorption and fluorescence spectra. One can derive the rate constant of IC k_{ic} (in s^{-1}) by inserting the energy gap (conveniently expressed in wavenumbers $\Delta\tilde{\nu} = \Delta E/hc$ and the unit μm^{-1}) into the empirically derived Eq. 4. For typical examples discussed in this thesis, $\Delta\tilde{\nu} \sim 2\ \mu m^{-1}$, resulting in $k_{ic}(S_1 \rightarrow S_0) \sim 10^{10}\ s^{-1}$.

$$\log(k_{ic}) \approx 12 - \Delta\tilde{\nu} \qquad \text{Eq. 4}$$

Rates for ISC k_{isc} are commonly around five orders of magnitude smaller than for IC in organic molecules.[6] This is due to the fact, that ISC is not mainly induced by electronic coupling as is IC, but by the magnetic coupling of the electron spin and the electron orbital motion. This *spin-orbit coupling* is only effective in the presence

5 Examples, in which vibrational relaxation quantitatively competes with other decay pathways, are early photophysics of ruthenium complexes (competition with ISC) [88] and ruthenium dye sensitized solar cells (competition with electron injection). [89] However, such cases are not relevant for this thesis and will not be further discussed.

6 There are examples of organic molecules baring heavy atoms (xanthones, nitroarenes), in which ISC occurs within picoseconds. [93,94]

of “heavy” (meaning atoms with a nuclear charge number $Z > 10$) atoms, as it is proportional to Z^4, or if the change in spin is accompanied by a change in momentum (El-Sayed rules). [94] ISC and triplet states only play a minor role within this thesis, so that no further explanation on their nature and the influences on their rate will take place.

As this sums up the discussion of non-radiative pathways, the radiative decay channels are discussed next. They comprise of fluorescence and phosphorescence, in which a photon is emitted under conservation and change in spin multiplicity, respectively. For the scope of this thesis, fluorescence is the only emissive pathway occurring. The emissive rate constant k_{em} can easily be estimated from the broad absorption spectra of molecules in solution. The most common method of calculating is the one derived by Strickler and Berg in 1962 [95]:

$$\frac{1}{\tau_{em}} = k_{em} = 2.880 \cdot 10^{-9} n^2 \frac{\int I(\nu) \mathrm{d}\,\nu}{\int I(\nu) \nu^{-3} \mathrm{d}\,\nu} \int \varepsilon(\nu) \mathrm{d} \ln \nu \qquad \text{Eq. 5}$$

Here, n is the refractive index of the solvent, $I(\nu)$ the emission intensity at the wavenumber ν, and ε the absorption coefficient. A simpler version of this equation is given in Eq. 6. Inserting the refractive index of the solvent n, the wavenumber of the absorption’s band maximum ν_{max} (in μm^{-1}) and the absorption band (with the molar absorption coefficient ε in $M^{-1}\,cm^{-1}$), integrated in the wavenumber region ν_1 to ν_2 yields a fluorescence rate constant k_f (in s^{-1}). [79] As absorption bands are often overlayed by other transitions, it might be helpful to consider either a mirror-image relationship between absorption and emission spectra or a Gaussian shape of the absorption band. A typical order of magnitude for k_{em} for chromophores discussed in this thesis is 10^9 to 10^{10} s^{-1}.

$$k_{em} = 2900\, n^2 \left(\nu_{max}\right)^2 \int_{\nu_1}^{\nu_2} \varepsilon(\nu) \mathrm{d} \ln \nu \qquad \text{Eq. 6}$$

In addition to all above mentioned processes, there are two more processes which are of high importance for the fate of eletronically excited states. The first is the photochemical reaction, either intra- or intermolecularly. Timescales for these reactive pathways cover many orders of magnitude, from several tens of femtoseconds (E/Z-isomerism in rhodopsin) [96] to hundreds of microseconds (reactive quenching of triplet states). [97] The photochemical pathways and their timescales will be discussed in more detail in the respective chapters of this thesis. The second process is of more fundamental importance, namely the dynamic solvation of the excited state. The change in electronic structure within a photoexcited molecule might induce changes into its electron density distribution. The solvent shell, however, is still oriented in the same way as when the solute was

in its electronic ground state. The solvent molecules will reorient their electric dipoles and the excited state of the solute will as a consequence be energetically lowered. [98,99] Typical solvation times for the solvents used in this thesis are in the order of picoseconds. [100]

How do all these processes now contribute to the excited state lifetime? First, it has to be emphasized, that according to *Kasha's rule*, all photochemistry stems from the lowest excited state of a given multiplicity (S_1 for singlet and T_1 for triplet states). [101] This finding is in line with the energy gap law: the energetic distance between excited states is smaller than that of the lowest excited state and the electronic ground state. Accordingly, IC between excited states proceeds with rates $k_{ic}(S_{n+1} \longrightarrow S_n)$ between 10^{12} to 10^{13} s^{-1} [84], several orders of magnitudes faster than $k_{ic}(S_1 \longrightarrow S_0)$. Thus, only the processes affecting the lifetime of the vibrationally relaxed S_1 or T_1 state will need to be discussed.

The excited state lifetime, or rather the rate by which an excited state is depopulated, is determined by the sum of the individual rates of processes contributing to its depopulation. In the case of the S_1 state, the lifetime τ_{S1} is determined by the sum of $k_{ic}(S_1 \longrightarrow S_0)$, $k_{isc}(S_1 \longrightarrow T_1)$, k_{em} and the rate of photochemical reactions k_{pc} (Eq. 7).[7] By inserting typical values derived above, singlet lifetimes in the order of nanoseconds are calculated.

$$\tau_{S1} = \frac{1}{k_{IC}(S_1 \rightarrow S_0) + k_{ISC}(S_1 \rightarrow T_1) + k_{em} + k_{PC}} \qquad \text{Eq. 7}$$

2.2 Absorption Spectroscopy

2.2.1 Steady-State Absorption Spectroscopy

All spectroscopic investigations begin with the recording of the steady-state UV/Vis spectrum of a compound. During a steady-state experiment, only a small part of the investigated sample is excited from its ground to its excited state. This can be rationalized by looking at the equilibrium steady-state constant K_{SS}, which is determined by the deactivation rate of the S_1 state and the excitation rate of the electronic ground state (Eq. 8). As discussed in 2.1, the deactivation rate is in the order of $(1\ ns)^{-1}$, and the rate of activation depends on the excitation power P_{ex} (in the order of mW or below) and the excitation wavelength λ_{ex}. Inserting values for the UV/Vis regime, $K_{SS} \leq 10^{-8}$. Thus, absorption spectroscopy solely addresses transitions from the electronic ground state and is the only method employed within this thesis to characterize the S_0 state.

7 In the absence of photochemical reactions, $k_{pc} = 0$.

$$K_{SS} = \frac{k_{S0 \leftarrow S_1}}{k_{S0 \rightarrow S_1}} = \frac{k_{deactivation}}{k_{excitation}} = \frac{10\,s^{-9}}{P_{ex}\,\lambda_{ex}/(h\,c_0)} \qquad \text{Eq. 8}$$

The absorbance A at the wavelength λ of a compound follows the Lambert-Beer law and is measured by comparison of the incident and transmitted spectral radiant powers P_λ^0 and P_λ, respectively (Eq. 9). [82]

$$A(\lambda) = \lg\left(\frac{P_\lambda^0}{P_\lambda}\right) = \varepsilon(\lambda)\cdot c \cdot d \qquad \text{Eq. 9}$$

It depends on the concentration c of the solution, the pathway of the cuvette (in most experiments presented in this thesis, d = 1 cm) and the wavelength-dependant molar absorption coefficient $\varepsilon(\lambda)$. In the determination of $\varepsilon(\lambda)$, a double-beam setup was used, *i.e.*, a cuvette with the pure solvent was measured simultaneously to account for absorption contributions of the cuvette and the solvent.

2.2.2 Illumination Experiments

In Chapter 4 and 5, solutions and thin spin-coated films of conjugated imine polymers were subject to steady-state illumination experiments in order to investigate their photodegradation. Two different light-emitting diodes (LEDs, Thorlabs) were used to illuminate the samples, one with λ_{ex} = 365 nm, P = 190 mW and the other with λ_{ex} = 455 nm, P = 900 mW. Samples were constantly stirred.

Quantum yields Φ_R for the consumption of the starting material were obtained using two separate experimental setups. In the first, samples were irradiated for set periods of time and absorption spectra were taken before and after each irradiation step. For the second setup, the kinetic measurement mode of the measurement program was used to follow the absorption changes at a set wavelength. Here, a glass filter (Schott, GG475) was used in the detection pathway to reduce stray light contributions from the LED. Most illumination experiments were conducted in the regime of total absorption, *i.e.*, the optical density of the samples was above 2 at the excitation wavelength, ensuring that 99 % of photons are absorbed. [102] The photoinduced absorption changes were recorded using a Jasco V-670 spectrophotometer. From plots of the absorption at this wavelength versus exposure time, an initial slope m was determined. Under the conditions applied this slope is proportional to the reaction quantum yield Φ_R according to Eq. 10.

$$\Phi_R = \frac{-m}{\varepsilon\,d}\,\frac{h\,c_0\,N_A\,V}{\lambda_{ex}\,P} \qquad \text{Eq. 10}$$

Hereby V is the sample volume, ε the absorption coefficient at the observation wavelength, h the Planck constant, c_0 the speed of light and N_A the Avogadro's number.

2.2.3 Transient Absorption Spectroscopy

Steady-state absorption spectroscopy delivers only information on the electronic ground-state, which is in a thermodynamic equilibrium with its surrounding, while no changes of spectral signatures in the time-domain can be visualized.[8] For the investigation of the fast excited state processes, it is necessary to instantly promote part of the investigated sample into its excited state. This can be achieved with the help of short laser pulses. Excitation of a molecule into its excited state puts it into a non-equilibrium state and, as discussed in 2.1, the deactivation of these electronically excited states may occur within picoseconds or even faster. In the thesis at hand, pump-probe spectroscopy is used to observe these fast processes.

The experimental setup used within this thesis is as follows. The fundamental generated from a titanium doped sapphire (Ti:Sa) laser[9] is split into two separate beams. The most intense one is used to generate the pump beam to excite the sample. Depending on the experimental conditions, *i.e.*, the electronic transition of the molecule to be targeted, it is generated in either of two ways: the first is the second harmonic generation of a 400 nm pulse by focussing the fundamental at 800 nm in a bariumborate crystal. [103] Alternatively, the beam is sent through an optical parametric amplifier, which is able to generate an excitation wavelength in a broad range. In this thesis, 370 and 400 nm excitations are most commonly used. For the probe beam, the other part of the fundamental is led over two delay lines (for a 2 ns window with fine steps and a 10 ns window with broader steps, respectively) and focussed in an eccentrically rotating CaF_2 plate to generate a supercontinuum (*whitelight*) in the range of 350–800 nm. [104,105] The plate has to be moved during the measurement to avoid degradation of the CaF_2 crystal. An attenuator and a moveable lens are placed before the supercontinuum generation to fine-tune the white-light properties. A portion of the probe beam is split and used as a reference beam in the data procession.

The relative polarization of the pump and probe beams is set to 54.7°, the so-called *magic angle*, to avoid signal artefacts due to rotational diffusion. This is realized by a Berek compensator in the pump path. Both beams are focussed at the sample position (the sample is located within a 1 mm flow-through cuvette to avoid the accumulation of photoproducts during the measurement) under a small angle, so that the pump beam after the sample is locally separated and can be blocked. The probe beam is recollimated and sent to the detection. Both the probe beam as well

8 Steady-state spectroscopy, namely emission spectroscopy, indirectly still contains kinetic information, though.

9 Fourier-transform limited pulses centered around 800 nm, pulse durations ≤ 100 fs, pulse energies ≥ 1 mJ, repetition rate 1 kHz.

as the reference beam are sent parallelly to the diode array, which is read out at the laser repetition rate.

The setup described in this thesis uses a two-pulse setup with a chopper in the pump path,[10] which is synchronized to half the repetition rate of the laser source. Thus, every second shot is blocked, so that the probe pulses hit the sample in a pumped (P_p) and unpumped (P_n) state. Additionally, before every scan (a scan entails the measurement of a complete set of spectra from about -50 ps to ~2 ns or ~10 ns, depending on the delay line used), P_{off} with both probe and pump blocked is recorded and subtracted from the measured spectra to account for ambient, *e.g.*, background light, and electronic noise. Moving the delay line allows measurements with different delays between pump and probe beam. The wavelength λ and delay time Δt dependant differential absorbance $\Delta A(\lambda,\Delta t)$ can then be calculated by Eq. 11. [106] Every dataset is the average of five to ten scans.

$$\Delta A(\lambda,\Delta t)=\log\left(\frac{P_{ref}(\lambda,\Delta t)-P_{off}(\lambda)}{P_p(\lambda,\Delta t)-P_{off}(\lambda)}\cdot\frac{P_{ref}(\lambda,\Delta t)-P_{off}(\lambda)}{P_n(\lambda,\Delta t)-P_{off}(\lambda)}\right) \qquad \text{Eq. 11}$$

The subscript *ref* denotes the signal by the reference beam. The differential absorption recorded can be analyzed analogously to the Lambert-Beer law (Eq. 9) in the presence of multiple absorbing species (Eq. 12). [79]

$$\Delta A(\lambda,\Delta t)=d\cdot\sum_i \varepsilon_i(\lambda)\cdot c_i(\Delta t) \qquad \text{Eq. 12}$$

Typically, it is assumed that the concentration is the only time-dependent parameter in a TAS experiment. [107] The obtained TAS dataset is a two-dimensional matrix M_{ij} with i time steps and j wavelengths. Inspection of $\Delta A_i(\lambda)$ delivers spectral information at specific delay times, while $\Delta A_j(t)$ contains kinetic information of the transient species. For a quantitative description of time-resolved datasets, global analysis methods based on Eq. 12 are applied (Eq. 13), *i.e.*, the dataset is reconstructed from a number of discrete species n, each with a characteristic decay associated spectrum $DAS_n(\lambda)$ and kinetic profile defined by their time constant τ_n. For a detailed explanation of the data fitting routine, see the doctoral thesis by Joachim Kübel. [108] Deconvolution with the instrumental response function (IRF) was neglected, since the first ~300 fs have been omitted from the analysis anyway due to the occurrence of coherent artefact signals as a result of the two short pulses interacting in a polarizable medium. [109] The model used assumes that the photophysical processes are subsequent and independent of

10 A four-pulse setup contains a chopper in the pump *and* the probe path, which also allows the detection of pump-only signals.

each other. The number of species n was varied until a satisfactory fit was achieved (as indicated by the residuals of the fitting procedure).

$$M_{ij} = IRF \otimes \sum_{n} DAS_n \cdot \exp\left(-t_j / \tau_n\right) \qquad \text{Eq. 13}$$

The decay associated spectra assist in the assignment of molecular processes occurring with the characteristic time constants τ_n. The amplitudes of $DAS_n(\lambda)$ can be either positive (meaning a decrease of signal) or negative (an increase of signal), due to the following processes (the sign of the amplitude is given in parentheses):

- ground-state bleach (-, GSB). The portion of molecules which have been excited does not contribute to the ground-state absorption anymore;
- stimulated emission (-, SE). The stimulated emission of a photon due to interaction of the whitelight with the excited state generates a negative signal, as more photons arrive at the detection than in the absence of emission;
- excited state absorption (+, ESA). Newly generated species, *e.g.*, excited singlet and triplet states, in the course of the deactivation dynamics are probed by the whitelight and exhibit different absorption characteristics than the electronic ground-state;
- photoproduct absorption (+). If a photoproduct is generated, it displays a positive absorption amplitude similar to ESA.

It is important to emphasize that the observed spectral amplitudes do not necessarily belong to one single species and mixtures of different processes are possible. Furthermore, the time constants describe the decay of $DAS_n(\lambda)$, and deliver no information on the state(s) which is/are generated in the course of the decay. For this purpose, one may look at species associated spectra [110], which has not been done in this thesis.

2.2.4 Transient Absorption Anisotropy

During standard TAS measurements, the polarization of pump and probe beam is adjusted to the magic angle to avoid measurement artifacts. Deliberately using not the magic angle, on the other hand, is useful to study the dephasing of the dipoles of the electornically excited states. The most common method is the investigation by means of transient absorption anisotropy spectroscopy (TAAS). [111]

In the setup used within this thesis, two probe beams are generated *via* a beamsplitter. During the experiment, single wavelength kinetics are recorded, in contrast to the whitelight used in TAS. The polarization of both beams is adjusted to be perpendicular to each other. This is achieved by leading one of the probe beams over two mirrors mounted to a periscope, which are tilted in a 90° angle towards each other. In the TAAS setup used, the pump beam is lead over a delay

line and its polarization is adjusted to be parallel to one of the probe beams. All three beams are focused at the same spot in the sample. The intensities of the probe beam parallel to the pump ($I_{\perp}$) and anti-parallel to the pump ($I_{\parallel}$) are collected independently from each other. The time-dependent anisotropy r(t) is then defined as

$$r(t) = \frac{I_{\parallel} - I_{\perp}}{(I_{\parallel} + 2I_{\perp})} \qquad \text{Eq. 14}$$

2.3 Emission Spectroscopy

2.3.1 Steady-State Emission Spectroscopy

Steady-state emission spectroscopy allows the investigation of the ultimately populated, *i.e.*, the fully vibrationally relaxed, re-solvated, lowest excited singlet state. Emission spectra of solutions were recorded in a 90° setup in high dilutions ($A_{max} \leq 0.05$), while spectra of films were recorded in front-face arrangements. In emission spectroscopy, two parameters are given in the characterization of compounds. The first is the Stokes shift $\Delta\tilde{\nu}$, which is the energetic difference (usually expressed in cm^{-1}) between the absorption and emission maxima. A small $\Delta\tilde{\nu}$ (< 2,000 cm^{-1}) is indicative of a very rigid and/or unpolar excited state, which undergoes only little energetic relaxation, while a large $\Delta\tilde{\nu}$ (> 3,000 cm^{-1}) is usually recorded in freely rotating excited state geometries with high dipole moments. [112]

The other important parameter is the emission quantum yield Φ_{em}. In principle, it describes the ratio of emitted to absorbed photons, but also contains kinetic information and sheds light on the emissive rate constant k_r and all non-emissive rate constants k_{nr} (Eq. 15). Emission quantum yields thus also quantify the competition between the emissive pathway and, *e.g.*, IC and ISC.

$$\Phi_{em} = \frac{k_r}{k_r + k_{nr}} = \tau_{S1} \cdot k_r \qquad \text{Eq. 15}$$

Emission quantum yields were measured in two different ways. The first procedure is the measurement of relative Φ_{em}. In this procedure, the fluorophore and a suited standard (in this thesis, quinine sulfate in 0.05 M H_2SO_4 with $\phi\Phi_{em,ref} = 0.53$) [113] are measured under identical experimental conditions. The relative quantum yield is then given as indicated in Eq. 16. Here, I is the spectrally integrated emission signal, A the absorbance at the excitation wavelength and n the refractive index of the solvent. The index *ref* denotes values for the reference sample. [114]

$$\Phi_{em} = \Phi_{em,ref} \cdot \frac{I}{I_{ref}} \frac{A_{ref}}{A} \frac{n^2}{n_{ref}^2} \qquad \text{Eq. 16}$$

The assessment of relative quantum yields is highly error prone, the absolute error of experiments being in the order of 0.1. Another, more reliable, setup was used in experiments conducted later during the experimental work of this thesis. Here, the absolute quantum yield of a sample was measured. This approach does not require the use of a standard. Instead, the sample emission and the emission of the pure solvent are measured under identical conditions in an integrating sphere. [115] By this approach, also quantum yields of films could be determined reliably.

Emission spectra were recorded at constant wavelength resolution. However, sometimes in this thesis, emission spectra are not plotted as a function of wavelength, but of the wavenumber $\nu = \lambda^{-1}$. For these cases, the emission intensity I(λ) had to be corrected by multiplication with λ^2 so that the integrals of spectra plotted against the wavenumber and wavelength remain identical (Eq. 17). [114]

$$\begin{aligned} &\int I(\nu)\,\mathrm{d}\,\nu = \int I(\lambda)\,\mathrm{d}\,\lambda \\ \Leftrightarrow &\int I(\nu)\,\mathrm{d}\,\lambda^{-1} = \int I(\lambda)\,\mathrm{d}\,\lambda \\ \Leftrightarrow &\, I(\nu)\cdot\lambda = I(\lambda)\cdot\lambda \\ \Leftrightarrow &\, I(\nu) = \lambda^2\cdot I(\lambda) \end{aligned} \qquad \text{Eq. 17}$$

2.3.2 Time-Resolved Emission Spectroscopy

TAS delivers information on excited state dynamics on the femtosecond to very early nanosecond scale. Time-resolved emission spectroscopy (TRES) is a convenient experimental method for the investigation of emissive states that live longer than ~1 ns.[11] In this thesis, a streak camera setup is exclusively used. Here, the frequency-doubled output of a Ti:Sa laser is frequency doubled to generate pulses centered at ~390 nm. The repetition rate of the fundamental is reduced to 400 kHz by a pulse selector. The excitation pulse is focussed in a sample in a 1 cm cuvette, the sample emission collected in a 90° geometry and spectrally dispersed on the detector. Again, the polarization of excitation and emission was set to a *magic angle* configuration. The incoming photons generate photoelectrons by means of a photocathode, which are subsequently accelerated and deflected onto a CCD camera. Streak-camera measurements thus deliver a temporally and spectrally resolved dataset. This is either globally analyzed (akin to Eq. 13) or spectrally integrated and the resulting single kinetic profile fitted with the fit program DecayFit. [116]

Sometimes, a method called time-resolved area normalized spectroscopy (TRANES) was used to analyze the datasets. [117] The approach used in this thesis slightly differs from the routine presented by Koti: emission spectra recorded at different times after excitation were simply normalized to their spectrally

11 With modern setups, accessing a time range of several femtoseconds is feasible.

integrated amplitudes and compared. This method is utilized to determine isolampsic[12] points, *i.e.*, the wavelength or wavenumber at which the total intensity of emitted light does not change [82], in multi-exponential decays.

2.3.3 Resonance Energy Transfer

Energy transfer processes play a huge role in many biological and artificial systems. One of the most ubiquitous is the Resonance Energy Transfer (RET), also known was Förster Resonance Energy Transfer, a non-radiative transfer of energy from a donor to an acceptor molecule based on the interaction of their dipoles. There are two conditions to be met for RET to occur. The first one is the overlap of the emission spectrum (normalized to its spectral integral) of the donor $I_D(\lambda)$ and the absorption spectrum of the acceptor $\varepsilon_A(\lambda)$ over the whole wavelength range. This is given as the spectral overlap integral $\mathcal{J}$ in Eq. 18.

$$\mathcal{J} = \int \varepsilon_A(\lambda) I_D(\lambda) \lambda^4 \, \mathrm{d}\lambda \qquad \text{Eq. 18}$$

The second requirement is close proximity of the donor and acceptor chromophore. The Förster radius R_0 (Eq. 19 for $[R_0]$ = nm) describes the distance between both at which the energy transfer efficiency $\eta_{RET} = 0.5$.

$$R_0 = 2.018 \cdot 10^{-2} \cdot \left(\frac{\kappa^2 \cdot \Phi_{em,D} \cdot \mathcal{J}}{n^4} \right)^{1/6} \qquad \text{Eq. 19}$$

Here, n describes the refractive index of the solvent, $\Phi_{em,D}$ is the emission quantum yield of the donor in the absence of an acceptor and κ^2 is a parameter describing the relative orientation of the donor and acceptor dipoles. Normally, $\kappa^2 = ⅔$ is assumed for freely rotating molecules. [114] Limitations of this assumption are discussed in Chapter 3.

As the distance r between both chromophores determines η_{RET}, RET experiments can also be used to measure the distance of two chromophores with known spectral overlaps. The molecular distance r can be obtained either by measuring the steady-state emission intensity of the donor in the absence and presence of an acceptor, I_D and $I_{D,A}$ (Eq. 20). TRES is the experimental method of choice. As the emission lifetimes, τ_D and $\tau_{D,A}$, do not depend on the sample concentration, the method minimizes experimental errors, and might also deliver more detailed information on the homogeneity of the donor-acceptor distribution.

$$\eta_{RET} = \frac{1}{1-(r/R_0)^6} = 1 - \frac{I_{D,0}}{I_{D,A}} = 1 - \frac{\tau_{D,0}}{\tau_{D,A}} = \frac{k_{RET}}{k_{RET} + k_{S1}} \qquad \text{Eq. 20}$$

12 While the term isoemissive is more often used, it does not refer specifically to light emission. [82]

Chapter 3

Dynamically Linked Oligo(arylene ethynylene)s

Oligo(arylene ethynylene)s (OAEs) are molecules, in which aromatic moieties are separated by C-C triple bonds. Depending on conjugation length and employed aromatic systems, this class of molecules is sometimes called Poly(arylene ethynylene)s, Oligo(phenylene ethynylene)s, or Poly(phenylene ethynylene)s (PPEs). Irrespective the exact molecular structure and name, these materials have become very interesting for use in optoelectronic applications: they possess high emission quantum yields, are conductive (and, due to their rigid structure, wire-like), and exhibit chromogenic behavior. [118] As such, they already found extensive usage as LEDs [119] or as bio- and chemosensors. [120] Combining these promising optoelectronic properties with dynamic chemistry could prove to be a versatile tool. For instance, polymer films with implemented dynamic functionality could change their optical properties even after being processed.

This chapter will deal with two categories of dynamers. First, main- and side-chain dynamers with incorporated chromophores are studied with regard to their photophysics. Furthermore, these chromophores can act as energy donors and acceptors in RET experiments and the influence on polymer structure on energy transfer efficiency will be discussed. In the second chapter, two polymers with different sites for intermolecular hydrogen bonding will be examined both in solution as well as in films.

3.1 Intramolecular Reversibility – Diels-Alder Optodynamers

The systematic approach in unraveling the photophysics of the Diels-Alder dynamers discussed in this chapter is as follows. First, the unimers are measured in solution (solvent: chloroform) and characterized in detail with regard to their photophysics. Next, the respective main-chain and side-chain homo-polymers are investigated, again in solution. In particular, the influence of the polymer architecture on the excited dynamics is discussed. What follows is an investigation of the optical properties of the polymers in thin spin-coated films. This sub-chapter concludes with the discussion of polymers, which incorporate both donor and acceptor unimers. For these hetero-polymers, RET studies were performed.

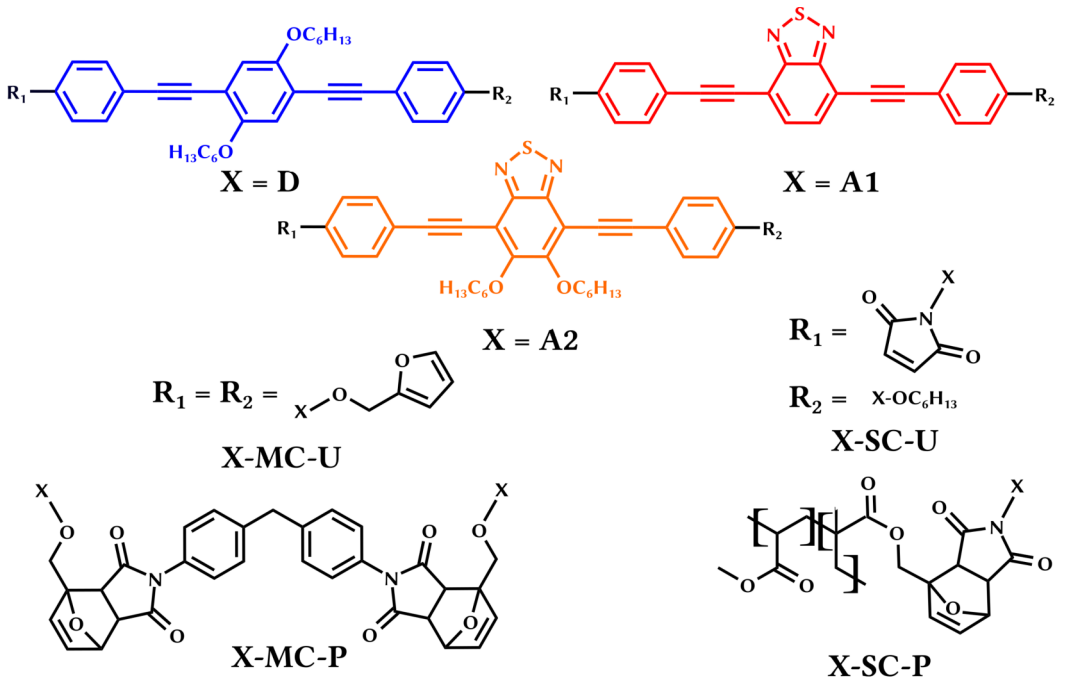

Figure 3.1: Dynamers and their respective unimers under investigation.

The compounds investigated within this chapter are depicted in Figure 3.1. Their nomenclature adheres to the system **X-Y-Z**, whereby **X** denotes a donor (**D**) or two different acceptor (**A1**, **A2**) chromophores, **Y** denotes the mono- (**SC**) or bis-furan (**MC**) functionalization needed in side-chain or main-chain architecture, respectively, and **Z** denotes whether the molecule at hand is a single unimer (**U**) or a polymer (**P**).

3.1.1 Investigations on Unimers in Solution

3.1.1.1 Steady-State Spectroscopy

First, all unimers were characterized by means of steady-state UV/Vis absorption and emission spectroscopy. The absorption and emission spectra are plotted in Figure 3.2. No pronounced difference between the mono- and bis-furan substituted chromophores was recorded. Both donor unimers **D-MC-U** and **D-SC-U** are characterized by a lowest-energy absorption maximum at ~370 nm with moderately high absorption coefficients $\varepsilon_{\lambda max} \approx 40 \cdot 10^3$ M^{-1} cm^{-1}. The absorption and emission spectra are not mirror-image spectra. In contrast to the relatively unstructured absorption spectrum, the emission spectra are characterized by a maximum at ~400 nm and a shoulder at ~420 nm. The lack of mirror symmetry, a finding which is in line with previously reported alkoxy-substituted OAEs [121,122], can be explained by a quick coplanarization of the phenyl rings into a single conformer in the excited state. A Stokes shift $\Delta\tilde{\nu} \sim 2300$ cm^{-1}, which is

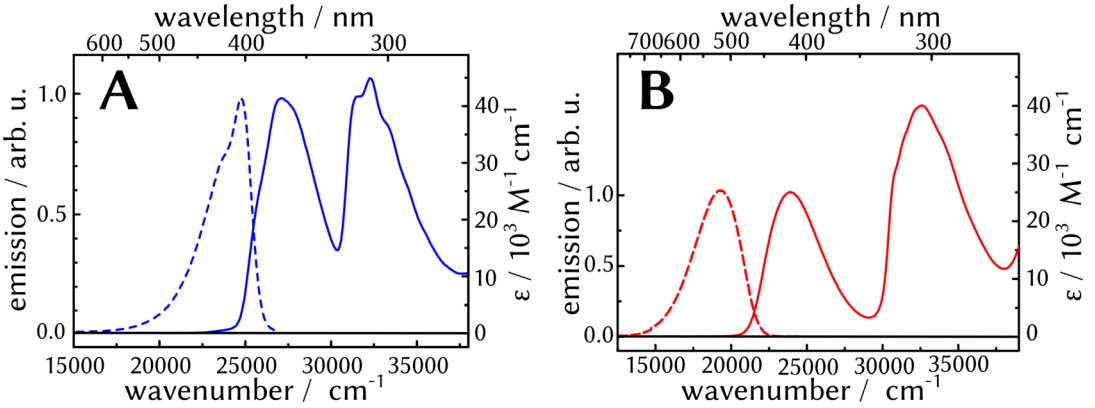

Figure 3.2: Steady-state UV/Vis characterization of unimers under investigation in chloroform. For (A) **D-MC-U** and (B) **A1-MC-U** the absorption coefficient (right scale) and the emission spectrum (left scale, normalized to the lowest energy absorption band) are representative for all investigated compounds.

in between the values reported for very rigid molecules, *e.g.*, fluorene ($\Delta\tilde{\nu} \approx 1400$ cm^{-1}) [112], and freely-rotating molecules, *e.g.*, bisphenyle ($\Delta\tilde{\nu} \approx 3300$ cm^{-1}) [112], further suggests a geometrical reorientation in the excited state. Both unimers also exhibit moderately high Φ_{em} in the order of 0.6.[13]

All three investigated acceptor unimers are also very similar with regards to their optical properties (Figure 3.2B and Table 3.1). The visible part of their absorption spectrum is characterized by a broad, featureless absorption band with its maximum centered at $\lambda \approx 420$ nm with a moderate absorption coefficient, $\varepsilon_{\lambda max} \approx 25 \cdot 10^3$ M^{-1} cm^{-1}. This value is comparable to methylacrylate-functionalized benzothiadiazol-ethynylenes. [124,125] All three compounds are strongly fluorescent with Φ_{em} near unity, which is larger than the value recorded for structural analogues. [124–126] Additionally, in contrast to the donor unimers, their emission spectra (centered at the maximum wavelength $\lambda_{em} \approx 520$ nm) are mirror symmetric to $\varepsilon(\lambda)$ with respect to the lowest energy absorption band and exhibit large $\Delta\tilde{\nu} \approx 4500$ cm^{-1}. A recent literature report by Ricci *et al.* attributes this behavior to the population of an internal charge transfer (ICT) excited state. [127] A detailed investigation on the solvent-dependence of emission follows later within this chapter.

13 The values for Φ_{em} for the side-chain unimers reported in ref. [123] were measured relative to a standard substance. The values reported within this thesis were measured using the integrating sphere method.

3.1.1.2 Time-Resolved Spectroscopy

The steady-state spectra revealed non-trivial excited state processes occurring in both donor and acceptor unimers. To investigate these dynamics, TAS and TRES were employed. In the case of TAS, only **D-MC-U** (λ_{ex} = 370 nm), **A1-MC-U**, and **A2-MC-U** (in both cases, λ_{ex} = 403 nm) will be discussed, while the discussion of time-resolved emission experiments (λ_{ex} = 390 nm for all experiments) entails also the side-chain unimers.

Donor Unimers

For donor unimer **D-MC-U** (Figure 3.3), a broad structured negative transient absorption signal between 350 and 460 nm is observed at early delay times. By comparison with steady-state absorption and emission data, this negative contribution can be assigned to overlapping contributions of GSB and SE. The rest of the transient absorption spectrum is dominated by positive absorption changes due to ESA which peaks at 590 nm. Both the positive and the negative absorption changes decrease in amplitude with increasing delay times. Transient spectra recorded at 1800 ps still exhibit negative contributions of GSB, but only marginal negative contributions in the spectral region, in which SE is expected, *i.e.,* below 500 nm. Furthermore, these negative contributions are also spectrally different from those at earlier delay times. In particular, the contributions from GSB and SE are spectrally more separated at longer delay times, as the peak position of SE gradually shifts to higher wavelengths with time, *i.e.*, from 402 nm at a delay time of 0.5 ps to 410 nm at 10 ps. Additionally, the ESA recorded at long delay times is much less structured than at early times and is characterized by a broad maximum between 550 and 600 nm.

A quantitative global analysis of the data using a three-exponential fit and an offset yielded τ_1 = 1.2 ps, τ_2 = 32 ps, and τ_3 = 1150 ps as characteristic time

Table 3.1. Steady state data on absorption and emission of the samples under consideration in chloroform. The molar absorption coefficient $\varepsilon_{\lambda max}$ at the lowest energy peak position λ_{abs} as well as the peak wavelength of fluorescence λ_{em} together with the fluorescence quantum yield Φ_{em}. In the last column, the predicted emissive lifetime $\tau_{em,SB}$ using a Strickler-Berg approach is given.

	λ_{abs} / nm	$\varepsilon_{\lambda,max}$ / M^{-1} cm^{-1}	λ_{em} / nm	Φ_{em}	$\tau_{em,SB}$ / ns
D-MC-U	369	$41.4 \cdot 10^3$	405	0.64	1.3
D-SC-U	372	$40.8 \cdot 10^3$	408	0.75	1.5
A1-MC-U	418	$25.1 \cdot 10^3$	512	0.99	2.7
A2-MC-U	424	n.d.	522	1.0	n.d.
A1-SC-U	428	$28.2 \cdot 10^3$	540	1.0	2.6

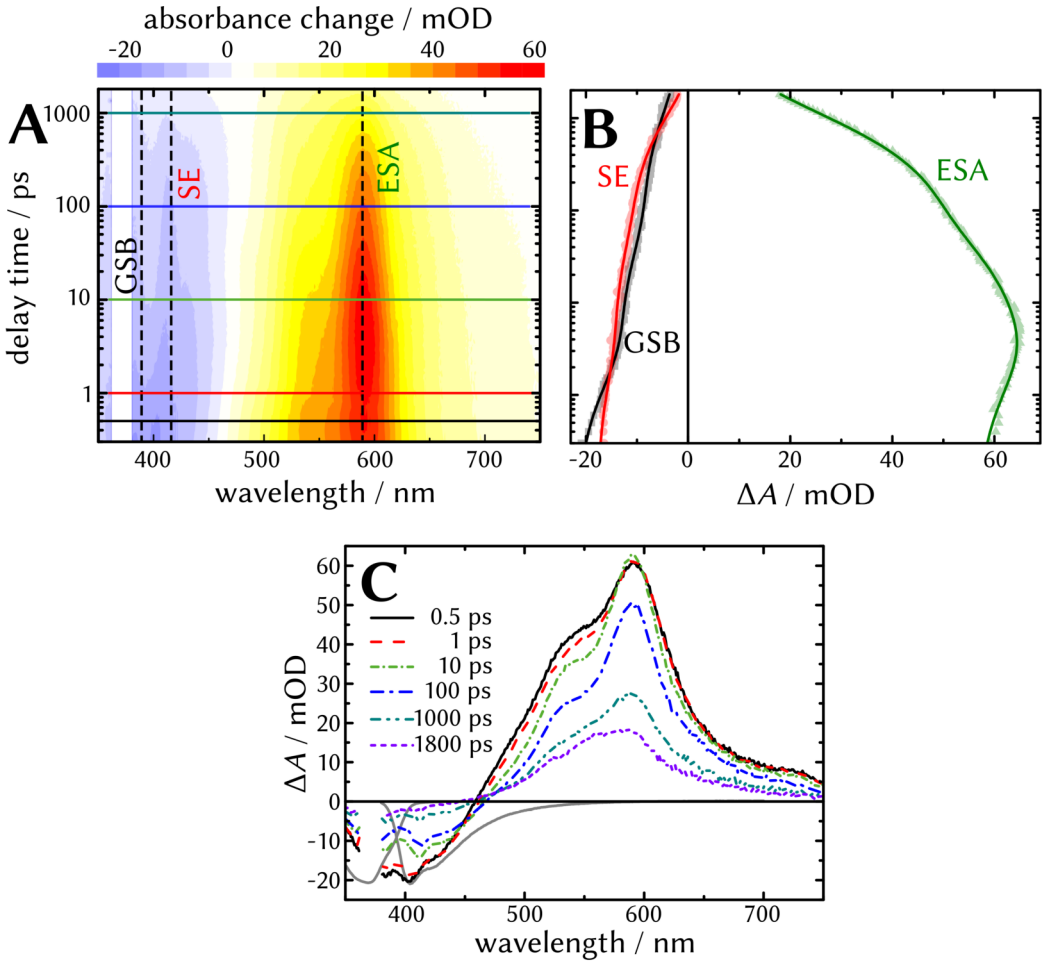

Figure 3.3: TAS of **D-MC-U** in chloroform upon 370 nm excitation. (A) The temporally and spectrally resolved signal intensity is visualized in a contour plot. Negative differential absorbance is indicated in blue, whereas yellow and red stand for positive changes. (B) Kinetic traces at selected wavelengths (as indicated in the contour plot). The spectral regions of the depicted kinetic profiles correspond to GSB recovery, and ESA and SE decay. The bold lines stem from a multi-exponential global fit of the data. (C) Transient spectra at selected times.

constants (Figure 3.4). The decay-associated spectrum $DAS_1(\lambda)$ associated with the short time constant τ_1 exhibits a negative peak at 402 nm and a local maximum at 413 nm. Such a sigmoidal pattern is often associated with relaxation processes [128] and the time-scale matches that, in which solvation of photoexcited molecules in $CHCl_3$ occurs. [98–100] $DAS_1(\lambda)$, thus, describes the shift of the SE to longer wavelengths due to vibrational relaxation of the excited state within the first ps after excitation. Another characteristic feature of $DAS_1(\lambda)$ is a sharp negative peak

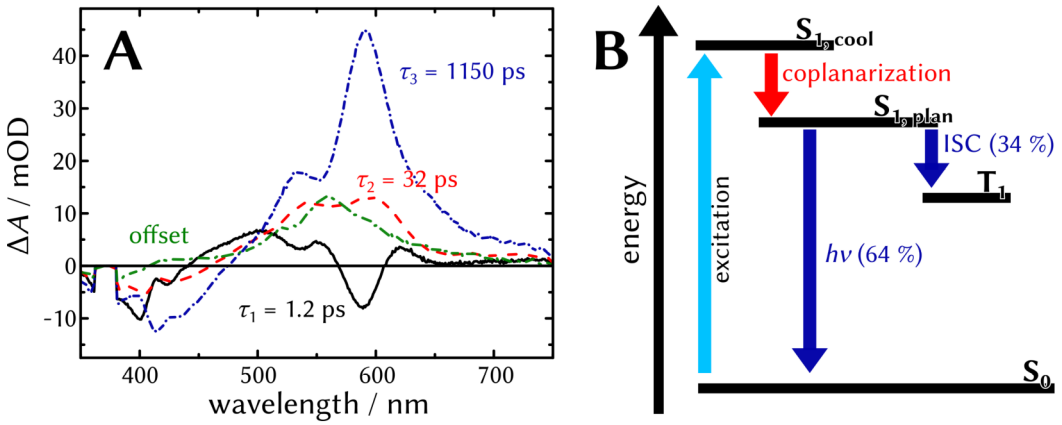

Figure 3.4: Excited state decay of **D-MC-U** recorded in chloroform upon 370 nm excitation. (A) Decay-associated spectra and corresponding time-constants as obtained from a global fitting routine. (B) Scheme summarizing the main photophysical processes of the excited state decay. The colours of the arrows correspond to the respective DAS.

at 590 nm which is surrounded by positive contributions. This describes a spectral narrowing and an increase of the ESA maximum.

$DAS_2(\lambda)$ is characterized by negative contributions below 460 nm, while two overlapping positive absorption bands centered at 540 and 600 nm can be seen. It mainly describes the shift of SE towards longer wavelengths. Previous reports on *bis*-alkyl- and *bis*-alkoxy-substituted OAEs observed similar spectral changes within tens of picoseconds after excitation, which were attributed to a coplanarization of the phenyl rings in the excited state. [121,129,130] Thus, the characteristic time constant τ_2 = 32 ps is within the expected range as judged from reports on related molecular systems.

Finally, the long time constant τ_3 = 1150 ps closely matches the value obtained *via* TRES, τ_f = 1.2 ns. In line with this observation, $DAS_3(\lambda)$ displays two overlapping negative bands centered around 370 nm (overlayed by scattered pump light) and 413 nm, coinciding with the maxima of the absorption and emission spectra. Thus τ_3 describes the recovery of the ground state from the fluorescent singlet excited state. **D-SC-U** decays on the same timescale with τ_f = 1.0 ns. This singlet lifetime is in excellent agreement with the predicted lifetime of the Strickler-Berg approach, which yields singlet lifetimes $\tau_f = \Phi_{em} \cdot \tau_{em,SB}$ 0.8 ns and 1.1 ns for **D-MC-U** and **D-SC-U**, respectively.

However, ground-state recovery by decay of the fluorescent singlet excited state is apparently not complete as indicated by the offset spectrum $DAS_\infty(\lambda)$, which exhibits a nearly identical spectrum to the transient spectrum recorded at 1800 ps. This offset spectrum, containing small contributions of GSB and an ESA with a

Table 3.2. Kinetic parameters of processes contributing to the excited state decay of the investigated unimers. The emissive rate k_{em} and non-radiative rate k_{nr} have been calculated using the time constant of the longest living emitting species. The rate of ISC k_{ISC} and IC k_{IC} have been calculated assuming no photoreaction depletes the excited singlet population.

	k_{em} (Φ_{em}) / 10^9 s^{-1}	k_{nr} / 10^9 s^{-1}	k_{IC} (Φ_{IC}) / 10^9 s^{-1}	k_{ISC} (Φ_{ISC}) / 10^9 s^{-1}
D-MC-U	0.53 (0.64)	0.30	0.02 (0.02)	0.28 (0.34)
D-SC-U	0.75 (0.75)	0.24	n.d.	n.d.
A1-MC-U	0.19 (0.99)	≪ 0.01	~0 (~0)	≪ 0.01 (~0.01)
A2-MC-U	0.24 (1.0)	~0	~0 (~0)	~0 (~0)
A1-SC-U	0.21 (1.0)	~0	n.d.	n.d.

maximum centered at 560 nm, closely resembles the triplet spectrum reported for *bis*-alkoxy-substituted OAEs. [130] Thus, the presence of the offset spectrum indicates the formation of the triplet state of **D-MC-U**.

By comparison of the GSB signal of DAS(τ_∞) with the initial bleach contained in the differential absorption spectrum ΔA(t = 0), a triplet yield can be estimated under the condition that triplet absorption does not play a role in the spectral region of the GSB considered in this evaluation. [131] As in the spectral window of GSB (350 – 380 nm) considerable contributions of ESA are present at early times, ΔA(t = 30 ps) has been used as the initial GSB of the excited singlet state, since ESA and GSB are more clearly separated at this delay time. Using this approach, a triplet yield for the donor monomers of Φ_{ISC} = 0.34 was estimated. This value is in line with values for triplet yields reported in literature for *bis*-alkoxy-substituted PPEs, which are in the order of 0.4. [130] ISC thus plays a major role in the deactivation of the initially populated singlet excited state at long delay-times. No further characterization of the triplet state decay was performed.

Acceptor Unimers – Early Photoinduced Dynamics

Both main-chain unimers **A1-MC-U** and **A2-MC-U** have been investigated by means of TAS (Figure 3.5). However, their excited state decays only differ slightly, so that the following description of the photoinduced dynamics refers to both chromophores if not noted otherwise.

A broad and structured negative transient absorption signal was recorded between 400 – 520 nm at early delay times. As this spectral region falls in the same range as the steady-state absorption and emission spectra, this negative feature is attributed to overlaying contributions of GSB and SE. Furthermore, a broad positive contribution due to ESA peaking at 650 nm was recorded. With increasing delay times, SE contributions seemingly disappear and eventually, due to superimposed

SE and ESA contributions, a local minimum at 560 nm appears, while the ESA increases at 750 nm, *i.e.*, the edge of our detection window.
A global analysis of the data yields four characteristic time constants and an offset. The time constants obtained for **A1-MC-U** are τ_1 = 0.9 ps, τ_2 = 6.2 ps, τ_3 = 270 ps, and τ_4 = 4820 ps (Figure 3.6A). The decay associated spectrum $DAS_1(\lambda)$ exhibits a

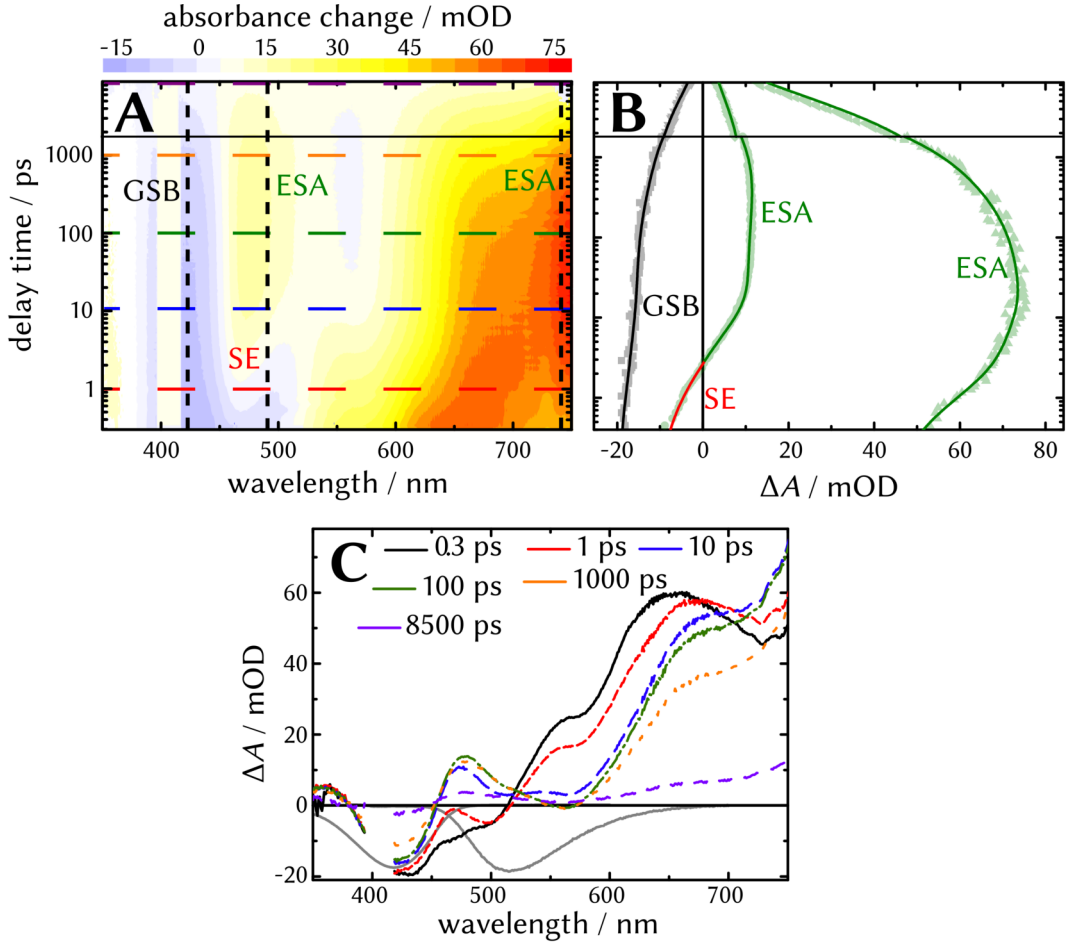

Figure 3.5: TAS of **A1-MC-U** in chloroform upon 403 nm excitation. (A) The temporally and spectrally resolved signal intensity is visualized in a contour plot. Negative differential absorbance is indicated in blue, whereas yellow and red stand for positive changes. Data for delay times greater than 1900 ps has been measured separately. (B) Kinetic traces at selected wavelengths (as indicated in the contour plot). The spectral regions of the depicted kinetic profiles correspond to GSB recovery, and ESA and SE decay. The bold lines stem from a multi-exponential global fit of the data. (C) Transient spectra at selected times. The steady-state absorption and emission spectra are additionally shown invertedly. Adapted from ref. [198].

negative peak at 460 nm and a local maximum at 620 nm with a zero-crossing at 500 nm. The spectrum and corresponding time-constant are associated with the vibrational relaxation of the initially populated hot excited state. $DAS_2(\lambda)$ exhibits comparable spectral changes, which are mainly characterized by a sigmoidal pattern in the spectral range of fluorescence, *i.e.*, a negative peak at 480 nm and a broad maximum at 600 nm and describes the shift of SE towards higher wavelengths. However, the time constant associated with this relaxation process is longer than one would expect for simple solvation (for chloroform, the average time constant for solvation is $\langle\tau\rangle$ = 2.8 ps) [100], but falls in the range of time constants describing the planarization of unsubstituted 1,4-bis(phenylethynyl)benzene. [132,133]

Thus, the process allocated with τ_2 is the coplanarization of the three phenyl rings in the excited state. This assignment is further substantiated by comparison of τ_2(**A1-MC-U**) with τ_2(**A2-MC-U**). In **A2-MC-U**, the central arylene is substituted with bulky alkyl chains. Accordingly, any rotational movement of this ring would be slowed down compared to the unsubstituted benzothiadiazole due to a higher moment of inertia and increased friction with the solvent surrounding. This is quantified by an increase in the coplanarization lifetime τ_2(**A2-MC-U**) = 11 ps > 6.2 ps (Figure 3.6B).

Acceptor Unimers – Decay of the S_1 state

Two time constants describe the decay of the coplanarized singlet state of **A1-MC-U**: both $DAS_3(\lambda)$ and $DAS_4(\lambda)$ are characterized by contributions of ground-state recovery, stimulated emission and the decay of the ESA. While qualitatively the same, the amplitude of these features is much smaller in $DAS_3(\lambda)$. TRES experiments further validate the presence of two decay processes of the coplanarized excited state with time constants $\tau_{em.1}$ = 0.3 ns and $\tau_{em,2}$ = 5.3 ns. A bi-exponential decay was also recorded for **A2-MC-U** $\tau_{em.1}$ = 0.2 ns and $\tau_{em,2}$ = 4.2 ns, whereas **A1-SC-U** decays mono-exponentially,[14] τ_{em} = 5.1 ns. It is noteworthy that a mono-exponential decay of the emissive state of **A1**, substituted for use in a side-chain architecture, has already been recorded by Breul *et* al. [134] However, it might be that the initial decay is simply too fast and occurs below the temporal resolution of the TRES setup.

As indicated in the discussion of steady-state spectra, benzothiadiazole-ethynylenes exhibit pronounced solvatochromism. Steady-state absorption and emission of **A2-MC-U**[15] recorded in different solvents reveal a pronounced solvent effect (Figure 3.7A): notably, the Stokes shift increases in more polar solvents, from

14 The emission decays of **A1-SC-U** and **A1-SC-P** have been reported to be mono-exponential. [123] Reevaluation of the data uncovered a biexponential decay for **P**, while the decay of **U** remained monoexponential.

4,000 cm^{-1} in toluene to nearly 5,000 cm^{-1} in acetonitrile (ACN). Additionally, solvent polarity seems to impact the emission quantum yield. While in the unpolar solvents chloroform and toluene, Φ_{em} = 1, the value decreases with increasing polarity to 0.97 (dichloromethane, DCM) and 0.89 (ACN). Furthermore, emission decay curves for **A2-MC-U** recorded in different solvents also reveal an influence of solvent polarity on the decay kinetics (Figure 3.7B). In the very unpolar toluene, a mono-exponential decay (τ_{em} = 3.4 ns) was observed. Going to the slightly more polar chloroform, the decay is now bi-exponential. In the even more polar DCM and ACN, the decay is again mono-exponential with time-constants of 4.0 and 4.4 ns, respectively. It is likely that their emission decay is also bi-exponential, but the first short time-constant is below the temporal resolution of the setup. In any case, the increase in Stokes shift and (long lived) emission life-time seems to be systematic (Figure 3.7B, inset).

In addition to the solvent-dependence of the emissive decay, the influence of temperature has been investigated as well (Figure 3.8A). TRES data were obtained for **A1-MC-U** in chloroform, methanol and toluene. The data recorded in chloroform reveal that the short time constant $\tau_{f,1}$ increases with decreasing temperature, whereas $\tau_{f,2}$ is temperature independent. Using an Arrhenius approach, an activation energy E_a = 8.4 kJ mol^{-1} was derived from the temperature dependent data. Temperature-induced changes on solvent polarity and viscosity have been neglected in this analysis. To account for these effects, the temperature dependent emission decay of the molecule was also recorded in methanol and

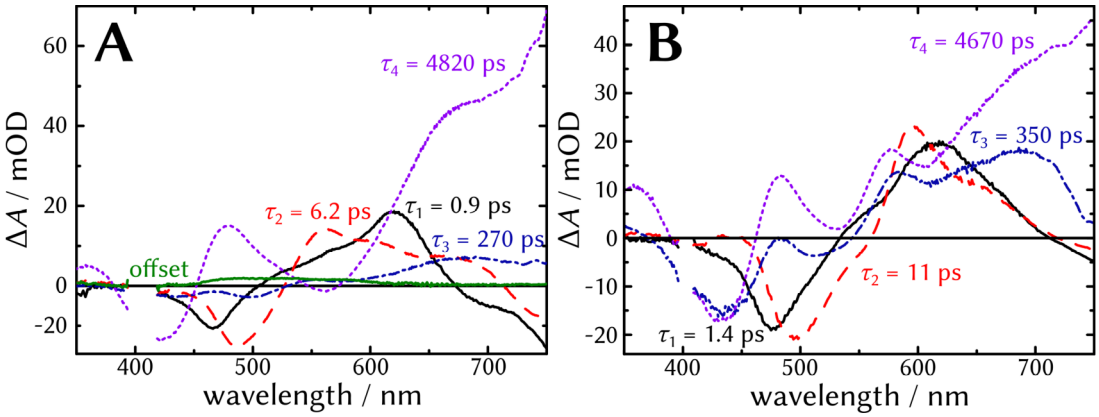

Figure 3.6: Decay-associated spectra of (A) **A1-MC-U** and (B) **A2-MC-U** recorded in chloroform. DAS with the same colour refer to the same photophysical processes in both chromophores, namely cooling (black), coplanarization (red), decay of the LE (blue), and decay of the ICT (purple). An offset, related to triplet absorption, was only observed for **A1**. Lifetimes for **A1-MC-U** from ref. [198].

15 **A1-MC-U** and **A1-SC-U** proved to be near unsoluble in most of the solvents used. Qualitatively, they exhibit the same solvatochromic behavior.

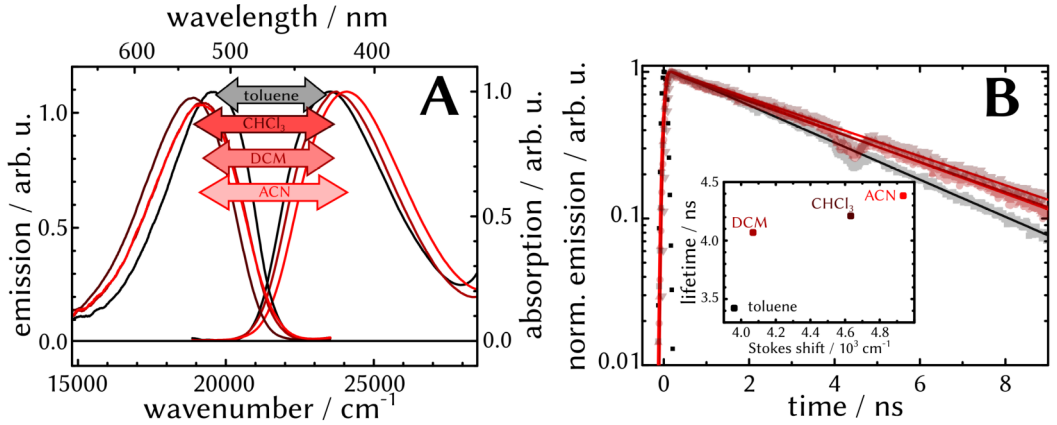

Figure 3.7: Solvent-dependance of emission and absorption of **A2-MC-U**. (A) Absorption and emission spectra recorded in different solvents. The arrows indicate the Stokes shift. (B) TRES measurements in different solvents. The offset plots the emission lifetime of the longest lived state *vs.* the Stokes shift.

toluene as examples of a highly polar and an unpolar solvent. In toluene, no multi-exponential decay could be recorded and the first-order emission decay appears to be independent from the temperature. In methanol, on the other hand, a complex behavior was recorded. For all temperatures, the decay is bi-exponential, and for temperatures below 230 K, a perfect agreement with an Arrhenius ansatz was recorded for the short time constant $\tau_{f,1}$ (the time constant $\tau_{f,1}$ is unaffected by temperature). The obtained activation energy in this temperature region (E_a = 10.0 kJ mol^{-1}) is in fairly good agreement with the value obtained in chloroform. Increasing the temperature, however, also led to an increase in the lifetime. The meaning of this "inverse Arrhenius" behavior is not clear and could not be resolved within this PhD thesis.

The solvent-dependence of the emission spectra and kinetics hints towards the population of an ICT state. In unpolar solvents such as toluene, the ICT state is energetically elevated and not reachable from the locally excited state LE. This is further evidenced by the emission lifetime as predicted by a Strickler-Berg approach: from the steady-state spectra of **A1-MC-U** recorded in chloroform, $\tau_{em,SB}$ = 2.7 ns was predicted, close to the value recorded in toluene (3.4 ns). The decay time recorded in toluene is thus probably the intrinsic life-time of the LE state. In more polar solvents, however, LE is readily quenched due to the population of a polar ICT state.

Additionally, the finding of an activation barrier quantitatively supports a (yet unproven) assumption from a literature report. Ricci *et al.* also found a four-step kinetic decay for a near identical benzothiadiazole. [127] Their interpretation of a

process on the 100 ps timescale includes a potential geometrical reorientation. The value for the activation barrier is in the same order of magnitude as activation energies for the rotational isomerism around triple bonds in the excited state. [135,136] Consequently, the formation of the ICT state might be accompanied by further planarization of the aromatic rings. This is further substantiated by comparison of the time constant associated with $DAS_3(\lambda)$ of A1 and A2: in the alkoxy-substituted A2, a slightly longer lifetime was recorded, as one would expect for rotation processes.

Last, the decay of the excited state of **A1-MC-U** seems to be incomplete within 10 ns, indicated by an offset spectrum $DAS_\infty(\lambda)$. This is again assigned to the population of a triplet state, but with a lower efficiency than in the donor unimers. Based on the emission quantum yield Φ_{em} = 0.99, the yield for non-radiative processes Φ_{nr} = (1- Φ_{em}) =0.01 puts an upper limit to the ISC efficiency Φ_{ISC} in **A1-MC-U**. The reason for this might lie in the nature of the transitions involved: the electronically excited S_1 state of benzothiadiazoles presumably has (π,π^*) character [127,137], the same as the lowest energy triplet state T_1. [138] ISC between states of same orbital type are forbidden (and thus slow) as dictated by the El-Sayed rules. [79] Notably, no triplet spectrum was recorded for **A2-MC-U.** As the non-radiative yields are low for all acceptor unimers, ISC is expected to play

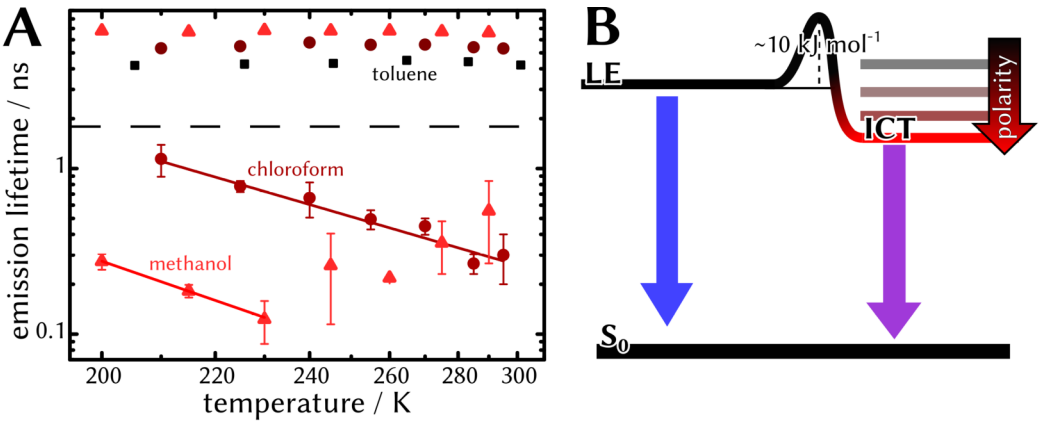

Figure 3.8: Temperature dependence of the emissive decay of **A1-MC-U**. (A) Temperature-dependent emission lifetimes obtained in different solvents. Values below the black dashed line were obtained using a biexponential decay model. For chloroform and methanol (for temperatures below 230 K), a fit according to the Arrhenius equation is plotted as a solid line. (B) State diagram depicting the excited state decay. The internal charge transfer state ICT is only populated from the locally excited state LE in polar solvents. Its energetic position depends on solvent polarity. Both states near-exclusively decay *via* fluorescence.

only a minor role in all of them. A scheme summarizing the solvent dependent photophysics of **A1-MC-U** as a model for all benzothiadiazoles investigated is depicted in Figure 3.8B.

3.1.2 Influence of the Polymer Architecture

As the unimers and their photophysics have now been explored in detail, the influence of incorporating them into a polymer backbone is studied next. Notably, no major changes in the spectral behavior between unimers and the respective polymers could be recorded, with absorption and emission maxima at virtually the same wavelength. In the case of main-chain dynamers, slightly lower $\varepsilon_{\lambda,\max}$ (referring to moles of chromophores in the polymer) were recorded. Calculation of $\varepsilon_{\lambda,\max}$ for the side-chain polymers is not as straightforward, as the number of chromophores attached to the Poly(methyl methacrylate) (PMMA) backbone is statistical. An upper and lower limit of the (methyl methacrylate)-to-chromophore ratio was calculated by means of ^{1}H-NMR spectroscopy and UV/Vis absorption spectroscopy. In the latter case, it was assumed that attachment of chromophores as a side-chain has no effect on the oscillator strength, as was observed in similar systems. [124,125] For **D-SC-P**, this ratio is between 4.3:1 (NMR) and 6.4:1 (UV/Vis) and for **A1-SC-U** it is between 3.3:1 (UV/Vis) and 4.3:1 (NMR).

For all polymers, a decrease in Φ_{em} was determined. This decrease in emission intensity is for the acceptor polymers (with the exception of **A2-MC-P**) additionally accompanied by a reduction of the emission lifetime. TAS measurements on **D-MC-P**, **A1-MC-P** and **A1-MC-P** revealed that all processes, which lead to the population of the final emissive state, remain unchanged in their kinetic behavior. Polymerization apparently only influences the longest living state. A similar behavior has already been observed when attaching chromophores as a side-chain to an aliphatic polymer backbone. [125,134]

Rate constants for emission, $k_{em} = \Phi_{em}/\tau_{em}$, and for non-radiative decay channels $k_{nr} = (1 - \Phi_{em}/\tau_{em})$ were calculated (Figure 3.9). For all systems investigated, k_{nr} of the unimers is lower than that of the polymers, whereas k_{em} remains mostly unchanged. This finding is in line with the “loose bolt” concept: introducing flexible substituents to a chromophore promotes non-radiative decay channels. [139] As no increase in Φ_{ISC} was observed in the polymer systems (as deduced from the TAS data), IC seems to be enhanced in the polymers and now takes part in the excited state depopulation. The extent of this effect varies based on the chromophore and the polymer architecture used: For **D-SC-P**, k_{nr} is doubled compared to **D-SC-U**, whereas only a 33 % increase was recorded for **D-MC-P**. Even though the relative increase is more pronounced in the donor side-chain system, $k_{nr} \approx 0.4 \cdot 10^9\ s^{-1}$ was found for all donor systems investigated. The same rate constant was found in a

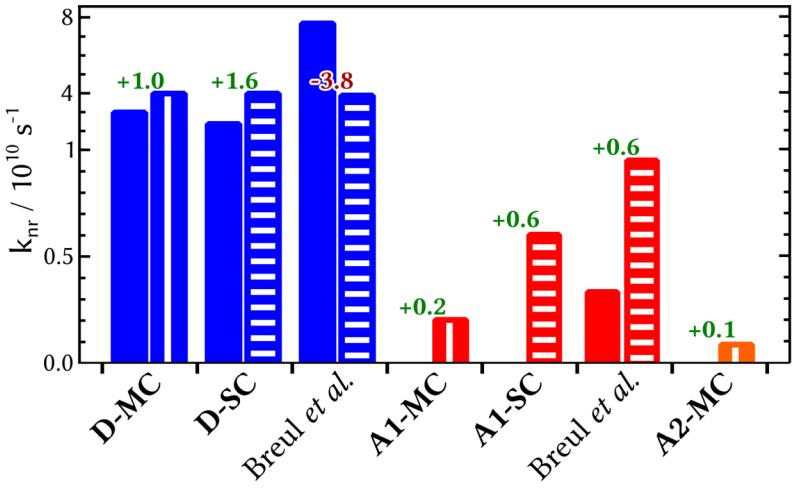

Figure 3.9: Non-radiative rate constants for unimers and dynamers under consideration. Fully filled bars refer to unimers, horizontal stripes represent side-chain architectures, and vertical bars represent main-chain architectures. Data on side-chain polymers from a literature report [134] has been included as well. Numbers above the bars indicate the change in the rate when going from the uni- or monomer to the respective polymer. Note that the different scale of the y-axis before and after $1 \cdot 10^{10}$ s^{-1}.

literature report on an irreversibly linked side-chain polymer. [125] It has to be noted that in this literature report, the non-radiative rate in a polymer actually decreased in contrast to the findings presented within this thesis. The nature of this different behavior remains an open question.

For the acceptor chromophores, the increase of the non-radiative rate constant is even more pronounced in the side-chain polymers: k_{nr}(**A1-SC-P**) is three times higher than k_{nr}(**A1-MC-P**) and five times higher than k_{nr}(**A2-MC-P**). The increase of non-radiative pathways in all polymers can be explained by the "loose bolt" concept [139]: the introduction of flexible substituents leads to increased non-radiative yields. For the side-chain polymer, the non-radiative rate increases more than for the main-chain ones. Apparently, the side-chain architecture allows for (comparatively) more rotational freedom of the chromophores, whereas embedding them into a polymer main-chain more rigidly restricts their movability.

3.1.3 Probing the Solid State

For any implementation of polymers into a device, their optical properties in the solid state, which might differ immensely from those in solution, have to be studied as well. With this in mind, thin films of all polymers have been studied with regards to their optical properties. Due to the differing solubilities of the

polymers, the procedure of film making was different for the films: **A1-MC-P** was dropcasted from highly concentrated chloroformic solutions, while the remaining polymers were dropcasted from chlorbenzene. Chlorbenzene is generally considered to be beneficial to film-formation and allows for higher ordered structures. [140]

In principle, polymer films exhibited very similar absorption properties as measured in solution (Figure 3.10). The main difference between solid-state and solution spectra is a broadening of the lowest energy absorption band of several 100 cm^{-1} for the films. This is in line with previous reports on PE films, which observed similar broadenings in OAE films (see, for instance, Chapter 3.2.2). The exact origin of this broadening is not clear. Chromophore aggregation is unlikely to have occurred, as OAE aggregates would show as sharp and distinct peaks in the absorption spectrum. [141] As these are absent, any electronic interaction between chromophores in the ground-state seems to be negligible.

In contrast to this, the excited-state behavior of all solid-state samples changed drastically. All polymers showed broad emission bands, that are bathochromically shifted by ~1,000 cm^{-1} compared to solution spectra. Additionally, emission is quenched in all films, resulting in lower quantum yields in the order of ~0.1 for acceptor polymers and ~0.01 for donor polymers. Emission spectra of polymer films containing A1 or A2 are overall very similar to each other, irrespective of the polymer structure: all show broad emission with an emission maximum at ~550 nm. However, the emission quantum yield of **A1-MC-P** is about 40 % smaller than for

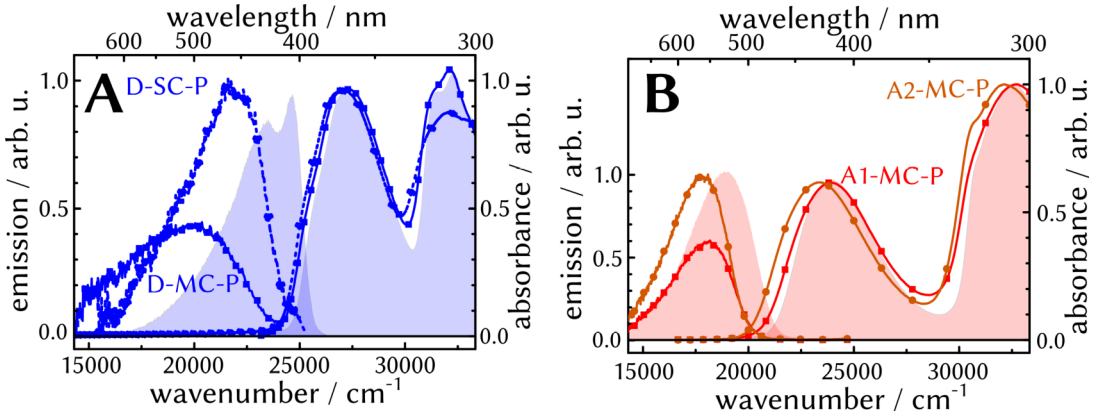

Figure 3.10: Steady-State UV/Vis spectra of dynamer films. For (A) the donor dynamers and (B) the acceptor dynamers, the steady-state spectra of **D-SC-P** and **A2-MC-P** in chloroform have been added as shaded areas, respectively. The spectral integrals of the emission spectra have been normalized to their respective emission quantum yields. The Spectra for **A1-SC-P** have been omitted for clarity, as they are very similar to **A2-MC-P**.

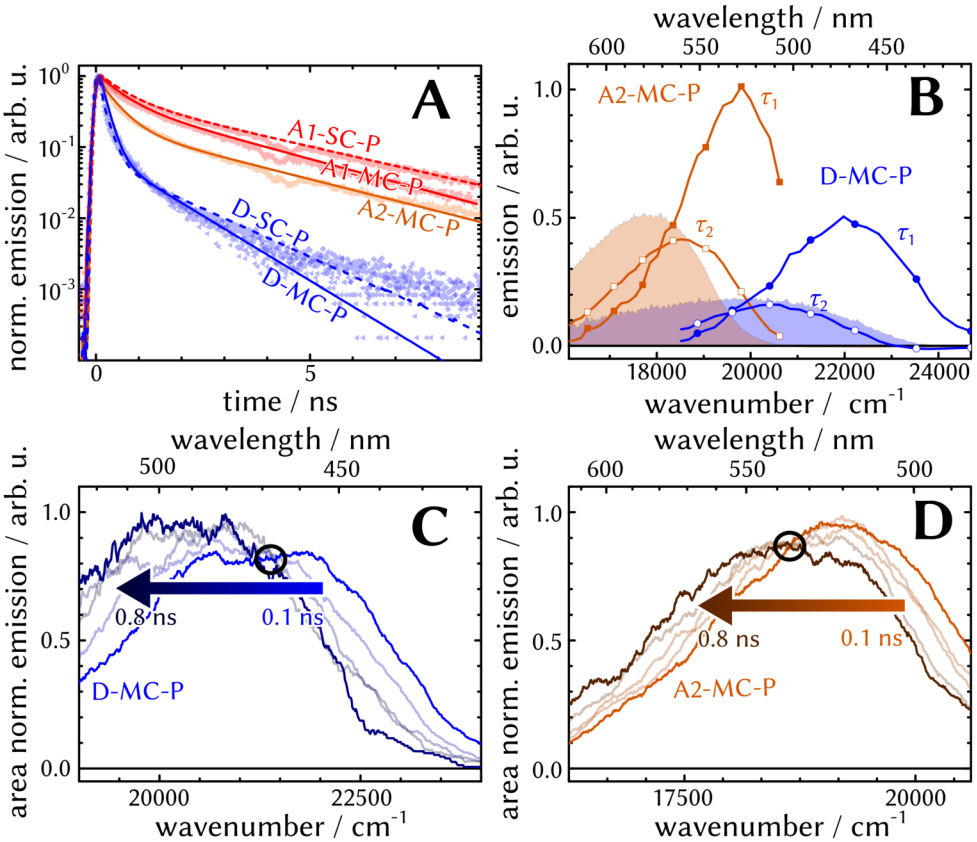

Figure 3.11: TRES measurements of dynamer films. (A) Emission decay curves recorded upon 390 nm excitation. The solid lines stem from a biexponential fit. (B) Emission spectra as obtained from a global fit using two time constants. The steady-state emission spectra of the respective polymer has been added as a shaded area. (C and D) TRANES spectra of a film of (C) **D-MC-P** and of (D) **A2-MC-P** within the first 0.8 ns after excitation. Black circles indicate isolampsic points, arrows the time-dependant shift of emission spectra.

the other acceptor polymers. A possible explanation might lie in the different solvents (chloroform and chlorbenzene), from which films were dropcasted: as already stated earlier, chlorbenzene is considered the superior solvent, as it evaporates more slowly and allows for polymer films with higher order. This might influence the quantum yield. The emission dependence of the dropcasting solvent has not been further investigated.

Donor containing polymers show a completely different behavior: while their emission quantum yields are similarly low, the spectral shape of emission differs. For **D-SC-P**, emission is narrow and has a maximum at ~460 nm, whereas emission

of **D-MC-P** films is bathochromically shifted ($\lambda_{max} \approx 500$ nm) and broader. In particular, the emission of the side-chain polymer is reminiscent of the emission spectrum recorded in solution. For all films, the emission spectrum was independent of the excitation wavelength and excitation spectra recorded at different emission wavelengths were basically identical. Thus, all emission seems to stem from the same chemical species.

TRES measurements revealed that the emissive decay in all polymers includes the decay of two spectrally different species. The longer-lived species, which decays with lifetimes of $\tau_{em,2} \approx 1$ ns, is bathochromically shifted compared to the short-lived ($\tau_{em,1} \approx 0.2$ ns) by ~1,000 cm^{-1}. TRANES revealed an isolampsic point in the emission decay. For **A1** and **A2** containing polymers, $\lambda_{iso} \approx 540$ nm, and for those that contain **D**, $\lambda_{iso} \approx 460$ nm. The occurrence of an isolampsic point indicates a two-step emissive decay of the initially populated state in contrast to the decay of two independently emitting species. The reduced Φ_{em}, the huge Stokes shift and the bi-exponential emission decay all point towards the formation of an excimeric state. The short-lived species is, based on the spectral similarity to emission recorded in solution, associated with the emission of a single chromophore, whereas the longer lived emission stems from excimers. Different structures of the excimers are feasible: Both intrapolymer, meaning interactions from chromophores within the same polymer chain, as well as interpolymer interactions might be considered. Based on the experimental results, these two cases can not be differentiated.

It was also tried to investigate excimer formation in main-chain polymers *via* TAS measurements. Interestingly, only films made out of chlorbenzene solutions proved to be stable enough to be investigated under an inert atmosphere. Films from chloroformic solutions, however, degraded too quickly to be measured. No definite explanation for this behavior was found. It is possible that the supramolecular structure of the films, which might be influenced by the solvent, is the crucial parameter. In particular, it cannot be excluded that small remains of chlorbenzene are still present in the films, which might prove beneficial to the film stability.

Only **D-MC-P** and **A2-MC-P** were accordingly investigated by TAS. However, only results of **D-MC-P** (Figure 3.12) will be discussed quantitatively, as the experimental setup showed huge fluctuations and irregularities when it was tried to measure **A2-MC-P**. Its excited state decay is qualitatively very similar to that of the donor film, which goes as follows: the first transient spectra upon excitation show features of GSB as well as a broad ESA, extending into the near-IR. However, this initially populated state quickly decays. For **D-MC-P**, a global fit yielded $\tau_1 = 1.6$ ps, $\tau_2 = 20$ ps, and $\tau_3 = 1400$ ps (Figure 3.13). These values complement the lifetimes as obtained from TRES: the initial locally excited state LE decays quickly and forms an

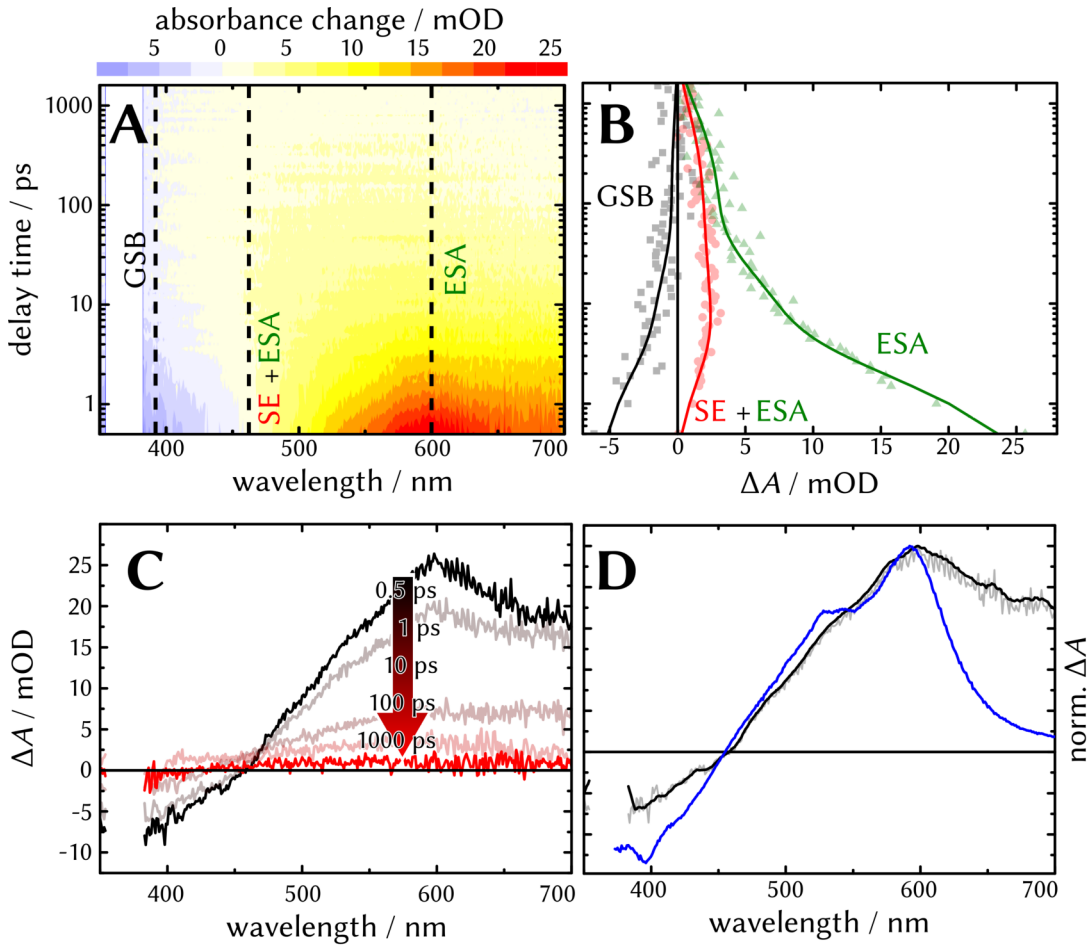

Figure 3.12: TAS of a thin film of **D-MC-P**. (A) Contour plot representation of the data. Red and blue colors stand for positive and negative amplitudes, respectively. (B) Kinetic traces at selected wavelengths. (C) Transient spectra recorded at different delay times. The arrow marks the decay of the ESA. (D) Comparison of the transient spectra of the polymer in chloroform (blue) and film (black) at 0.5 ps after excitation. Both spectra have been normalized to their respective absorption maximum. The spectrum of the film has been smoothed (solid black) using a 10 nm window.

excimer state. The occurrence of a LE is further validated by comparison of transient spectra recorded in films and solution at an early delay time (Figure 3.12D), which are very similar. Thus, LE apparently behaves as the chromophore in solution.

It has to be highlighted that $DAS_1(\lambda)$ and $DAS_2(\lambda)$, which describe the quenching of LE, are spectrally very similar. Both processes are characterized by GSB recovery and the decay of ESA. It is not necessarily so, that both correspond to

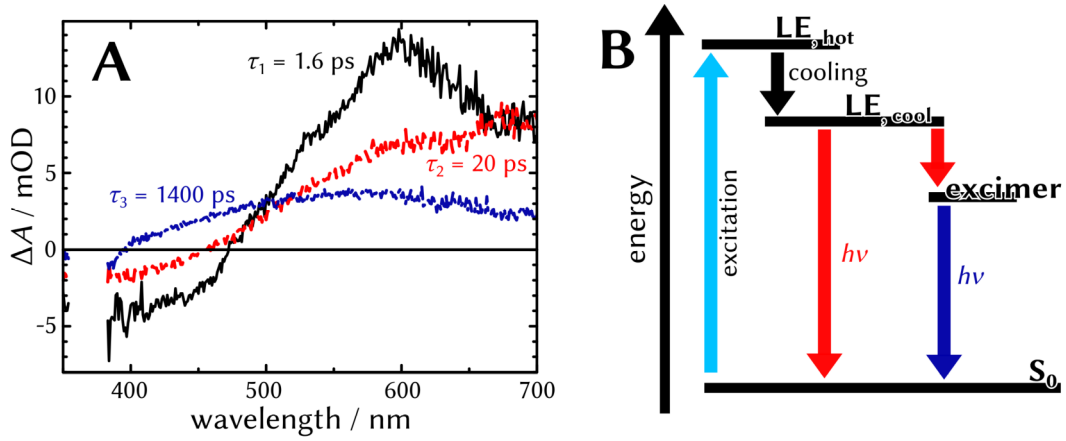

Figure 3.13. Photophysics of **D-MC-P** in the solid state. (A) DAS as obtained from a global fit of the TAS data upon 370 nm excitation. (B) State diagram depicting the deactivation pathways of the excited state. The colors of the deactivation processes correspond to the colors used in the DAS presentation.

completely different processes. In fact, the occurrence of two (spectrally) similar processes might account for the fact, that the polymer films are not perfectly ordered. Thus, the process associated with τ_1 might be excimer formation of close-lying chromophores, whereas the second DAS_2 describes the excimer formation of non-adjacent molecules. Such disordered systems often result in non-trivial excited state models, which can often be fitted using a stretched exponential function. [142] However, using a stretched exponential model did not deliver a satisfactorily fit to the data, so that the exact kinetics of the LE remain open. $DAS_3(\lambda)$ is mainly characterized by GSB recovery and the decay of broad ESA. It describes the decay of the excimer state. Notably, SE is absent from all spectra, even though excimer emission was recorded in steady-state emission and TRES experiments. It is probable that it is too weak to be recorded and overlayed by ESA. A scheme summarizing the photophysics of the film is presented in Figure 3.13B.

3.1.4 Energy Transfer Investigations

All preceding investigations were performed on homo-polymers, *i.e.*, polymers in which only one type of chromophore was incorporated. Including **D** and either **A1** or **A2** in the same polymer would allow for RET. The prerequisites of RET are met by the overlap of the emission spectrum of **D** and the absorption spectra of **A1** or **A2**, in addition to a close proximity of the chromophores. In the following section, the energy transfer in the side-chain system **DA1-SC** and the main-chain system **DA1-MC** will be described.

For both hetero-polymers, a Förster radius r_0 in the order of 40 Å ($r_{0,SC}$ = 43 Å, $r_{0,SC}$ = 33 Å) was calculated based on the steady-state spectra. The RET efficiency was then calculated by comparison of the emission lifetime of the donor in the respective homo-polymer with the hetero-polymer. For **DA1-SC**, the decay of donor emission does not follow a mono-exponential model, but decays in a more complex way (Figure 3.14). This is to be expected, as chromophore distribution is statistical. [114] Indeed, the exponential decay could be well fitted assuming a Gaussian distribution of donor and acceptor distances. An average distance r_{SC} = 51 Å was derived, with a width of the distribution of 20 Å. Thus, the "mean RET efficiency" (at 51 Å) amounts to $\eta_{RET,SC}$ = 0.74. The side-chain architecture apparently prohibits closer packing of chromophores for higher RET efficiencies.

The donor emission decay in **DA1-MC** also does not decay mono-exponentially, but for a different reason. While it also is a statistical copolymer, donor and acceptor chromophores are in discrete distances $r_{MC} \approx n \cdot (L+C)$, with the linker length $L \approx 15$ Å [143,144] and the chromophore length C. As $r_{MC} \gg r_0$ for $n > 1$, only directly neighbored donor and acceptor chromophores can undergo RET. The statistical nature of the copolymer also implies that there are **D** chromophores which are not situated directly next to **A1**. The bi-exponential decay in **DA1-MC** ($\tau_{em,1}$ =0.2 ns, $\tau_{em,2}$ =1.0 ns) accordingly originates from donors with two different

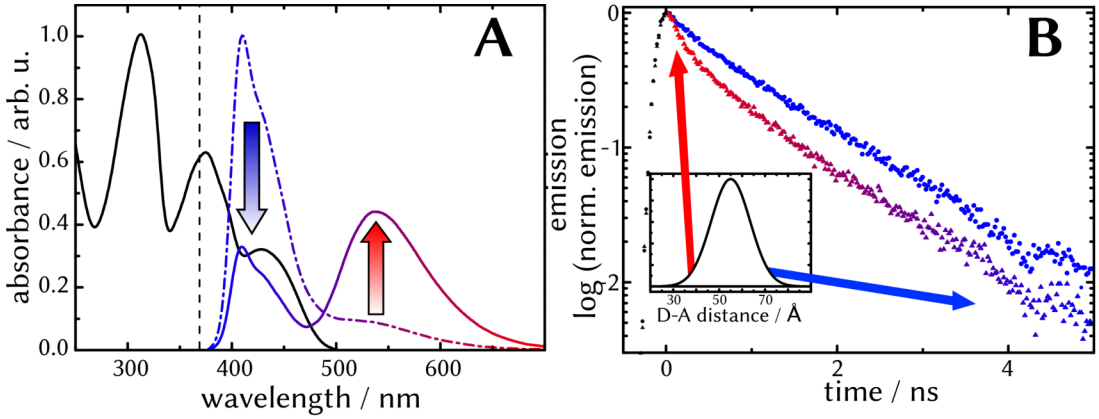

Figure 3.14: RET studies of **DA1-SC** in chloroform. (A) The steady state absorption spectrum (black) shows absorption features of the **D** and the **A1** chromophore. The donor emission (blue) is quenched in **DA1-SC** (solid line) compared to a mixture of both homo-polymers (dashed line) and acceptor emission (red) is enhanced. (B) TRES studies of **D-SC-P** (blue) and donor emission in the heteropolymer in solution. The inset shows the distance distribution of donor-acceptor pairs: those that are close to each other readily undergo RET (red), whereas those that are separated by a large distance behave like the chromophore in the homo-polymer (blue).

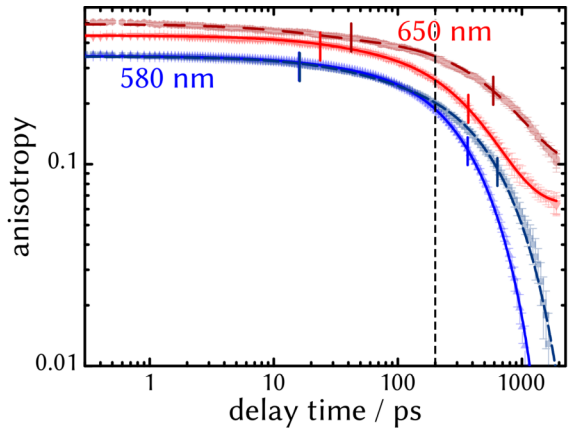

Figure 3.15: Transient-absorption anisotropy curves of main-chain unimers and polymers upon 370 nm excitation. D-MC-U (blue) and D-MC-P (dark blue) were probed at 580 nm, whereas A1-MC-U (red) and A1-MC-P (dark red) were probed at 650 nm. Vertical lines depict the time-constants of the biexponential decay (solid and dashed curves). The decay occurring at later times (indicated by the dashed black line) is attributed to diffusion processes.

molecular surroundings: the long lifetime, which is also basically identical to that of **D-MC-P**, stems from **D**, which is not located next to an acceptor, whereas the short lifetime comes from **D** which undergoes RET to an adjacent **A1**. The derived efficiency $\eta_{RET,MC} = 0.84$ is a lot smaller than one would expect: considering the molecular length of the bismaleimide linker, the efficiency of RET should be basically unity. The TRES measurements are considered to be free of experimental error; the calculated efficiency is believed to be correct. Thus, the Förster distance r_0 seems to be calculated incorrectly. However, even assuming an experimental error of 20 % in the assessment of the spectroscopic parameters needed in the calculation of r_0, its value would (due to its sixth power dependence) basically remain the same. Therefore, it is believed that the assumption of the orientation factor κ^2 is incorrect.

Assuming a $\kappa^2 = ⅔$ is only valid if the chromophore (or rather, its dipole) can freely rotate during the excited state lifetime. However, as was already discussed in Figure 3.1.2, the main-chain architecture seems to prohibit free motion of the chromophores. To gain further understanding of the movability of the embedded chromophores, transient absorption anisotropy spectroscopy was employed (Figure 3.15). Both unimers as well as polymers have been probed near their ESA maximum (for **D-MC-Z**, 580 nm, for **A1-MC-Z**, 650 nm) following 370 nm excitation. The time-dependent anisotropy $r(t)$ could be well fitted using a bi-exponential decay model

$$r(t) = r_1 \exp\left(\frac{-\rho_1}{t}\right) + r_2 \exp\left(\frac{-\rho_2}{t}\right) + r_0 \qquad \text{Eq. 21}$$

with the time constants ρ_n and their corresponding anisotropy amplitudes r_n. The offset value r_∞ corresponds to an anisotropy decay which is not finished within the investigated time-window.

The first relaxation time ρ_1 is for all compounds in the order of 20 to 40 ps. The physical process associated with this fast decay remains elusive. It is substantially slower than mere solvation ($\langle\tau\rangle$ = 2.8 ps in chloroform) [100], but falls for the **D**-containing molecules in the range of the coplanarization of the excited state. However, for **A1**, the coplanarization occurs much faster (within 10 ps, see Chapter 3.1.1.2), so ρ_1 might describe a different process in these chromophores. The second relaxation time ρ_2 on the other hand, can with a high certainty be attributed to diffusion processes: for both unimers, ρ_2 is in the order of 370 ps, whereas in both polymers, it is slowed down to ~600 ps. A similar increase in the relaxation time has been observed in chromophores attached to a side-chain polymer. [125] The depolarization of chromophores embedded is severely slowed down, as rotational or segmental diffusion is dictated by the polymer backbone.

Based on the anisotropy values of diffusion r_2, one can now calculate a correct range of values for κ^2. [114] First, one derives the depolarization factor d^x for both **D-MC-U** and **A1-MC-P**

$$d^x = \left(\frac{r_2}{r_0}\right) \qquad \text{Eq. 22}$$

with the fundamental anisotropy $r_0 = r_1 + r_2 + r_\infty$. This value is then used in the calculation of lower

$$\kappa^2_{min} = \frac{2}{3}\left(1 - \frac{d^x_D + d^x_A}{2}\right) \qquad \text{Eq. 23}$$

and upper limits of κ^2: [114]

$$\kappa^2_{max} = \frac{2}{3}\left(1 + d^x_D + d^x_D + 3\, d^x_D\, d^x_A\right) \qquad \text{Eq. 24}$$

By this approach, a range $0.4 < \kappa^2 < 1.5$ was calculated. Accordingly, Förster radii of this donor-acceptor pair are in the range of 30 to 38 Å. Taking the lower calculated Förster radius and calculating the efficiency, a $\eta_{RET,MC} = 0.92$ is calculated, in fairly good agreement with the measurement. The low value for κ^2 indicates that the dipoles of the donor and the acceptor chromophores are nearly perpendicular towards each other.

3.2 Intermolecular Reversibility – Using Hydrogen Bonds

In this sub-chapter, two different PPEs are investigated with regard to their optical properties. Both polymers differ in two ways, their hydrogen bonding site and the aliphatic linker. **PPE-NCN** bear two urea moieties per repeating unit and a polypropylene glycol backbone, **PPE-NCO** two urethane moieties per repeating unit and a PEG backbone (Figure 3.16A). While a urea moiety can form two hydrogen bonds, urethane can only form one. Both urethane as well as urea functionalities have already found use in the field of self-healing materials in recent years.[145–148] While these studies were mainly focused on mechanical properties of the material, this study entails the excited state characterization in solution and the solid state.

3.2.1 Characterization in Solution

Both polymers exhibit near identical electronic spectra in chloroformic solution (Figure 3.16B). Their absorption spectra are characterized by an absorption maximum in the UV at λ_{max} = 376 nm with moderately high absorption coefficients $\varepsilon_{\lambda max} \approx 45 \cdot 10^3\ M^{-1}\ cm^{-1}$. Similarly, no pronounced difference in their emissive behavior could be recorded. Their emission spectra peak at ~406 nm and exhibit a shoulder at ~430 nm. Also, the emission quantum yield ($\Phi_{em} \approx 0.6$) is basically the same for both molecules. Furthermore, in both cases, the excited singlet state decays mono-exponentially and with very similar emission lifetimes, $\tau_{em} \approx 0.8$ ns. Small differences in the decay kinetics between both polymers are not necessarily based on intermolecular interactions, but on the slightly different molecular (and, as a consequence, electronic) structure.

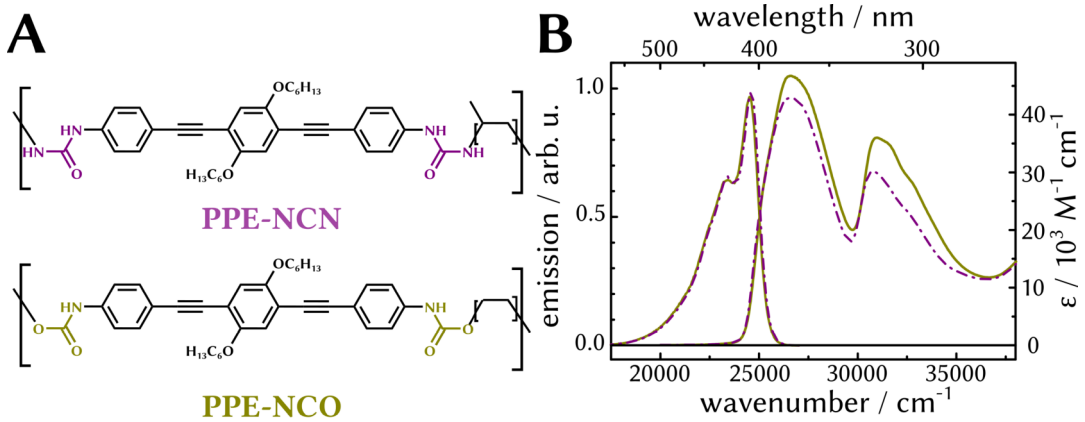

Figure 3.16: Characterization of supramolecular dynamers in solution. (A) Molecular structures of the polymers under consideration. (B) Steady-state absorption and emission spectra of PPE-NCN (purple) and PPE-NCO (green) recorded in chloroform.

In summary, no pronounced difference neither in the ground-state behavior nor in their excited state dynamics could be recorded. This points towards the absence of intermolecular interactions induced by hydrogen bonds. This is not surprising: the concentrations (of repeating units) used for absorption experiments were in the order of 10 µM, and for emission experiments even lower (1 µM). Considering the molar masses M of the polymers (6,000-12,000 g mol^{-1}) [149] and the molar mass of the repeating units (M ≈ 1,000 g mol^{-1}), the concentration of polymers in solution is in the order of 100 -1,000 nM. Association constants K_a, a measure of preference of hydrogen bonding, for hydrogen bonding in urea systems in chloroform are in the order of tens to hundreds M^{-1}.[145] Inserting this value and the concentration of free polymer into the definition of K_a (Eq. 25), the concentration of hydrogen bonded polymers in the investigated samples was in the order of 10^{-10} M or lower, several numbers of magnitudes smaller than the free polymer concentration. To achieve appreciable concentrations (> 1 µM) of aggregates, one would need solutions with concentrations above 0.1 mM, way higher than possible for absorption (limited by the maximum detectable absorption of the spectrometer) or emission (limited by the inner filter effect) experiments.

$$K_a = \frac{[\mathrm{H-bonded\ polyer}]}{[\mathrm{free\ polymer}]^2} \qquad \text{Eq. 25}$$

3.2.2 Characterization of Thin Films

The investigated polymers do not form hydrogen bonded aggregates in high yields in solution. It is to be expected that the opposite is the case for solid samples. Here, the close proximity of polymers to each other is probably considered beneficial for association. Indeed, based on IR spectra of thin films (spin-coated out of chlorbenzene with film thicknesses of ~50 nm), hydrogen bonds seem to have formed: a broad N-H band at 3,300 cm^{-1} was observed for both samples,[149] indicative for the formation of hydrogen bonds. [150] The inter-polymer interaction in the solid state is also visible from the steady-state spectra (Figure 3.17A): the absorption spectra of both polymers broadened compared to those in solution. As already discussed in Chapter 3.1.3, this is often observed for films of OAEs, but not always easy to interpret. The lowest energy absorption band could be fitted using three Gaussians, centered at the wavenumbers ν_1 to ν_3 with decreasing energy. To diminish the influence of electronic transitions located at higher energies, additional Gaussians were used in the UV region. As film absorption is limited by the absorption of the glass substrate, no comparison in this wavelength region can be performed. Three different effects could be seen for both polymers (summarized in Table 3.3):

1) The position of the Gaussians, defined as their central wavelength or wavenumber, is shifted towards lower energies in the case of the films compared to those in solution. The energetic difference between the Gaussians, however, remains mostly unchanged.
2) The full-width-at-half-maximum (FWHM) of the Gaussian located at ν_1 increases by ~500 cm^{-1}, whereas the widths of the remaining two Gaussians remain unaffected.
3) Integration of the Gaussians and normalization to the entire absorption band reveals that the contribution of each Gaussian to the overall shape of the absorption band changes in films. In particular, the contribution of the Gaussian located at ν_1 increases by ~15 %, whereas the one located at ν_2 decreases by more than 30 %. The third Gaussian remains unchanged in its relative integrated amplitude for **PPE-NCO**, but decreases for **PPE-NCN**.

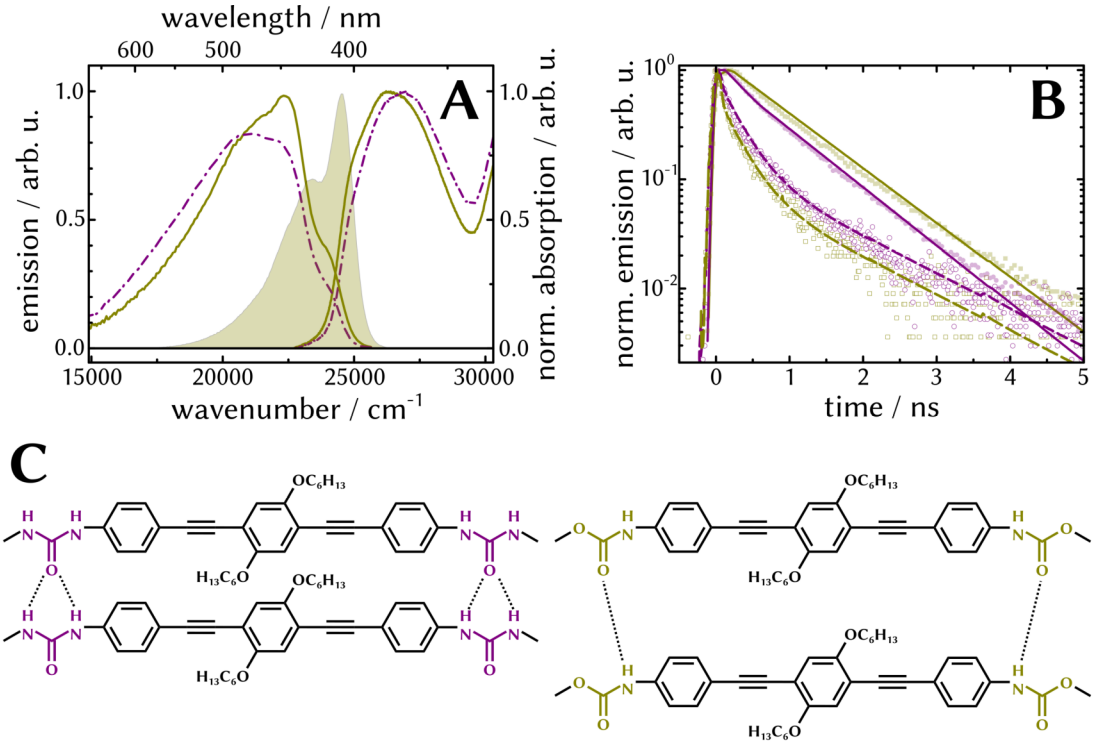

Figure 3.17. Characterization of hydrogen bonded polymers in thin films. (A) UV/Vis absorption and emission spectra of both polymers. The emission spectrum of PPE-NCO in chloroform is added in shades. (B) TRES of polymers in solution (filled symbols) and films (open symbols) upon 390 nm excitation. The lines stem from a monoexponential (solid line) or biexponential decay (dashed line) for solutions and films, respectively. (C) Schematic representation of hydrogen bondss formed between adjacent polymer chains.

These changes only indicate that polymer chains do interact, but no statement on the degree of interaction can be drawn from these results, as both polymers show very similar features in films. Emission spectra of films reveal a much drastic difference between both polymers. For both, emission spectra look qualitatively different from those in solution and are characterized by a pronounced shoulder at ~420 nm, emission peaking at ~440 nm and a broad shoulder in the low energy part of the spectrum. While emission spectra in solution can be adequately reconstructed by three Gaussians, an additional fourth component is needed for those of thin films (Table 3.4). The first three Gaussians are similar to the fits obtained for the spectra in solution, both with regards to the energy of emitted photons as well as their width. The fourth Gaussian, on the other hand, is bathochromically shifted with a peak emission at $\nu_4 \sim 19{,}000\ \mathrm{cm^{-1}}$ and much broader than the other fitting curves. The emerging picture based on the steady-state emission spectra is as follows: The three Gaussians located at higher energies are (mainly) due to the emission of single polymer chains, while the additionally needed Gaussian reflects the emission of excimers. The crucial factor in excimer formation is the spatial distance of adjacent polymer chains. Thus, a reduced single polymer emission intensity (or, alternatively, an increase of excimer emission) hints towards closer proximity of polymer chains due to increased hydrogen bonding strength. This is the case in the films investigated: in films of **PPE-NCO**, the emission of Gaussian 4 only contributes 42 % to the overall emission, whereas in **PPE-NCN**, more than 50 % of the emission stems from excimer emission.

This interpretation is nicely complemented by TRES experiments (Figure 3.17B). The emission decay in both polymer films is described by a bi-exponential decay with a short time constant $\tau_{em,1} \approx 0.2$ ns and a longer time-constant $\tau_{em,2} \approx 1.1$ ns. Spectral analysis of the TRES data reveals that the process associated with the short time constant is the collapse of higher energy emission, spectrally similar to

Table 3.3. Quantification of the lowest energy absorption band of the polymers in solution and as thin films. c_i, $\Delta\nu_i$, and LW_i are the relative integrated amplitude (normalized to the entire absorption band), offset of the center from the origin in $\mathrm{cm^{-1}}$, and FWHM LW_i of the ith Gaussian in $\mathrm{cm^{-1}}$.

sample		c_1	c_2	c_3	ν_1	$\Delta\nu_2$	$\Delta\nu_3$	LW_1	LW_2	LW_3
PPE-NCO	$CHCl_3$	0.67	0.28	0.05	27,700	1,600	2,000	2,900	1,800	900
	film	0.76	0.19	0.05	27,200	1,600	2,400	3,400	1,800	900
PPE-NCN	$CHCl_3$	0.68	0.26	0.06	27,400	1,500	2,300	2,700	1,600	900
	film	0.80	0.16	0.03	27,300	1,600	2,400	3,300	1,700	800

the structured emission recorded in solution. Thus, this time constant describes the quenching of the single polymer emission. The long-loved emission is red-shifted and is accordingly ascribed to excimer emission. By inserting the values of $\tau_{em,1,film}$ and the emission time-constant in solution $\tau_{em,solution}$, one can estimate the rate k_q of excimer formation by Eq. 26.

$$k_q = \frac{1}{\tau_{em,1,film}} - \frac{1}{\tau_{em,solution}} \qquad \text{Eq. 26}$$

For both polymers, a $k_q \sim 5 \cdot 10^9\ s^{-1}$ is obtained. It is important to highlight that the short time-constant is at the very edge of the temporal resolution available (limited by the IRF ~ 0.1 ns), so that no difference between both polymers from the emission decay can be recorded. Actually, the process of excimer formation probably occurs already in the early picosecond time-window (see, *e.g.*, Figure 3.1.3), but films of both polymers proved to be unstable under the conditions needed for TAS. Thus, no further quantification of excimer formation based on time-resolved spectroscopy could be performed. In summary, emission spectra of films indicate that excimer formation is more pronounced for **PPE-NCN**. This is likely due to the additional hydrogen bond it can form compared to **PPE-NCO** (Figure 3.17C).

Table 3.4. Quantification of the emission band of the polymers in solution and as thin films. c_i, $\Delta\nu_i$, and LW_i are the relative integrated amplitude (normalized to the entire emission band), offset of the center from the origin in cm^{-1}, and FWHM LW_i of the ith Gaussian in cm^{-1}.

sample		c_1	c_2	c_3	c_4	ν_1	$\Delta\nu_2$	$\Delta\nu_3$	$\Delta\nu_4$	LW_1	LW_2	LW_3	LW_4
PPE-NCO	$CHCl_3$	0.24	0.47	0.29	–	24,600	1,100	2,600	–	900	2,200	3,400	–
	film	0.03	0.11	0.43	0.42	24,100	1,500	2,700	4,900	900	1,400	3,400	5,700
PPE-NCN	$CHCl_3$	0.27	0.48	0.26	–	24,700	1,100	2,400	–	800	2,100	3,300	–
	film	0.01	0.09	0.36	0.54	24,100	1,500	2,900	5,200	700	1,600	3,400	5,600

Chapter 4

Photochemistry of a Conjugated Imine Polymer

In the previous chapter, conjugated polymer chemistry has been combined with dynamic covalent chemistry and the resulting optodynamers have been investigated in detail with regards to their optical properties. The subsequent chapter, on the other hand, will introduce a case study on the photochemistry and photodegradation of a conjugated imine polymer. It has already been demonstrated that imines[16], *i.e.*, molecules containing a C=N double bond, may be used in dynamer chemistry as well. In particular, self-healing systems based on imines have already been reported. [71,151–153] This is of particular importance considering the multitude of applications in which azomethines have already been implemented, *e.g.*, organic photovoltaics [154–157] or light-emitting and electrochromic devices. [158] In many instances, their facile and straightforward synthesis *via* a simple condensation reaction compared to their vinyl analogues, which require expensive catalysts and stringent reaction conditions, makes these materials interesting for organic electronics. Combining the ability to self-heal damages with the inherent optoelectronic properties of the materials could improve the lifecycles of optoelectronic devices, one of the main barriers in their commercialization. [159]

While the introduction of imine bonds has synthetic advantages over other conjugated materials, it also adds a new center of photoreactivity, namely the *E*/*Z* photoisomerization of the carbon-nitrogen double bond. One of the most studied examples of this reaction is the isomerization of structural analogues of rhodopsin, the integral part of the visual process [96,160,161], but it has also been employed in imine-based molecular motors. [162–164] In optoelectronic devices, however, it is seen as detrimental to a device's efficiency as it provides an additional unwanted deactivation channel of excited states. [165] Despite the importance of imine photoisomerization in these materials, it still remains relatively unexplored compared to their vinyl- or azo-analogues.

The study presented here focuses on the photophysical and photochemical characterization of conjugated imine polymer **tT-CN-Fl** (Figure 4.1). Its molecular

16 The term imine will be used throughout this thesis to refer to the generic carbon-nitrogen-double-bond motif. Other names in the literature are azomethines and Schiff bases, even though, depending on the author, these terms may or may not refer to special cases of imine bonds.

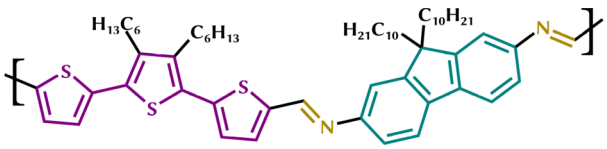

Figure 4.1: Molecular structure of imine polymer **tT-CN-Fl**. The terthiophene (purple), imine (gold), and fluorene (turquoise) moieties are highlighted in color.

structure makes it a prime model compound, as it contains a fluorene and terthiophene moiety, two predominantly employed building blocks in conjugated polymer research. These chromophores are bridged by an imine bond. The polymer is investigated in a range of several solvents, and its photophysics are studied by variation of excitation wavelength.

4.1 Spectroscopic Characterization

First, **tT-CN-Fl** was characterized by means of steady-state spectroscopy. Absorption and emission spectra were taken in solvents of different polarity (Figure 4.2A). Only minor differences between the absorption spectra were recorded. In all solvents, a broad absorption in the visible part of the spectrum was recorded, with a maximum absorption at ~470 nm and maximum absorption coefficients of $\varepsilon_{max} \approx 50 \cdot 10^3\ M^{-1}\ cm^{-1}$. The oscillator strength f of this electronic transition, as defined as the integrated absorption band [114]

$$f = \frac{4.3 \cdot 10^{-9}}{n} \int \varepsilon(\nu) \mathrm{d}\,\nu \qquad \text{Eq. 27}$$

is unaffected by solvent polarity. Taking the refractive index of the solvent n into account,[17] an average oscillator strength $f = 1.0 \pm 0.1$ was derived for all solvents.

The spectra have been analyzed using a Strickler-Berg approach (Eq. 6). [95] On average, an emissive rate constant $k_{em} \approx (9.5 \pm 0.1) \cdot 10^8\ s^{-1}$ was derived in all solvents. However, the emissive pathway (λ_{ex} = 450 nm) is heavily quenched in all solvents. The emission quantum yield Φ_{em} was measured against the reference substance $[Ru(bpy)_3](PF_6)_2$ in water (Φ_{em} = 0.063). [169] Independent of the solvent, Φ_{em} of **tT-CN-Fl** was in the order of 0.005. In this low regime, it was impossible to detect solvent influences on the yield, as the signal intensity is obscured by effects such as impurities in the solvent and Raman scattering of the solvent. Using the predicted emissive rate constant k_{em} and Φ_{em}, the lifetime of the emissive state is estimated to be in the order of 10^{-12} s. This estimation is supported by the fact that no emission lifetime of the sample could be recorded, indicating a rapid decay

17 Ignoring the refractive index, $f = 1.5 \pm 0.1$. The oscillator strength is defined with and without the refractive index in the literature. [84,114,166–168]

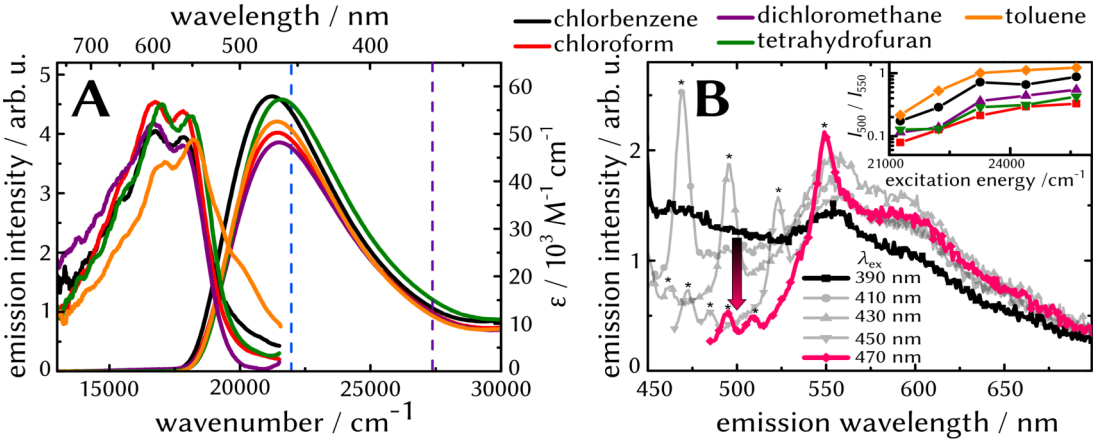

Figure 4.2: Steady-state absorption and emission spectra of **tT-CN-Fl**. (A) Absorption and emission spectra recorded in various solvents. The dashed lines indicate the excitation wavelengths used in the illumination experiments. The shoulder at ~500 nm in some solvents is due to Raman scattering and impurities in the solvent. (B) Emission spectra of **tT-CN-Fl** recorded at different excitation wavelengths in chlorbenzene. The arrow marks the decrease of emission at 500 nm when going to higher wavelengths. Emission bands due to Raman scattering of the solvent are marked with an asterisk. A plot of the emission intensity ratio recorded at 500 and 550 nm in different solvents is shown as an inset.

below the time-resolution of the instrument (tens of picoseconds). Solvent polarity also has no effect on the qualitative shape of the emission spectra. They are characterized by a peak emission at ~550 nm with a pronounced shoulder at ~600 nm, the Stokes shift being in the order of ~3,000 cm^{-1}.

While solvent effects on the emission properties were negligible, changes in excitation energy changed the emissive behavior of the sample. Going to lower excitation wavelengths, *i.e.*, increasing the photon energy, gave rise to a new emission band at ~500 nm (Figure 4.2B). This behavior was found to be independent of the solvent. Using 390 nm as the excitation wavelength, the ratio between the emission at 550 and 500 nm was tenfold increased compared to 479 nm excitation (Figure 4.2B, inset). There are two possible explanations for this behavior: Either two different transitions (related to different chromophores in the repeating unit) are excited by changing the excitation wavelength, or a photoproduct is formed in the course of the experiment that emits at a different wavelength than the original polymer. Excitation spectra recorded at emission wavelengths of 500 nm (the new emission) and 660 nm (the red edge of the original polymer emission) further validate the presence of two electronically different species (data not shown). The

500 nm emission stems from a species absorbing at 400 nm, while 650 nm emission originates from a species with an absorption maximum at 460 nm, coinciding with the original polymer absorption. In the subsequent chapters, the influence of excitation energy on the absorption properties of the sample will be investigated in detail.

4.2 Illumination by Visible Light

4.2.1 Steady-State Illumination

Absorption spectra of solutions of **tT-CN-Fl** before and directly after illumination with a 455-nm-LED did, at first glance, not exhibit pronounced differences. The main difference between both is a slightly decreased absorption in the main absorption band, which was initially attributed to some photodegradation mechanism. However, recording absorption spectra after some minutes elapsed since the irradiation showed, that the absorption was nearly restored to its original value. This was the first hint of a photochemical reaction, which is followed by a very fast thermal back reaction. A first estimate of the time-scale of the back reaction is based on the time needed to record an absorption spectrum. Absorption spectra were routinely measured from 800 nm to 300 nm, to ensure that no photoproduct absorption in the near-IR occurred and to ensure that the baseline of

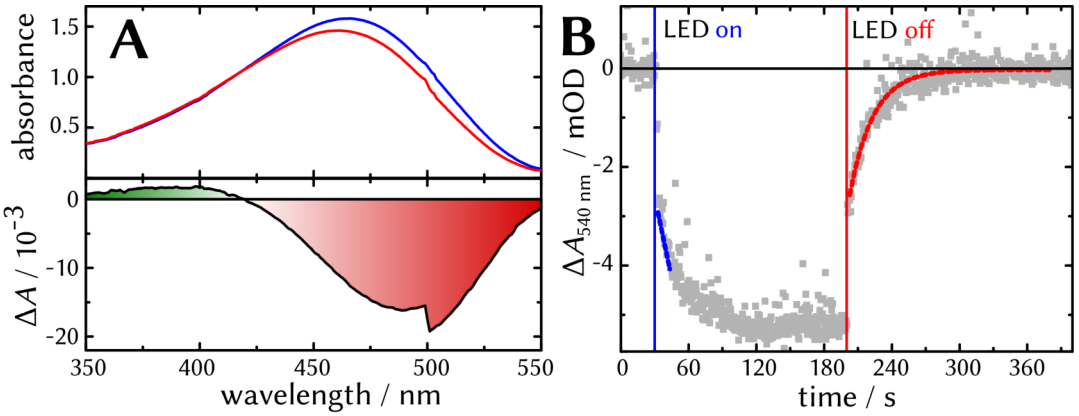

Figure 4.3: Steady-state illumination of **tT-CN-Fl** in chloroform upon 455 nm excitation. (A) Steady-state spectra recorded before (blue) and directly after (red) illumination. In the lower panel, the differential absorption of both spectra is plotted. Negative and positive changes are marked in red and green, respectively. The dip at 500 nm is due to an experimental artifact. (B) Kinetic trace of the absorbance change recorded at 540 nm. The blue line marks the quasi-linear decay of the absorption used in the assessment of Φ_r. The red line is a mono-exponential fit of the thermal reaction upon turning off the LED.

the absorption does not show an offset. The recording speed of spectra was 400 nm min^{-1}, recording a full spectrum accordingly took over 70 s. For unknown reasons, the spectrometer stops for several seconds at the 500-nm-mark, so that the actual recording time was even higher. The thermal back reaction has to be nearly completed within this time.

To test this hypothesis, the absorption spectrum between 350 and 550 nm was recorded before and directly after illumination (Figure 4.3A). The time to record this spectrum amounts to ~20 s. The difference spectrum unambiguously demonstrates a huge decrease in the main absorption band and a small increase in absorption at 390 nm. The experimental protocol was adjusted to reflect these rapid changes: Instead of recording full spectra, the absorption changes at a single wavelength were recorded. This measurement mode allows for a time-resolutions of 0.1 s. The absorption changes at 540 nm ΔA_{540} were traced (Figure 4.3B), in the red flank of the absorption spectrum, as contributions of photoproduct absorption were believed to be negligible in this spectral region (based on Figure 4.3A, the absorption maximum of the photoproduct is estimated to lie at ~380 nm). Before turning on the LED, ΔA_{540} was recorded for extended periods of time (normally, 20-60 s) to ensure that no photoreaction was triggered by the absorption of the probe light. Upon turning on the LED, the absorption decreased near-exponentially before it reached a steady-state equilibrium and remained constant. After turning off the LED, the absorption slowly recovered to its original value. This cycle could be repeated with the same sample up to eight times in a row without any noticeable non-reversible degradation occurring (Figure 4.4).

From the initial negative slope of ΔA_{540}, a reaction quantum yield $\Phi_{r,SS}$ (the subscript SS stands for steady-state) was calculated (Eq. 10). Independent of the solvent, a $\Phi_{r,SS} \approx 0.01$ was found. It has to be stated that this value only delivers a lower boundary for this value, as will be explained at the end of this chapter during the discussion of the transient-absorption data. The return of the absorption to its

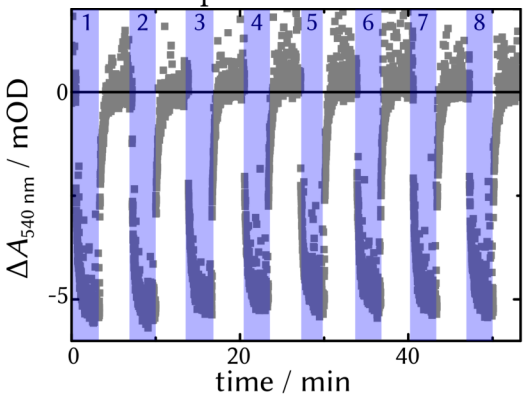

Figure 4.4. Multiple cycles of irradiation and subsequent thermal back-reaction. The blue shaded areas indicate illumination periods.

initial value after turning off the LED nicely followed an exponential behavior. For all solvents, the rate of back-reaction k_{back} as derived from a mono-exponential fitting model was in the order ~ 0.1 s^{-1}. Notably, a correlation between solvent viscosity and k_{back} was found: in less viscous solvents, such as DCM (η = 0.449) [170], k_{back} = 0.06 s^{-1}, where in the more viscous chlorbenzene (η = 0.753) [170], k_{back} = 0.15 s^{-1}.

The results presented in the preceding paragraph are surprising for two reasons. First, the *E*-isomer is normally thermodynamically more stable than the *Z*-isomer. In some reports that investigated spectroscopic properties of imine-isomers, the Z-isomer absorbs light at higher wavelengths than the *E*-isomer. [171,172] Its ground state potential barrier is energetically elevated compared to that of the *Z*-isomer, but their excited states are basically isoenergetic. In the illumination experiments of **tT-CN-Fl**, the only positive change in absorption is an increase at ~390 nm, which is blue-shifted by more than 4,000 cm^{-1} from the original absorption maximum, indicating a higher distance between the ground- and excited state in the case of the *Z*-isomer.

There are a number of possibilities to account for this finding. First, the assumption that the *E*-isomer is thermodynamically more stable might simply not be the case for the molecule investigated. Second, *Z*-isomers absorbing at lower energies is merely an empirical finding and might not be a general rule. Luo *et al.* found in a study containing both experimental as well as theoretical results, that the *E*-isomer sometimes only weakly absorbs at higher wavelengths, while the main absorption band is blue-shifted. [173] A final explanation might account for the fact that a conjugated polymer is investigated: in the *E*-isomer, the conjugation length might be lowered, due to the steric hindrance of now adjacent chromophores. In any case, no resolution of this question is given within this thesis. The other notable finding is, that the thermal back reaction –assuming the previous discussion is correct, this is the thermal reisomerization – is slowed down in less viscous solvents. This effect could not be explained during the course of this thesis and remains an open question.

4.2.2 Time-Resolved Spectroscopy

To gain further understanding of the excited state dynamics, TAS (λ_{ex} = 492 nm) was employed (Figure 4.5). The sample was investigated in toluene.[18] The first transient spectra within hundreds of femtoseconds after excitation are mainly characterized by broad negative amplitudes peaking at 480 and 600 nm. The first

18 The sample was also investigated in chloroform by means of TAS. However, even at 490 nm excitation, the stock solution turned purple, indicating photodegradation. The integrity of the sample during the measurement could thus not be guaranteed and no further investigations in chloroform were carried out.

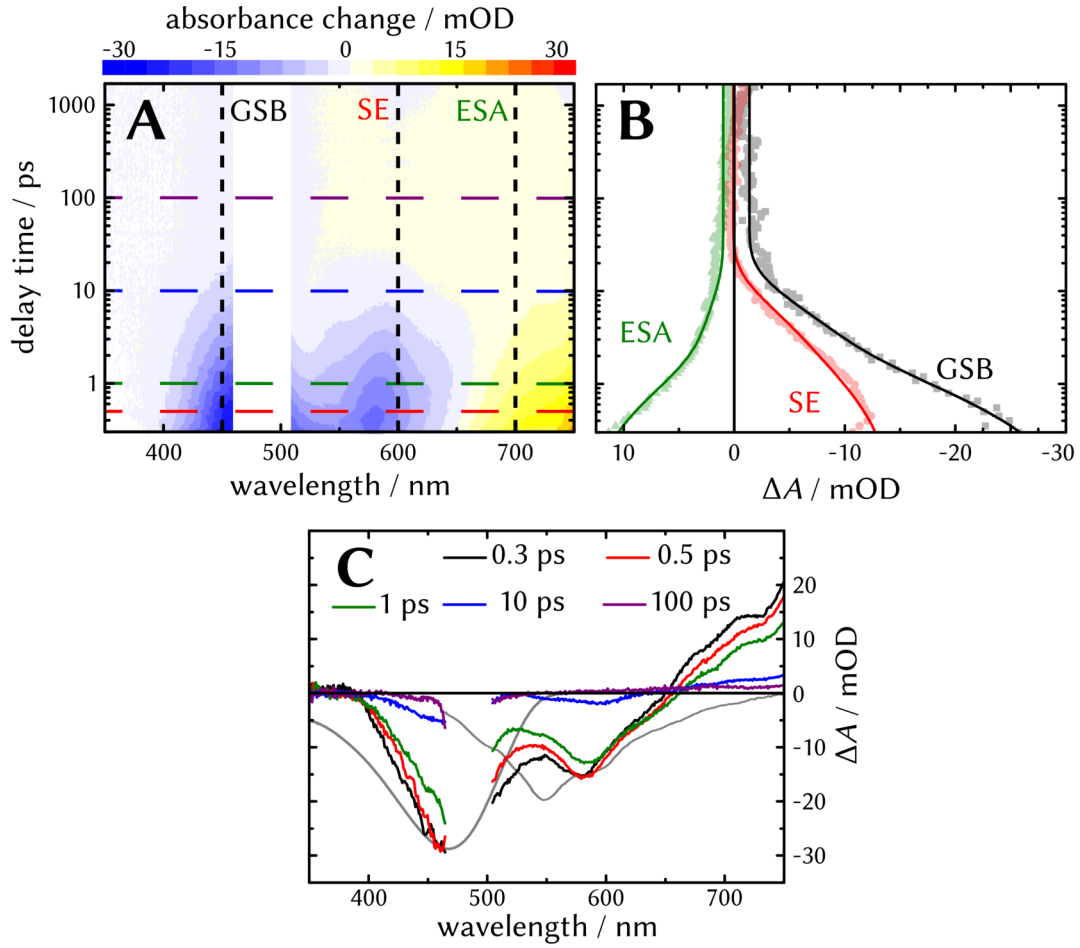

Figure 4.5: TAS of **tT-CN-Fl** in toluene upon 492 nm excitation. (A) The temporally and spectrally resolved signal intensity is visualized in a contour plot. Negative differential absorbance is indicated in blue, whereas yellow and red stand for positive changes. (B) Kinetic traces at selected wavelengths (as indicated in the contour plot). The spectral regions of the depicted kinetic profiles correspond to GSB recovery, and ESA and SE decay. The bold lines stem from a multi-exponential global fit of the data. (C) Transient spectra at selected times. The steady-state absorption and emission spectra are additionally shownin vertedly.

negative amplitude is in near-perfect superposition to the steady-state absorption spectrum and is attributed to GSB. However, the recorded GSB signal is much narrower than the steady-state absorption band. At wavelengths below 400 nm, no net absorption change was recorded. The second peak corresponds to the shoulder recorded in steady-state emission spectroscopy and is related to SE. Additionally, a positive amplitude corresponding to ESA was recorded for wavelengths above 680 nm, the edge of the detection window. The amplitude of the entire spectrum

quickly decays to zero at delay times longer than 10 ps. However, at a delay time of 1800 ps, a negative contribution due to GSB was still observed. This and a weakly pronounced ESA at wavelengths over 600 nm were the only appreciable contribution at long delay times.

Only two time constants and an offset were needed to adequately represent the excited state decay, τ_1 = 0.8 ps, and τ_2 = 6.2 ps (Figure 4.6). DAS_1 is characterized by negative contributions of GSB recovery and overlaying SE. It mainly describes the dynamic shift of SE towards higher wavelengths. An additional feature of DAS_1 is the decay and bathochromic shift of ESA.

DAS_2 shows very similar features, namely GSB recovery (this time, near perfectly superimposed with steady-state absorption), contributions from a structured SE and ESA decay. The corresponding time-constant is in perfect agreement with the excited-state lifetime as estimated from the Strickler-Berg (~10^{-12} s) approach above. As no other long lived excited state species were found, this spectrum probably corresponds to the excited state from which the isomerization occurs. The rate of photoisomerization k_{iso}, assuming a Φ_r = 0.01, is accordingly $1.6 \cdot 10^9$ s^{-1}. Deactivation mechanisms other than emission or isomerization thus are operative and contribute mainly to excited state decay. Even though terthiophenes promote ISC to the triplet state, no long-lived triplet absorption was recorded. In studies on imine-based thiophenes in the group of Skene, some molecules also showed low emission quantum yields, similar to **tT-CN-Fl**. Their excited states were mainly depopulated by means of IC. [174,175] However, no explanation for this empirical finding was given. It is very likely, that the same (unknown) mechanism is operative for **tT-CN-Fl**. Due to the polymeric structure, IC might even be more enhanced due to the “loose bolt” effect. [139]

The offset spectrum DAS_∞ mainly shows negative remaining contributions from GSB. Positive values for ΔA are recorded, however, at $\lambda \geq 600$ nm. No positive amplitude at 390 nm, as seen in the steady-state absorption spectrum, was observed. It is likely, that any product absorption at 400 nm is overlayed by GSB of the original polymer, resulting in a net change $\Delta A \approx 0$. This would also account for the fact that the GSB signal does not extend to this wavelength region, as it is superimposed by product absorption. The GSB contributions in the offset spectrum thus originate in molecules which have not returned to the initial ground-state, but isomerized. The initial GSB signal, on the other hand, is proportional to the concentration of molecules which have been photoexcited. By comparison of the initial GSB (at t = 0.3 ps) and that seen in the offset spectrum, one can estimate $\Phi_{r,TAS}$ directly from the transient absorption spectra (Eq. 28). The GSB was compared in the range of 400-460 nm, as contributions of SE in the initial transient spectrum are negligible.

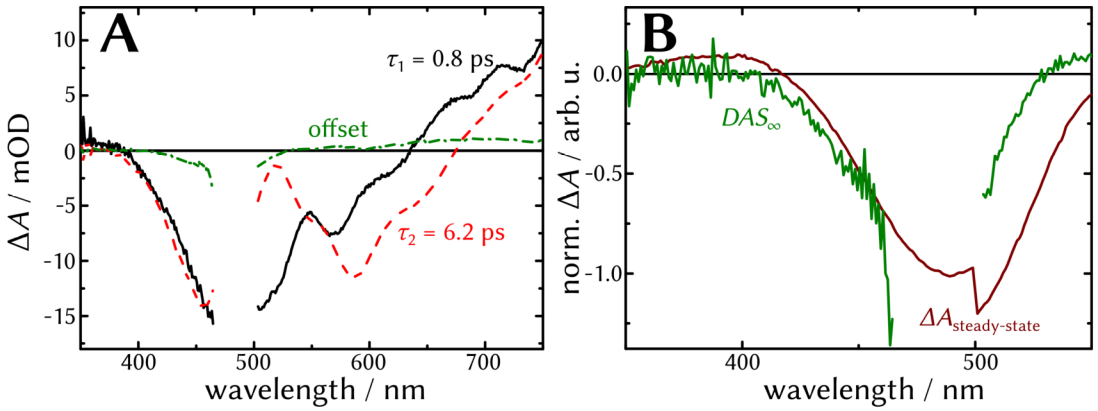

Figure 4.6: Decay-associated spectra of **tT-CN-Fl** in toluene. (A) For each DAS, the time-constant as derived from a global fit is indicated. (B) Comparison of the offset spectrum from TAS and the difference spectrum of the steady-state illumination experiment. Both difference spectra have been normalized at 455 nm.

$$\Phi_{r,TAS} = \frac{\Delta A_{offset}(400-460\,nm)}{\Delta A_{0.3\,ps}(400-460\,nm)} \qquad \text{Eq. 28}$$

This yields $\Phi_{r,TAS} \approx 0.05$, which is five times higher than $\Phi_{r,SS}$ derived from the steady-state measurements. There are two explanations to account for this. First, photoisomerized polymer might not be the only cause of the GSB in the offset spectrum. As indicated by the weak ESA, a long lived triplet state might still be populated in low yields. Thus, $\Phi_{r,TAS}$ might include contributions from Φ_{ISC}. Second, in the steady-state illumination experiments, $\Phi_{r,SS}$ is calculated by tracing the depletion of original absorption (and, indirectly, concentration), $(dA/dt)_{obs}$. The depletion of the original concentration due to the photoreaction, $(dA/dt)_{PR}$, competes with the thermal back reaction. $(dA/dt)_{TR}$. Thus, the observed change in concentration contains contributions from both terms:

$$\left(\frac{dA}{dt}\right)_{obs} = \left(\frac{dA}{dt}\right)_{PR} - \left(\frac{dA}{dt}\right)_{TR} \qquad \text{Eq. 29}$$

The reaction quantum yield $\Phi_{r,SS}$ was calculated based on two assumptions. First, $(dA/dt)_{obs}$ was obtained by fitting the data points in the first ~10 s after turning on the LED. In these early stages of irradiation, it was assumed that the photoproduct concentration was negligible. As $(dA/dt)_{TR}$ depends on the concentration of photoproduct, it was not accounted for in the calculations. [102] Second, it was assumed that the photoproduct does not absorb light at the irradiation wavelength and does not undergo a photochemical re-isomerization. This facilitates the calculation, but imines are known to photoisomerize from both isomers. If the

reisomerization can also be triggered photochemically, $(dA/dt)_{obs}$ is decreased, leading to an observed lower Φ_r.

4.3 Illumination in the UV Regime

In the previous chapter, it could be seen that illumination by visible light leads to the formation of a thermally unstable isomer. In contrast to this, illumination in the UV (λ_{ex} = 365 nm) in chloroform leads to more drastic and irreversible changes in the absorption (Figure 4.7A). First, the initial absorption band decreases in amplitude. This decrease is accompanied by a hypsochromic shift of the absorption maximum, until an absorption maximum at 400 nm remains. Additionally, a new absorption band in the near-IR region rises with an absorption maximum located at ~590 nm. Turning off the LED did not lead to a restoration of the original absorption properties. After extended illumination periods (more than 1 mmol of absorbed photons), another behavior was observed, namely an increase of the 400 nm absorption band and a decrease of the 590 nm absorption. After 2 mmol of absorbed photons, this spectrum remained basically constant. The system has not been investigated for the reversible isomerization reaction upon UV irradiation.

The occurrence of the new absorption band is attributed to the photooxidization of the terthiophene motif in the polymer. It is well known that thiophene radical cations exhibit absorption maxima at 572 nm [176], close to the absorption recorded in this experiment. The attribution to an oxidized thiophene species is further supported by spectroelectrochemical (SEC) investigations, conducted by

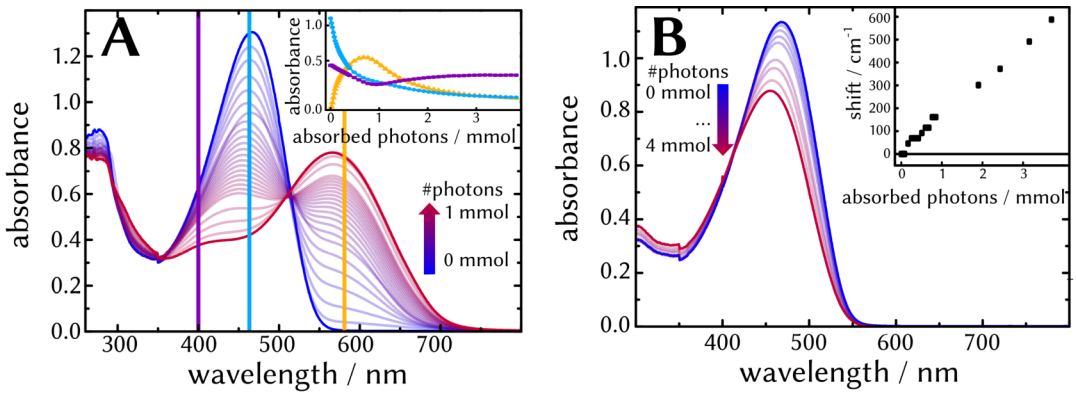

Figure 4.7: Steady-state illumination of **tT-CN-Fl** upon 365 nm excitation. (A) Steady-state spectra recorded in chloroform at different illumination times. The spectra are shown until the absorption of 1 mmol photons. In the inset, kinetic profiles at selected wavelengths are also depicted at later illumination times. (B) Steady-state spectra recorded in toluene. The inset depicts the shift of the absorption maximum as a function of absorbed photons.

Ying Zhang (Figure 4.8). A detailed description of the employed setup can be found elsewhere. [177]

In the cyclovoltammogram (CV), recorded in chloroform with the addition of 0.1 M $TBABF_4$, no clear oxidation peaks were recorded (Figure 4.8A). However, by looking at the second derivative of the CV data, two inflection points located at ~0.7 V and ~1.1 V could be identified. It is possible that these are related to not-highly pronounced oxidation peaks. Recording absorption spectra at different external applied potentials further supports the presence of two different oxidization steps (Figure 4.8B). Applying an external bias of 0.6 V does not alter the absorption spectrum, except for a small decrease of the original absorption band, heavily. Applying a higher potential (0.8 and 1.0 V) leads to the formation of a new absorption band at 600 nm, accompanied by a pronounced decrease of the absorption band at ~470 nm. No shift of the absorption maximum was recorded. At an even higher potential (U = 1.2 V), the absorption spectrum is completely altered. The absorption in the near-IR is now characterized by a broad band with a maximum at 635 nm and a pronounced shoulder at 690 nm. As the voltage applied lies above the presumed second oxidation potential deduced from the CV data, the absorption at the shoulder most likely corresponds to a twofold oxidized terthiophene. Its absorption maximum also matches that for literature reports on terthiophene. dications. [178] The original polymer absorption is reduced to a small shoulder, with another weakly pronounced shoulder located at 400 nm.

Comparison of the SEC and illumination data (Figure 4.9) leads to the conclusion, that only singly oxidized terthiophenes are generated, as the dication absorption is absent from the absorption spectra after illumination. During the illumination, the original polymer absorption decreases more than in the SEC

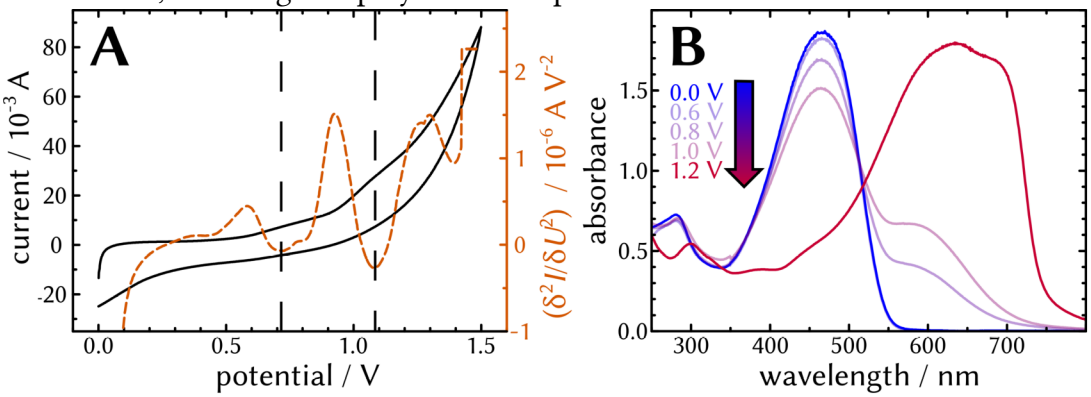

Figure 4.8: Spectroelectrochemical data on **tT-CN-F** in chloroform. (A) In addition to the cyclic voltammogram, its second derivative is also shown in orange. The dashed lines mark local minima of the derivative. (B) UV/Vis absorption spectra recorded after applying the set potential for 300 s.

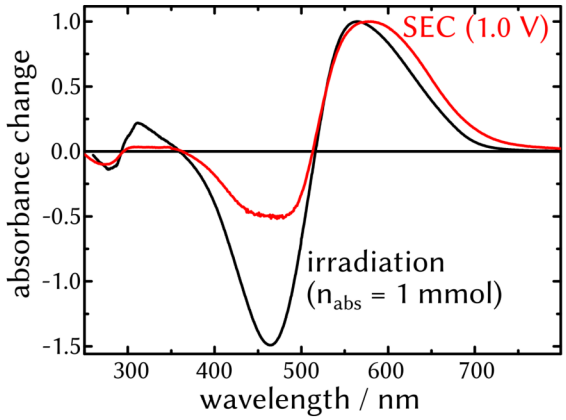

Figure 4.9: Comparison of absorbance changes during SEC and irradiation experiments on **tT-CN-Fl** in chloroform. Both difference spectra are normalized to the maximum.

experiment. The reason for this is unknown. The terthiophene cation is probably generated by interaction with the solvent. Schnabel and coworkers have extensively investigated the photodegradation of polystyrene in halogenated solvents in the early 80s. [179–181] Their explanation on the degradation mechanism involved an energy transfer from the photoexcited polymer to the solvent, which in turn dissociated into radicals. These radicals attacked the double bonds present in the molecule, generating radical cations in the process. The very same mechanism could apply to the photodegradation of **tT-CN-Fl** in chloroform. Indeed, irradiation of the polymer in toluene lead to no formation of a new band in the near-IR, meaning that no oxidized species was generated in the experiment. Instead, a gradual decay of the initial absorption band and a hypsochromic shift of the absorption maximum were observed.

Transient-absorption spectra were recorded using 403 nm as excitation energy. However, neither the spectral nor the kinetic profile of the data differ from the data recorded at 492 nm excitation. It is very possible that the photon energy employed is not high enough to induce the photochemical reaction outlined above. No investigation using even lower excitation wavelengths was performed.

4.4 Concluding Remarks

The previous experiments exemplary demonstrate the complex photochemical behavior found in conjugated polymers. The main results can be summarized as follows. (i) Neither the ground- nor the excited state of **tT-CN-Fl** seem to be affected by solvent polarity. (ii) Illumination in the visible part of the spectrum leads to a very short-lived excited state, which is probably mainly depopulated by means of IC ($\Phi_{IC} \leq 0.95$). Other deactivation pathways such as emission

(Φ_{em} = 0.01), ISC (Φ_{ISC} < 0.05), and isomerization of the imine bond (0.01 ≤ Φ_{iso} ≤ 0.05) all occur with similar efficiencies. (iii) The isomerization product thermally returns to its original isomer with a rate constant k ≈ 0.1 s^{-1}. This reaction seems to be influenced by solvent viscosity. In solvents of higher viscosity, it proceeds faster. (iv) Illumination with UV light leads to the irreversible degradation of the polymer. In chloroform, terthiophene radicals are formed, whereas the degradation mechanism in toluene remains elusive.

Chapter 5

Towards Self-Healing of Optical Properties

5.1 Optical Property Recovery Requires Restoration of Conjugation

Conjugated organic molecules, and in particular conjugated polymers, are a class of compounds, which have been extensively studied in the context of organic electronics, *e.g.*, photovoltaics and light-emitting diodes, since mid-20th century. [182–185] In particular, their facile processability compared to inorganic materials put them in the spotlight of interest for chemists, physicists, and material engineers. [45] Nevertheless, these materials also have drawbacks, namely their limited stability.

In Chapter 3, several examples of intra- and supramolecular reversible bonds were introduced, which could potentially be used in the context of self-healing polymers. However, none of the structures discussed are able to solve one of the most urgent challenges in polymer electronics, namely the degradation of conjugated polymers. Among the many degradation pathways (for an extensive review, see ref. [186]), photodegradation, *i.e.*, structural and molecular changes upon absorption of a photon, seems to be of considerable importance. In particular, oxidation of the conjugated bonds or breakage of aromatic moieties lead to irreversible failure of the material. These material damages would be reflected in altered optoelectronic properties of the material, *i.e.,* altered and decreased absorbance and emission. For this purpose, optical spectroscopy is one of the prime techniques in the investigation of photodegradation mechanism.

While there have been numerous attempts at increasing the stability of organic electronic devices, self-healing has not yet been demonstrated in these systems. In fact, there has been basically no (successful) research on the recovery of conjugated bonds at all. Williams *et al.* were the first to demonstrate the viability of self-healing of conjugation. [187] In their report, a *N*-heterocyclic carbene and a noble metal were shown to reversibly form a conductive polymer. Scratches in the polymer surface could be healed under hot dimethyl sulfoxide vapor. However, this study is inherently flawed by two factors. First, while the original polymer is

conductive, the authors do not comment on the conductivity of the damaged and healed polymer. Second, the study presents a mechanically damaged polymer that can heal its conjugation. In organic photovoltaics, mechanical damage is not the main source of failure, but photodamage is. Still, this study – published more than a decade ago – presents to this day the only known system that can recover conjugation.

The challenge in designing self-healing conjugated materials stems from the fact that (carbon-carbon) double bonds have nearly double the dissociation enthalpy (a measure of bond stability) than single bonds.[188] While light can conveniently deliver the energy needed for dissociation of this bond, the reverse process of double bond creation is thermodynamically demanding. Thus, a method which circumvents the build-up of double bonds might be suitable for designing a self-healing conjugated polymer.

5.2 Imine Metathesis in the Solid State – A Proof of Principle

With this idea in mind, imine metathesis, the C=N analogue to the C=C-olefin metathesis, was conceived to be a viable reaction mechanism. This reaction has been mechanistically investigated since the early 20th century and involves substituent change of imine bonds. [189,189] Initially, it was thought to proceed in a concerted mechanism involving a cyclic transition state. However, thermal [2+2] cycloadditions contradict the principle of conservation of orbital symmetry and are thus symmetry forbidden. It was not until the 1970s when Tóth *et al.* finally unraveled the underlying reaction mechanism [190], which is now commonly accepted. [191] In their work, the authors provided substantial evidence of a proton catalyzed reaction pathway (Figure 5.1). One of the nitrogen atoms is protonated, on which follows a cascade of several reversible reactions (one of

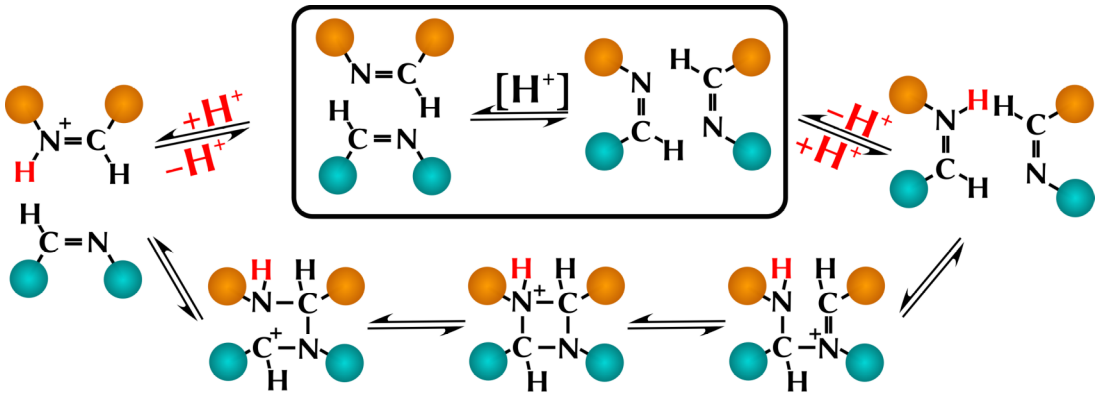

Figure 5.1: Reaction mechanism of the acid-catalyzed imine metathesis. The orange and blue balls stand for any substituent at the imine bond. The proton acting as the catalyst is highlighted in red.

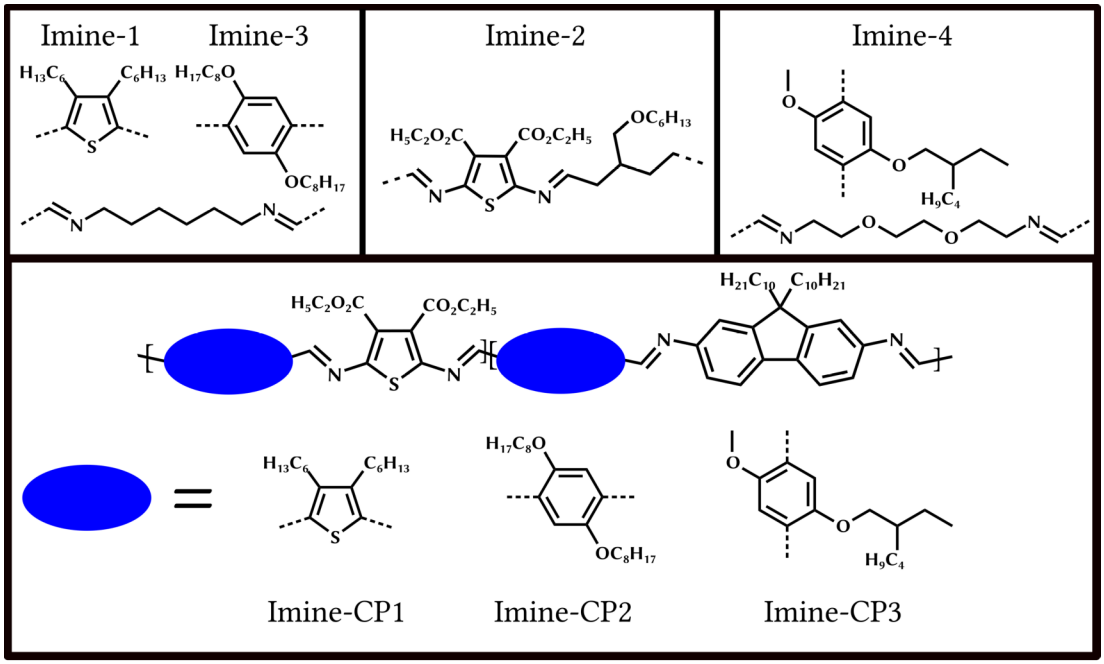

Figure 5.2: Imine-based healing agents under consideration.

which includes a cyclic intermediate). The validity of this reaction pathway has also been proven theoretically. [192]

Before the concept of imine metathesis can be applied to a self-healing system, it has to be demonstrated that it can occur a) in fully conjugated polymers and b) in the solid state. For this purpose, two conjugated imine main-chain polymers were designed: **Imine-1,** a dihexyl substituted thiophene linked to the nitrogen end of the imine bond, and **Imine-2**, a methyl formate substituted thiophene linked to the carbon end of the imine bond Figure (5.2). In both polymers, an alkyl linker is attached to the other end of the imine bond. First, exchange experiments in chloroformic solution were performed to show the general viability of the metathesis reaction for this polymer couple. For this purpose, three different polymer solutions (c_1 =10 mM, c_2 =20 mM, and c_3 =50 mM for each polymer) were stirred at room temperature and the reaction progress was monitored by UV/Vis spectroscopy (Figure 5.3B). While no reaction was observed in solutions containing no additives, the addition of 0.5 mol eq acetic acid[19] induced a reaction: the original absorption at 320 nm decreased and a new, broad, structured band appeared in the region of 360 to 600 nm. The occurrence of this band can be explained by the formation of a polymer containing paucimers[20], in which **Imine-1** and **Imine-2** are

19 The equivalents refer to moles of imine bonds, of which two are present in each repeating unit.

20 The term paucimer (from lat. *paucus*, few) is here, in analogy to unimers, used to differentiate it from oligomers. Oligomers and polymers can constitute of several paucimers, which in theirself constitute of unimers.

covalently linked to each other *via* imine metathesis. Due to a hybridization of the highest occupied molecular orbitals and the lowest unoccupied molecular orbitals of both unimers, respectively, the band gap of the metathesis product is reduced. This results in absorption at longer wavelengths (Figure 5.3A). [193,194] At the same time, the depletion of original absorption reflects the decrease of unimer concentration during the course of this reaction. Comparison with a literature report allows for an estimate of the length of the chromophoric system: Bourgeaux *et al.* synthesized imine oligomers of varying length, which incorporate very similar chromophores as used within this thesis. Depending on the oligomer length, absorption maxima between ~470 and 600 nm were recorded. [195] Based on the UV/Vis absorption data presented here, it can be concluded that mainly dimers and trimers were formed within the polymer backbone, as the absorption maximum of the new absorption band is in good agreement with that of oligomers of that length.

Having successfully demonstrated imine metathesis in solution, experiments in films were conducted next. Similar to the approach presented by Ono *et al.* [80], who blended two different hydrazone polymers with an acid catalyst and heated these films, blends of **Imine-1** and **Imine-2** were exposed to an acetic acid atmosphere and the subsequent absorbance changes recorded. In contrast to the approach of Ono, films were not additionally heated, but the experiment was conducted at room temperature. The changes in the UV/Vis absorption spectrum are near identical to those recorded in solution, indicating the formation of metathesis products. However, in the case of films that were exposed to acid, a shift of the initial absorption maximum to lower wavelengths could be observed. This hints towards degradation of the imine bond, which is susceptible to hydrolysis. [196,197] Dissolution of the imine bond decreases the overall conjugation length in the original imine polymers, hypsochromically shifting their absorption. After 30 h of reaction, no more pronounced changes in absorption could be recorded.

Finally, exchange studies were performed in the absence of acid (Figure 5.3C and D). At room temperature, blends of the imine polymers did not reveal major changes even after prolonged reaction times. By increasing the temperature up to 100 °C, on the other hand, the metathesis reaction was not only accelerated (as indicated by the increase in absorption at 450 nm), but also leads to the formation of higher conjugates: at 40 °C tempering temperature, no increase in absorption at wavelengths larger than 600 nm could be recorded, whereas tempering at 100 °C resulted in changes in this wavelength region (inset in Figure 5.3D). Furthermore, the decrease in absorbance at 320 nm, corresponding to single unimer absorption, is accelerated at elevated temperatures. It has to be noted that all experiments were

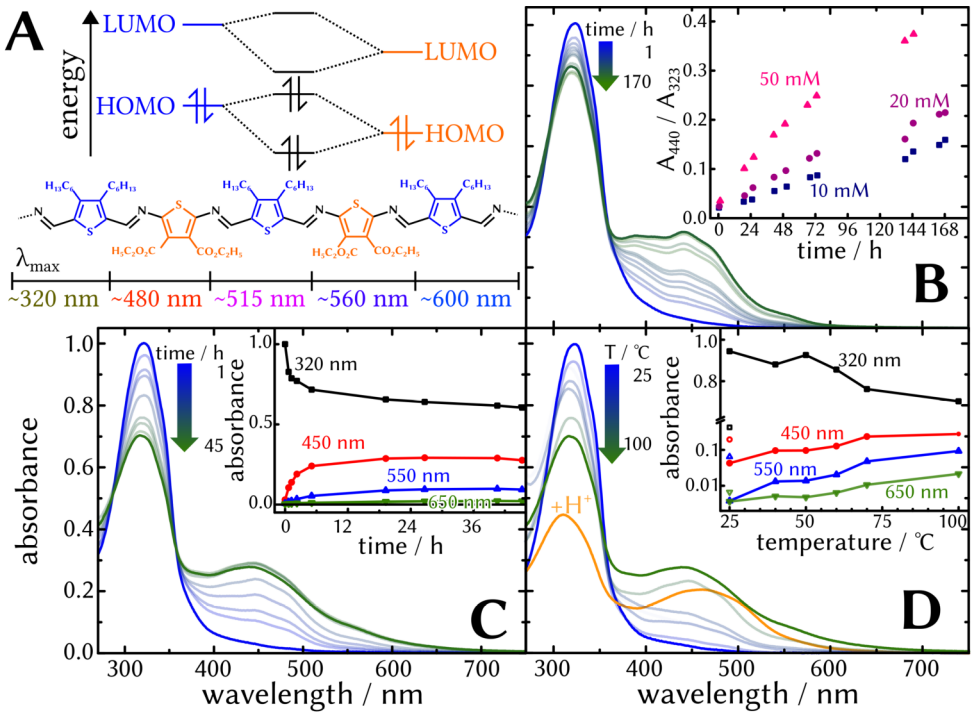

Figure 5.3: Characterization of the exchange process by means of UV/Vis absorption spectroscopy. (A) Hybridization of donor (blue) and acceptor (orange) molecular orbitals leads to a smaller band gap in the donor-acceptor molecule. The shown structures are possibly formed during the imine metathesis reaction. The absorption maxima are from a literature report on similar structures. [195] (B) Absorption changes in 50 mM chloroform solution of **Imine-1** and **Imine-2**. In the inset, the ratio of the absorption at 440 and 320 nm is plotted for all concentrations investigated. (C) Time-lapse absorption spectra of a film tempered at 100 ℃. The inset shows absorption changes at selected wavelengths as a function of reaction time. (D) Absorption spectra of equilibrated films tempered at different temperatures. Absorption values at selected wavelengths for films tempered at different wavelengths are plotted in the inset. Additionally, the spectrum of a film which was exposed to an acid atmosphere is shown. Its absorption values in the inset are shown as hollow symbols. Partially taken from ref. [151].

performed below the melting temperature of the initial materials. [151] Thus, the unimers were highly constraint within the polymer matrix and could, as a consequence, only react with other unimers in close spatial proximity. Increasing the temperature increased also the range, in which unimers can react. As a result,

the unimer depletion (as indicated by the change in absorption in the UV) is accelerated, and the formation of longer paucimers is favored.

The imine metathesis reaction is only known to occur with the aid of a catalyst [191], so that it is quite surprising that it can also be triggered in the absence of one. The influence of water from the air, that is absorbed on the polymer surface and could act as a proton donor, has been investigated. The temperature dependent experiments have been performed under inert conditions (after thoroughly evacuating a glass flask) and no pronounced changes in the kinetics could be recorded. Thus, it is still unclear what the mechanism of the metathesis reaction in the solid state is. It is conceivable that the glass substrate used could also act as a proton donor. Alternatively, the close proximity of imine bonds in the solid state favors the metathesis reaction, so that no catalyst is needed. These questions still remain open.

5.3 Restoring Absorption of a Photodamaged Polymer

The previous section delivered substantial proof that the imine metathesis reaction is suitable to allow for substituent exchange in the solid state. In this sub-chapter, several self-healing experiments were performed to deduce basic principles to generalize the concepts of self-healing of optical properties. The procedure for all experiments was the same: first, different polymer blends were heated at 100 °C for several hours, until no more changes in their absorption spectra due to the formation of donor-acceptor paucimers were recorded. Next, these thermally equilibrated samples were illuminated by a 455 nm light source, close to the peak absorption of the conjugated paucimers and polymers investigated. This illumination procedure leads to altered absorption properties of the samples due to photodamage in the material. The photodamage has been characterized by means of mass spectrometry and IR and Raman spectroscopy by Robert Geitner. [151] The main effect of irradiation is the opening of thiophene moieties as well as photooxidative cleavage of alkyl chains. No impact on the imine bond was observed, which is a prerequisite for the self-healing process. Last, the photodamaged material was heated again and time-lapse absorption spectra were taken until no further changes in the spectra could be recorded. The healing efficiency (Eq. 2) was determined by comparison of the spectrally integrated absorption of the initial, the damaged, and the heated material.

The first material under consideration is the metathesis product formed in a blend of **Imine-1** and **Imine-2**. In the photodamaged material, the absorption of the entire spectrum is reduced in amplitude (Figure 5.4). Heating the material, on the other hand, is characterized by two changes: a decrease in absorption at 320 nm, reflecting depletion of original unimers, and an increase at wavelengths

above 360 nm, indicating the formation of new conjugated paucimers. The healing mechanism can then be explained as follows: the thermally equilibrated films contain not only conjugated paucimers, but also still non-reacted unimers. Photodamaging the material removes (intact) paucimers from the thermal equilibrium. Inducing imine metathesis at elevated temperatures in turn leads to the exchange of damaged unimer units in the paucimers with intact ones, recovering paucimer conjugation, while the photodamaged unimers do not contribute to the virgin unimer absorption anymore. The first healing cycle is defined by a high healing efficiency $\eta \approx 0.5$. The whole procedure could be repeated at least five times, each cycle after the first still exhibiting high efficiencies in the order of 0.3. The average healing efficiency of five healing cycles amounted to $\bar{\eta} = 0.39 \pm 0.13$ (Figure 5.5).

Next, the same procedure was carried out on a film of a fully conjugated imine polymer **Imine-CP1**. The absorption spectrum of the thermally equilibrated polymer is characterized by a strong transition peaking at ~490 nm and only weak transitions in the UV regime. Illumination of the film led to a decrease in absorbance at 500 nm and, surprisingly, to an increase at 400 nm. Both changes are related to photodamage of the material and a photoproduct which absorbs at this wavelength region, something which has not been observed in the polymer blend investigated before. Upon heating, the absorption spectrum of the film remained virtually unchanged, with only small increases in absorption to be seen between 500 and 700 nm. Notably, the time until the photodamaged film reaches a thermally equilibrated state is heavily decreased compared to the blend of **Imine-1** and

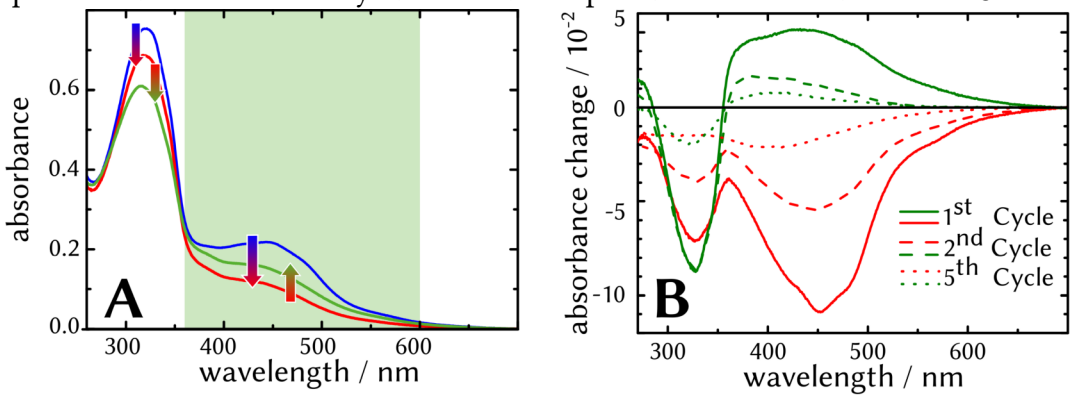

Figure 5.4: Self-Healing of a thermally equilibrated blend of **Imine-1** and **Imine-2**. (A) Spectra before (blue) and after (red) 455 nm irradiation and after thermally treating the film at 100 °C for 9 h. The inset shows the integrated absorption between 370 and 600 nm (shaded area) as a function of time, which is used in the healing efficiency determination. (B) Difference absorption of films after irradiation (red) and after thermal treatment (green) for the 1st, 2nd and 5th healing cycle.

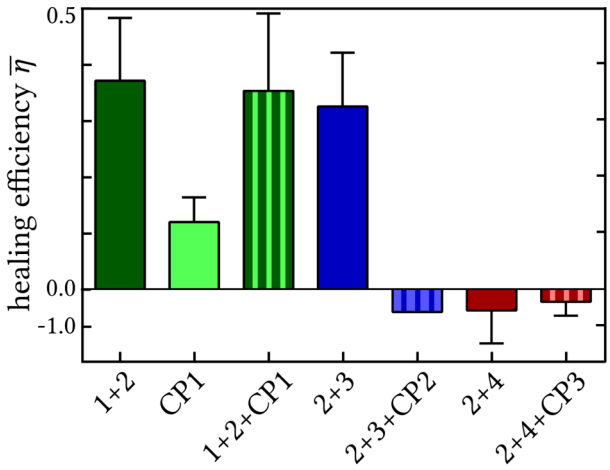

Figure 5.5: Healing efficiencies of the samples investigated. The error bars stem from multiple healing cycles of one film. Please note the different scale of the y-axis in the positive and the negative part.

Imine-2, to tens of minutes instead of several hours. Apparently, component exchange due to imine metathesis takes place, but due to the long polymer chain, the mobility of unimers is severely restricted within the polymer matrix. Still, in five healing cycles, the efficiency for each cycle was in the order of $\eta \approx 0.15$ ($\bar{\eta} = 0.13 \pm 0.05$, Figure 5.5).

In order to integrate the higher mobility of unimers into a conjugated polymer, the experimental protocol was extended to a blend of **Imine-1**, **Imine-2**, and **Imine-CP1**. The thermally equilibrated blend showed absorption features of the unimers at ~320 nm and of conjugated paucimers in the visible part of the spectrum. Similar to the system consisting of **Imine-1** and **Imine-2** only, photodegradation of the sample led to a pronounced decrease at 320 and 500 nm. Subsequent thermal treatment also led to the recovery of absorption in the visible part of the spectrum at the cost of unimer absorption at 320 nm. The changes recorded are not simply a superposition of the spectral changes recorded only for the conjugated polymer and those of the blend of **Imine-1** and **Imine-2**. This indicates that the unimers actually exchange with the chromophores present in **Imine-CP1**. The average healing efficiency of five healing cycles $\bar{\eta} = 0.37 \pm 0.16$ is very close to that of the blend of **Imine-1** and **Imine-2** and a lot higher than for films consisting only of **Imine-CP1 (**Figure 5.5).

Last, the influence of healing-agent and conjugated polymer properties on the healing process was also investigated. For this purpose, two blends, one consisting of **Imine-2** and new imine-based polymer **Imine-3**, and one consisting of **Imine-2** and **Imine-4**, were spin-coated in thin films. The chromophoric unit in **Imine-3** and **Imine-4** consists of a *bis*-alkoxy substituted phenyl, which is linked to the

carbon end of the imine bond. The most important change in the absorption spectrum compared to **Imine-1** is the extension of the absorption into the visible. Accordingly, illumination of thermally treated blends leads to a decrease in all absorption bands, as these imine polymers also absorb considerable amounts of light. Heating the films to induce a healing event only led to an increase in the spectral region between 500 and 700 nm and the number of healing cycles was very limited, as too many photodamaged unimers accumulated in the blend. Based on the molecular structure of these healing agents, two more conjugated polymers **Imine-CP2** and **Imine-CP3** were investigated in the presence of their respective healing agents. Both polymers showed no self-healing and thermal treatment upon illumination even led to decreased absorbance (Figure 5.5). The lack of absorbance recovery is more pronounced in the system based on **Imine-CP3**, which lacks a glass transition temperature. This highlights the importance of chain mobility in the healing process.

5.4 Principles of Optical Self-Healing

The approach presented here constitutes as an intrinsic, non-autonomous self-healing system. By implementing macromolecular healing agents, *i.e.*, polymers containing the conjugated unimer motif of the polymer to be healed, into a polymer matrix, the absorption of a photodamaged conjugated polymer could be restored upon a thermal stimulus. In contrast to, *e.g.*, approaches demanding encapsulation of healing agents, the healing agents are ideally immersed in the sample, facilitating the manufacturing of films. Based on the experimental results presented, the following principles for the design of a system that can heal its optical properties can be deduced:

1. The unimers used as healing agents should ideally exhibit absorption at wavelengths which are different from that of the polymer to-be-healed. Additionally, the healing agent should exhibit a high photostability.
2. The healing agent polymers should exhibit low glass transition temperatures, as this facilitates blending of the material and enhances the mobility of the healing agent.
3. The thermal equilibrium between unimers of the healing agent and conjugated paucimers should be on a level, at which the healing agent is still present in the material. Ideally, only intact unimers should act as healing agents to allow for many efficient healing cycles.

It has to be emphasized that the study presented here was only occupied with the restoration of absorption, *i.e.*, the electronic structure of the ground state. Excited state properties, in particular emission, have not been investigated, but as they play

a key role in organic electronics, developing systems which can recover these damaged properties would prove highly useful.

Chapter 6

Summary

It was a popular song from the 90s that said “Life in plastic, it's fantastic” - and indeed, the premises of the “Polymer Age” are fantastic. By now, polymers have become ubiquitous and are used in basically every conceivable way. This is an ongoing trend, and as polymers become even smarter, they might one day completely eliminate traditionally used materials from industrial and everyday applications from the market.

However, polymers – and by extension, all materials – have one inherent flaw: they break, losing their functionality, rendering them useless. Traditionally, material design was only concerned with improving the resistance of polymers towards damage, which in turn resulted in longer lifespans. However, this “damage prevention” approach still cannot fully prevent material failure. The “damage management” approach, on the other hand, presents a conceptually different way to handle material damage. Instead of avoiding the accumulation of damage, it tries to cope with it and, by means of self-healing materials, only looks at the net usage time of the material. However, self-healing research is still in its infancy: as of now, it cannot heal more sophisticated material failures, such as the photooxidative cleavage of bonds, that lead to material failure not on a mechanic, but on an optoelectronic level. Additionally, spectroscopic methods are rarely applied in the investigation of self-healing systems, and are mainly used to only uncover the chemistry behind the healing event, and not to probe the material properties.

This work aims to fill this gap in self-healing material research. It is divided in three parts, reflecting the three stages (characterization, damaging, healing) of self-healing experiments. In the first part, dynamically bonded polymers, so called dynamers, have been investigated with regards to their optical properties. Dynamers represent a class of materials, which is able to intrinsically, meaning in the absence of additives, self-heal damages inflicted on them. Three kinds of dynamers, representing the most important macromolecular structures, have been investigated: Side-chain, main-chain, and supramolecularly bonded polymers. In the case of side- and main-chain polymers, Diels-Alder bonds were employed to introduce centers of reversibility, whereas hydrogen bonds were used in the supramolecular case. All dynamers incorporated oligo-arylene-ethynylenes, a material class with high emission yields.

In particular, side- and main-chain polymers have been investigated focusing on the influence of polymer architecture on their optical properties. Two different kinds of oligo-arylene-ethynylenes were incorporated as unimers, *i.e.*, as dynamer building blocks: an alkoxy-substituted oligo-arylene-ethynylene, that might be used as a donor in energy transfer experiments, and two different thiadiazole-based oligo-arylene-ethynylenes, that can act as acceptors. First, the unimers were investigated in solution (Figure 6.1A). The photophysics of the donor are mainly characterized by a coplanarization of the three phenyl rings within 30 ps after photo-excitation. This coplanarized state then emits light in high efficiencies or can undergo intersystem crossing to the triplet state. The excited state decay in the acceptor chromophores, on the other hand, is a lot more complicated. The first step in their photophysical cascade is also a coplanarization of the phenyl rings. However, this coplanarized, locally excited state can undergo internal conversion into an internal charge transfer state. This state is only available in polar solvents, whereas the locally excited state apparently decays "normally" in unpolar solvents, mainly by means of fluorescence. The population of the internal charge-transfer state is an activated process with an activation barrier in the order of 10 kJ mol^{-1}. This activation energy is a hint towards the charge transfer state formation mechanism, which might involve a further rotation around the carbon-carbon triple bond. The internal charge transfer state is also mainly depopulated by fluorescence; intersystem crossing seems not to play an important role for thiadiazole-ethynylenes.

Embedding these chromophores into polymers leads to no notable changes on their photophysics; their behavior is basically identical to their respective unimer. However, for all polymer architectures, the rate of internal conversion, which has not contributed to the unimer excited state decay, is enhanced. This is attributed to the "lose bolt" effect, the increase of internal conversion *via* introduction of flexible substituents. The side-chain architecture seems to enhance internal conversion in particular, whereas chromophores in a main-chain framework are apparently much more rigidly restricted in their movement (Figure 6.1B). Investigating these polymers in the solid state, on the other hand, reveals no big difference between polymer architectures or different chromophores. In all samples, the locally excited state is depopulated by the formation of an excimer state (Figure 6.1B). Whether this state includes inter- or intrapolymer excimers could not be resolved within this thesis.

The polymers have also been used in energy transfer experiments (Figure 6.1C). Here, both donor as well as acceptor chromophores were embedded into the polymer chains to generate hetero-donor-acceptor-polymers. The side-chain architecture revealed a statistic distribution of donor and acceptor chromophores,

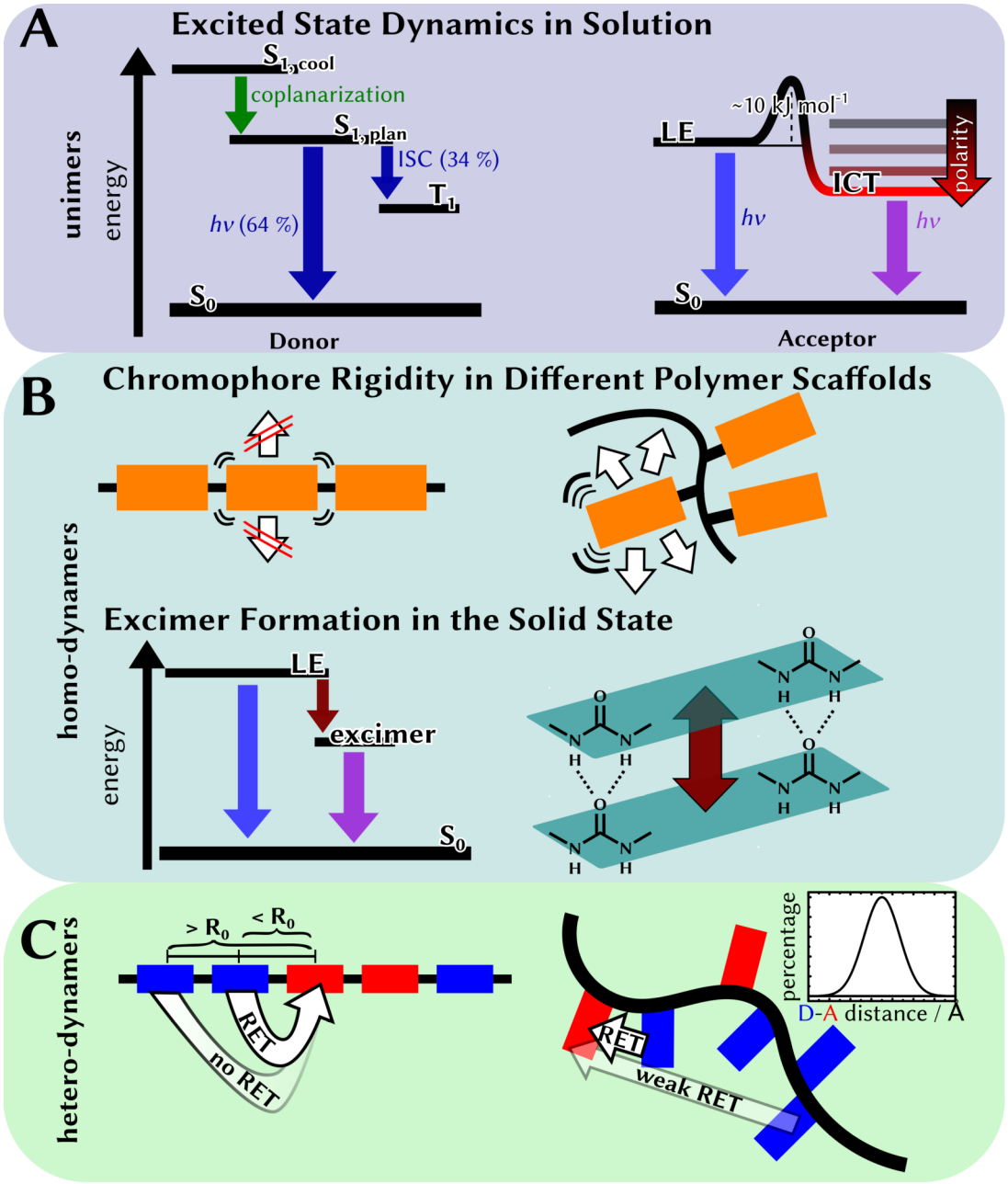

Figure 6.1: Graphical summary of Chapter 3. (A) The phtophysical processes of unimers in solution have been studied. (B) The unimers have been inserted into different polymer architectures. Differences in non-radiative rates and excimer formation were found. (C) Hetero-Dynamers were used in energy transfer experiments.

which leads to only medium energy transfer efficiencies. The main-chain polymers also displayed lower efficiencies than one would expect based on the molecular donor-acceptor distances. By means of anisotropy experiments it was found, that

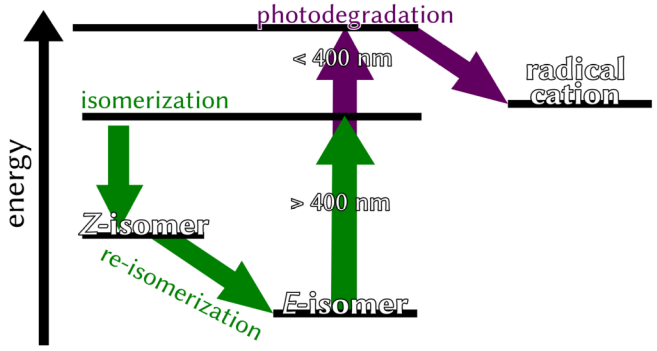

Figure 6.2: Graphical Summary of Chapter 4. Depending on the excitation wavelength, different degradation pathways in a conjugated imine polymer could be addressed.

the relative orientation of donor and acceptor chromophores is not favorable for an energy transfer. This could correlate with the rigid incorporation of these polymers within the polymer backbones, which prevents a random orientation of the chromophores within the donor's excited state lifetime.

The other type of dynamers investigated involved hydrogen bonds. Two different hydrogen bond binding sites, the urea (can undergo two) and the urethane (can undergo one hydrogen bond), were introduced into an oligo-phenylene-ethynylene based system, separately. In diluted solutions, both polymers behaved nearly identical. However, films of both polymers showed distinct differences: in the urea-polymer, excimer formation is more enhanced than in the urethane polymer. This could be rationalized by the stronger hydrogen bonds in the urea polymer, which leads to a denser chromophore packing.

In the second part of this thesis, an imine based conjugated polymer was investigated with regards to its photochemical degradation (Figure 6.2). In particular, an impact of the excitation wavelength on the degradation pathway was found: illuminating the sample with visible light leads to the formation of a short lived (several picoseconds) excited state. This state is mainly depopulated by means of internal conversion to the ground-state. However, fluorescence (1 %), isomerization of the imine bond (up to 5 %), and possibly intersystem-crossing to the triplet manifold (< 1 %) also contribute to its decay. The isomerization product, which is presumed to be the *E*-isomer, absorbs at lower wavelengths than the *Z*-isomer, which is atypical for conjugated imines. A conjugation break induced by the isomerization might account for this finding. The *E*-isomer readily re-isomerizes to the original polymer within several seconds at room temperature.

Illumination in the UV regime, on the other hand, led to irreversible degradation of the polymer. Illumination of chloroformic solutions generated a thiophene radical cation, an assertion that is supported by spectroelectrochemical

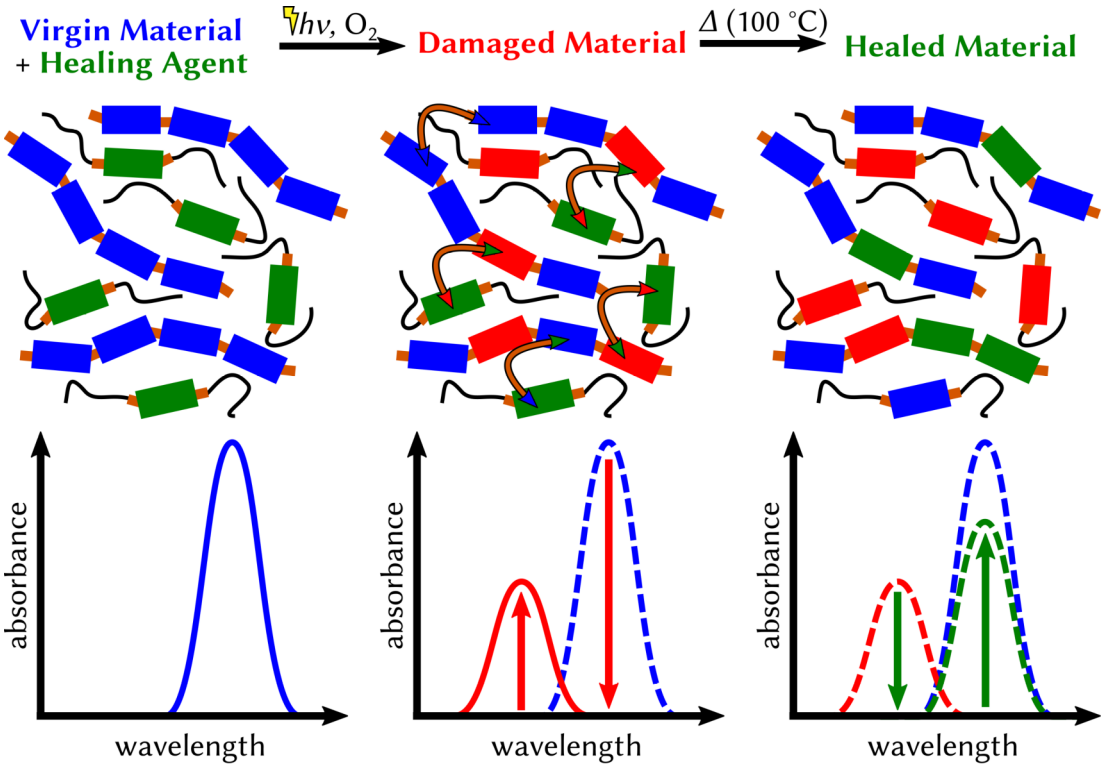

Figure 6.3: Graphical summary of Chapter 5. A self-healing system based on the addition of healing agents was envisioned. Photodamaged blends of a conjugated imine polymer and the healing agents showed recovery in absorbance upon thermal treatment.

investigations. In toluene, the conjugation of the polymer decreases, as indicated by a decrease in both absorption as well as a shift of the absorption maximum. Transient absorption spectroscopy could not unravel the exact decay mechanism of the polymer, as the excitation wavelength employed (403 nm) was not high enough in photon energy.

In the last chapter of this work, self-healing experiments of imine-based polymers were presented (Figure 6.3). The utilized reaction mechanism is based on the imine-metathesis reaction, during which a substituent exchange occurs at the imine bond. In proof-of-principle experiments, this exchange was visualized by the formation of conjugated donor-acceptor chromophores, which showed new absorption features in the visible range of the spectrum. These experiments were conducted in acidic solutions, in the solid state under an acetic atmosphere, and in the solid state under atmospheric conditions. Notably, the metathesis reaction also proceeded in the absence of acid, but at elevated temperatures, which was unknown for this type of reaction.

Next, self-healing experiments using the metathesis reaction were envisioned. First, only small conjugated polymers were photodamaged by irradiation at their absorption maximum. The photodamage of the material, which was mainly bond dissociation of the thiophene units, was reflected in the decreased absorption properties of the material. Thermal treatment of the photodamaged films led to a partial restoration of the absorbance due to the imine exchange reaction. A larger conjugated imine polymer did only show little self-healing efficiency. This is rationalized by the limited mobility of chromophore units within the films. Consequently, the large conjugated material was blended with imine polymers, which contained only single chromophores. This blend showed increased healing efficiencies. The added polymers thus act as supramolecular healing agents. Changing the properties of the healing agents, namely their glass transition temperature and extending their absorption to the visible range of the spectrum, led to non-healing systems. Based on the results, basic principles for the design of self-healing optical materials were derived.

Within this thesis, dynamically linked polymers have been investigated with regards to their optical properties. The presented results directly build on the current state of dynamic and self-healing chemistry, expanding it to the field of optoelectronic materials. This, in turn, will clear the path for future, smart materials, such as self-healing organic semiconductors.

Chapter 7

Zusammenfassung

In einem Pop-Song der Neunziger Jahre heißt es: „Life in Plastic, it's fantastic“ – und tatsächlich sind die Verheißungen des „Polymerzeitalters“ fantastisch. Mittlerweile sind Polymere allgegenwärtig und haben Verwendung in jedem nur denkbaren Arbeitsfeld gefunden. Dies ist eine fortlaufende Entwicklung, und immer ausgefeiltere Polymere könnten eines Tages konventionelle Materialien vollkommen aus industriellen und alltäglichen Anwendungen verdrängen.

Jedoch haftet Polymeren – und im engeren Sinne allen Materialien – ein Makel an: Sie gehen kaputt, und verlieren dabei ihre Funktionalität, was sie nutzlos werden lässt. Bisher war die Materialwissenschaft vor allem mit der Erhöhung der Schadensresistenz von Polymeren beschäftigt, was ihre Nutzungsdauer erhöhte. Aber auch dieser Ansatz der „Schadensvermeidung“ konnte ein Materialversagen nach längerer Nutzungsdauer nicht verhindern. Ein konzeptionell anderer Ansatz, die „Schadensverwaltung“, verfolgt eine andere Herangehensweise an Materialschäden. Statt die Ansammlung von Schäden zu vermeiden, versucht man diesem Ansatz folgend, die Schäden mittels selbstheilender Materialien in Schach zu halten. Dies sorgt für eine Nutzungsdauerverlängerung des Materials. Die Erforschung und Entwicklung selbstheilender Materialien steckt jedoch noch in den Kinderschuhen: Derzeit ist es noch nicht möglich, komplexere Materialschäden, die sich nicht auf die mechanischen, sondern die optoelektronischen Eigenschaften des Materials auswirken (beispielsweise die photooxidative Spaltung von Bindungen), zu heilen. Außerdem werden spektroskopische Methoden, die bei der Erforschung der Materialien und ihrer Schädigungen eine gewichtige Rolle einnehmen könnten, bisher kaum eingesetzt und dienen derzeit meist ausschließlich der Aufklärung der zugrunde liegenden Selbstheilungschemie.

Diese Arbeit zielt darauf ab, diese Lücke im Forschungsfeld der Selbstheilung zu füllen. Sie gliedert sich in drei Abschnitte, welche die drei Stufen eines Selbstheilungsexperiments (Charakterisierung, Schädigung, Heilung) reflektieren. Im ersten Teil der Arbeit wurden dynamisch verknüpfte Polymere, sogenannte Dynamere, hinsichtlich ihrer optischen Eigenschaften untersucht. Dynamere stellen eine Materialklasse dar, welche intrinsisch, also ohne die Zugabe von Zusatzstoffen, Schäden selbstheilen kann. Drei verschiedene Arten von Dynameren wurden untersucht. Diese lassen sich den drei wichtigsten makromolekularen Strukturen auf dem Gebiet der Dynamere zuordnen: Hauptketten-, Seitenketten- und

supramolekular verbundene Polymere. Im Falle der Haupt- und Seitenkettenpolymere wurden Diels-Alder-Systeme zur reversiblen Verknüpfung in die Polymerstruktur eingebaut, während Wasserstoffbrückenbindungen als supramolekulares Strukturelement genutzt wurden. Alle untersuchten Dynamere verwendeten Oligoarylenethinylene als stark fluoreszierende Chromophore.

Im Falle der Seiten- und Hauptkettensysteme lag der Fokus der Untersuchung auf dem Einfluss der Polymerarchitektur auf die optischen Eigenschaften. Zwei unterschiedliche Oligoarylenethinylene wurden als Unimere, d.h. als Dynamerbausteine, genutzt: ein Alkoxy-substituiertes System, welches als Donor in Energietransferexperimenten genutzt werden kann, sowie zwei verschiedene Thadiazol-basierte Systeme, welche als Energietransferakzeptoren agieren können und sich hinsichtlich ihrer Substituierung unterscheiden. Zunächst wurden die Unimere in Lösung untersucht (Abbildung 7.1A). Die Photophysik des Donors ist hauptsächlich durch eine schnelle Koplanarisierung (30 ps nach Photoanregung) der drei Phenylringe charakterisiert. Dieser koplanarisierte Zustand kann daraufhin entweder sehr effizient Photonen in Form von Fluoreszenz emittieren oder mittels Interkombination in den Triplettzustand übergehen. Der Zerfall des angeregten Zustands der Akzeptorsysteme ist etwas komplexer. Auch bei diesen Molekülen stellt die Koplanarisierung des aromatischen Ringsystems den ersten Schritt der Zerfallskaskade dar. Dieser koplanarisierte Zustand kann jedoch in einen internen ladungsseparierten Zustand übergehen. Dieser Zustand ist nur in polaren Lösungsmitteln zugänglich, wohingegen der lokal angeregte Zustand in unpolaren Lösungsmitteln „normal“ zerfällt. Fluoreszenz stellt den Hauptdeaktivierungspfad des lokal angeregten Zustands dar. Die Bevölkerung des ladungsseparierten Zustands ist ein aktivierter Prozess mit einer Aktivierungsbarriere von ungefähr 10 kJ mol^{-1}. Die Höhe dieser energetischen Barriere gibt Rückschluss auf den Bildungsmechanismus des Zustands, welcher eine weitere Rotation der aromatischen Ringe beinhalten könnte. Im Gegensatz zum Donorsystem spielt Interkombination in den Triplettzustand so gut wie keine Rolle bei den Akzeptorsystemen. Stattdessen wird der ladungsseparierte Zustand nahezu ausschließlich durch Fluoreszenz entvölkert.

Das Einbetten der Chromophore in eine Polymerstruktur führte zu keinen stark ausgeprägten Änderungen ihrer Photophysik; die Dynamere und Unimere verhalten sich nahezu identisch. Bei der Entvölkerung des angeregten Zustands der Polymere ist jedoch die innere Konversion in den Grundzustand, welche bei den Unimeren keine Rolle spielte, stärker ausgeprägt (Abbildung 7.1B). Dies wird mit Hilfe des „lose bolt“-Effekts (eng. *lockere Schraube*) rationalisiert, welcher besagt, dass die innere Konversion durch die Einführung flexibler Substituenten zunehme. Vor allem die Seitenkettenarchitektur scheint innere Konversion zu

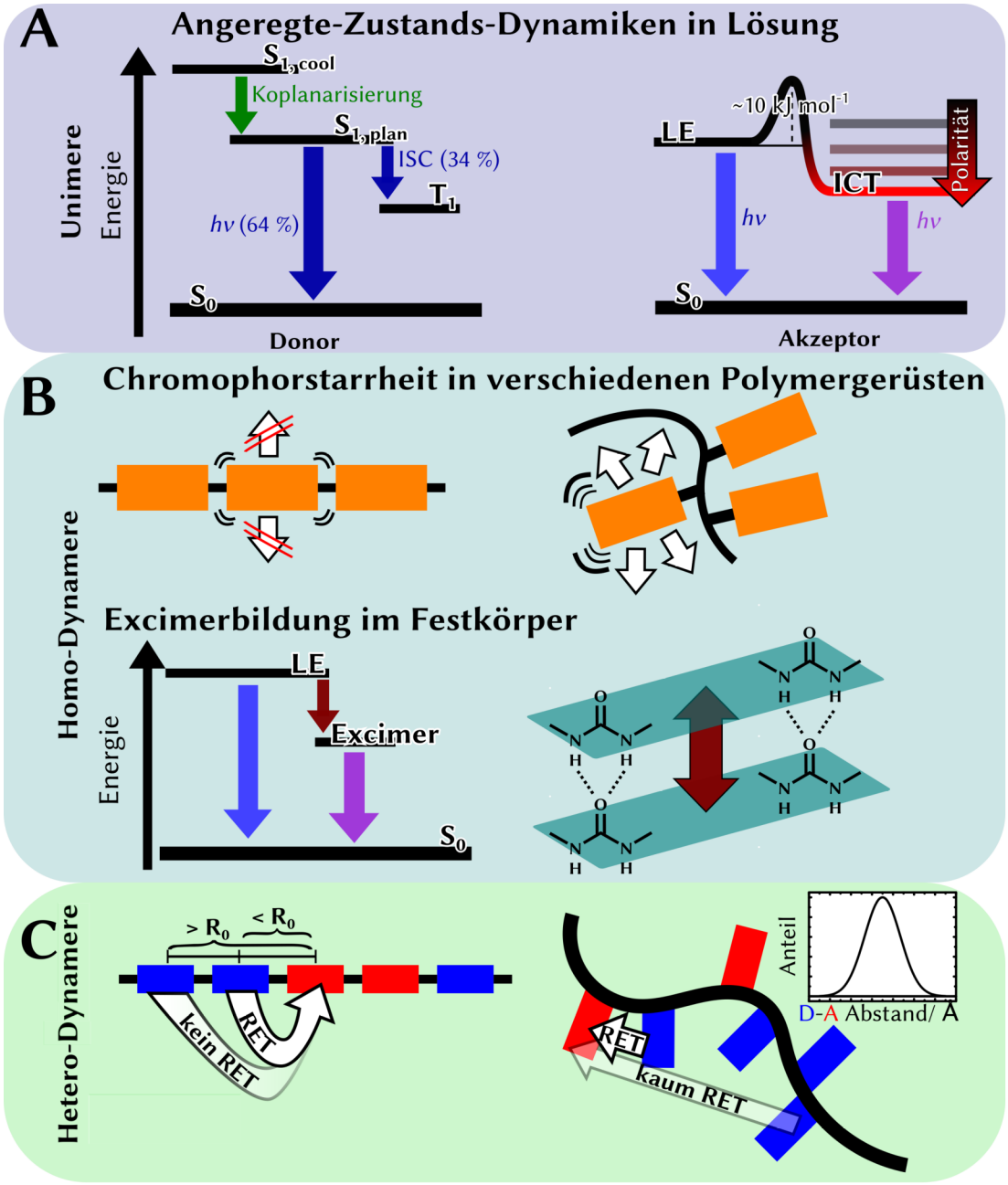

Abbildung 7.1: Graphische Zusammenfassung der Ergebnisse aus Kapitel 3. (A) Die photophysikalischen Pozesse von Unimeren wurden in Lösung untersucht. (B) Die Unimere wurden in verschiedene Polymerarchitekturen eingebettet. Unterschiede in nicht-strahlenden Raten und der Excimerbildung wurden gefunden. (C) Hetero-Dynamere wurden in Energietransferexperimenten genutzt.

begünstigen, während Chromophore in einem Hauptkettenpolymer stärker in ihrer Bewegungsfreiheit eingeschränkt zu sein scheinen. Untersuchungen der Polymere

im Festkörper zeigten weiterhin, dass Unterschiede in Polymerstruktur und -zusammensetzung im Film keine Rolle mehr spielen. In allen Proben wird der initial angeregte Zustand durch die Bildung von Excimeren entvölkert. Ob diese Excimere inter- oder intramolekular gebildet werden, konnte innerhalb dieser Arbeit nicht aufgeklärt werden.

Die Polymere wurden außerdem in Energietransfer-Experimenten genutzt (Abbildung 7.1C). Sowohl Donor- als auch Akzeptorunimere wurden in die Polymere eingebaut, um Hetero-Donor-Akzeptor-Polymere darzustellen. Bei der Seitenkettenarchitektur wurde eine statistische Verteilung des Donor-Akzeptor-Abstands gefunden, welche nur zu einer mittleren Transfereffizienz führt. Die Effizienz des Energieübertrags in der Hauptkettenarchitektur war im Vergleich zum Erwartungswert (basierend auf spektralem Überlapp und theoretischem Abstand der Chromophore) verringert. Mit Hilfe zeitaufgelöster Anisotropieexperimente konnte ermittelt werden, dass die relative Orientierung der Chromophordipole zueinander unvorteilhaft ist. Dies könnte mit der bereits erwähnten starreren Einbettung in der Polymermatrix zusammenhängen, welche eine zufällige Orientierung der Chromophore innerhalb der Lebenszeit des angeregten Zustands verhindert.

Die andere untersuchte Dynamerart basiert auf Wasserstoffbrückenbindungen. Zwei verschiedene funktionelle Gruppen, die Harnstoff- und Urethangruppe, welche zwei bzw. eine Wasserstoffbrücke ausbilden können, wurden je in ein Oligoarylenethinylensystem eingebettet. In verdünnten Lösungen verhielten sich beide Polymere nahezu identisch. In dünnen Filmen zeigten sichtjedoch charakteristische Unterschiede zwischen beiden: Im Harnstoffpolymer ist die Bildung von Excimeren im Vergleich zum Urethanpolymer verstärkt. Dies konnte durch die stärkere Wechselwirkung benachbarter Polymere erklärt werden, welche zu einer dichteren Packung der Polymere führt (Abbildung 7.1B).

Der zweite Teil der Arbeit befasste sich mit der Photochemie eines konjugierten Iminpolymers (Abbildung 7.2). Es wurde vor allem eine Abhängigkeit der Photochemie von der Anregungswellenlänge gefunden: Bestrahlung mit sichtbarem Licht führte zur Bildung eines kurzlebigen (wenige Pikosendungen) angeregten Zustands. Dieser wird vor allem durch innere Konversion in den elektronischen Grundzustand entvölkert. Fluoreszenz (1 %), Isomerisierung um die Iminbindung (1 bis 5 %) sowie möglicherweise Interkombination in den Triplettzustand (unter 1 %) tragen auch zur Entvölkerung des initial angeregten Singulettzustands bei. Das Reaktionsprodukt der Isomerisierung, welches wahrscheinlich das *E*-Isomer ist, absorbiert bei niedrigeren Wellenlängen als das *Z*-Isomer, was atypisch für konjugierte Imine ist. Ein durch die Isomerisierung verursachter Konjugationsbruch könnte eine Erklärung dafür liefern. Das *E*-Isomer

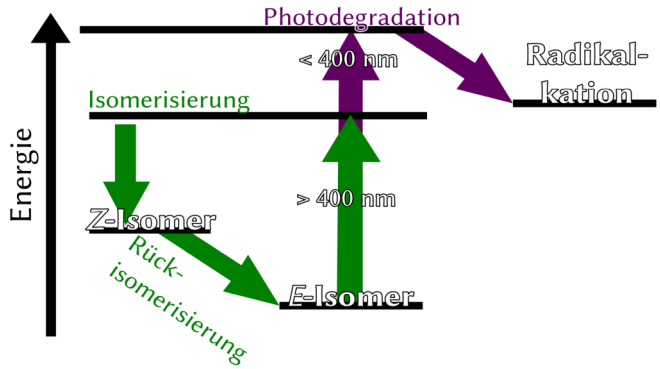

Abbildung 7.2: Graphische Zusammenfassung der Ergebnisse aus Kapitel 4. In Abhängigkeit von der Anregungswellenlänge können verschiedene Degradationspfade in einem konjugierten Iminpolymer addressiert werden.

isomeriert bei Raumtemperatur innerhalb weniger Sekunden zum ursprünglichen Polymer zurück.

Bestrahlung im UV-Bereich führte andererseits zu einer irreversiblen Degradierung des Polymers. Die Bestrahlung von Lösungen mit Chloroform als Lösungsmittel führte zur Bildung von Thiophen-Radikalkationen. Diese Zuordnung wird von spektroelektrochemischen Untersuchungen gestützt. In Toluol verringert sich bei Bestrahlung die Konjugation des Systems, was sich sowohl in der Abnahme der Absorption als auch der Blauverschiebung des Absorptionsmaximums ausdrückt. Der exakte Zerfallsmechanismus mit Hilfe transienter Absorption konnte nicht aufgeklärt werden, da die verwendete Anregungswellenlänge (403 nm) nicht genug Photonenenergie aufwies.

Im Schlusskapitel dieser Arbeit wurden Selbstheilungsexperimente Imin-basierter Polymere gezeigt (Abbildung 7.3). Der verwendete Reaktionsmechanismus basiert auf der Iminmetathese-Reaktion, bei welcher ein Substituentenaustausch an der Iminbindung erfolgt. In einem Experiment zur generellen Nutzbarkeit der Reaktion im Kontext konjugierter Polymere manifestierte sich der Komponentenaustausch in Form von neuen Absorptionsbanden im sichtbaren Teil des Spektrums, die auf die Bildung neuer Donor-Akzeptor-Systeme zurückzuführen sind. Diese Experimente wurden in essigsaurer Lösung, sowie im Film unter Essigsäure- und normaler Atmosphäre durchgeführt. Es zeigte sich, dass die Reaktion auch in Abwesenheit eines Säurekatalysators durch die Erhöhung der Reaktionstemperatur initiiert werden konnte, was für diese Reaktion bislang unbekannt war.

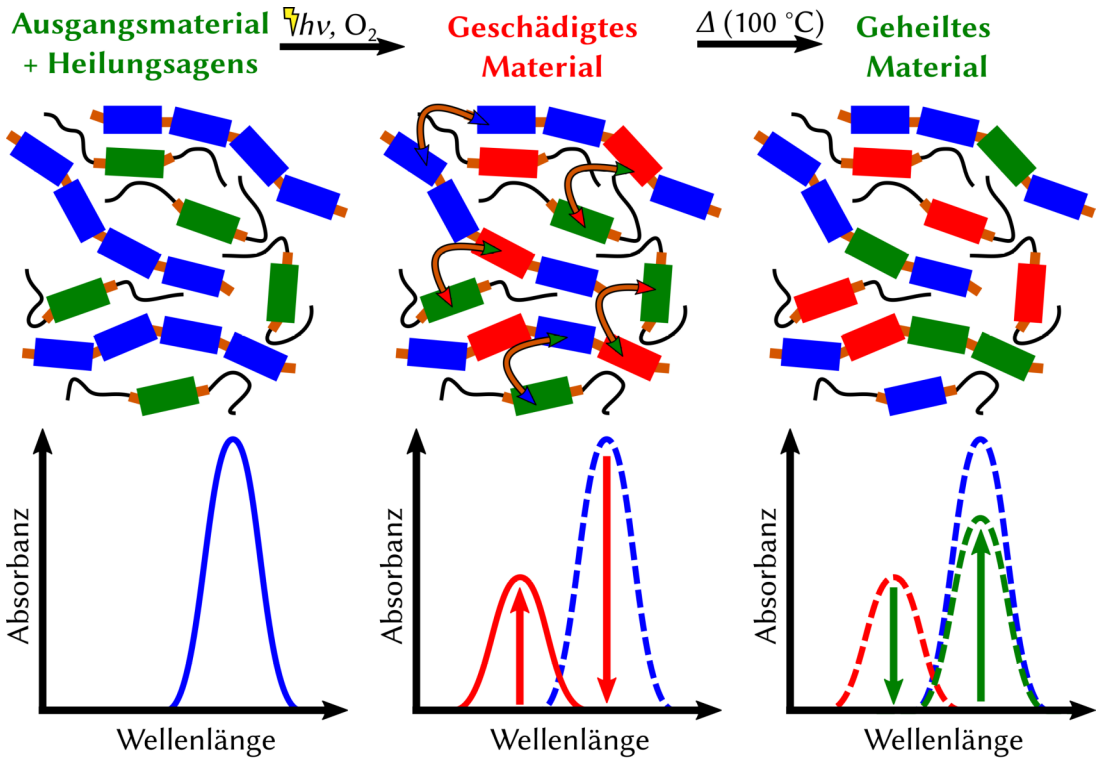

Abbildung 7.3: Graphische Zusammenfassung der Ergebnisse aus Kapitel 5. Ein Selbstheilungssystem das auf der Verwendung von Heilungsagenzien basiert, wurde entwickelt. Photogeschädigte Mischungen eines konjugierten Iminpolymers und den Heilungsagenzien zeigte eine Wiederherstellung der Absorbanz nach thermischer Behandlung.

Im Anschluss wurden Selbstheilungsexperimente, die auf der Iminmetathese-Reaktion basieren, entwickelt. Zunächst wurde nur ein kurzes konjugiertes Polymer durch Bestrahlung im Absorptionsmaximum beschädigt. Der Photoschaden des Materials, der hauptsächlich in der Dissoziation der Thiopheneinheiten bestand, zeigte sich als verringerte Absorption des Materials. Die thermische Behandlung der photogeschädigten Filme führte anschließend zu einer teilweisen Wiederherstellung der ursprünglichen Absorption mittels Iminmetathese. Ein größeres konjugiertes Polymer zeigte hingegen eine deutlich verringerte Selbstheilungseffizienz. Dies wird mit der eingeschränkten Mobilität der Chromophore im Film erklärt. Deshalb wurde dieses große Polymer mit kleineren Polymeren, welche nur einzelne Chromophore enthalten, gemischt. Diese Mischung zeigte erneut eine erhöhte Heilungseffizienz. Die hinzugefügten Polymere dienten somit als supramolekulare Heilungsagenzien. Eine Änderung der Heilungsagenzieneigenschaften, insbesondere ihre Glasübergangstemperatur und eine Erweiterung ihrer Absorption in den sichtbaren Teil des Spektrums, führte zu

nicht-heilenden Systemen. Basierend auf diesen Ergebnissen wurden allgemeine Prinzipien in der Entwicklung selbst-heilender optischer Materialien hergeleitet.

In dieser Arbeit wurden dynamisch-verknüpfte Polymere hinsichtlich ihrer optischen Eigenschaften untersucht. Die gezeigten Ergebnisse knüpfen unmittelbar an den aktuellen Stand der dynamischen und Selbstheilungschemie an und erweitern diese Bereiche um optoelektronische Materialien. Dies wird in der Folge den Weg für zukünftige, intelligente Materialien bereiten, beispielsweise selbstheilende organische Halbleiter.

Bibliography

[1] Rudolf Clausius. Ueber Verschiedene Für Die Anwendung Bequeme Formen Der Hauptgleichungen Der Mechanischen Wärmetheorie. *Ann. Phys.*, **1865**, *201*, 353–400.

[2] Matthews, R.A.J. The Science of Murphy's Law. *Sci. Am.*, **1997**, *276*, 88–91.

[3] Stone Age, Iron Age, Polymer Age. *J. Chem. Educ.*, **1986**, *63*, 743.

[4] Kumaraswamy, G. Living in the Polymer Age. *Resonance*, **2017**, *22*, 333–334.

[5] Maitz, M.F. Applications of Synthetic Polymers in Clinical Medicine. *Biosurface Biotribology*, **2015**, *1*, 161–176.

[6] Kaltenbrunner, M.; Sekitani, T.; Reeder, J.; Yokota, T.; Kuribara, K.; Tokuhara, T.; Drack, M.; Schwödiauer, R.; Graz, I.; Bauer-Gogonea, S.; Bauer, S.; Someya, T. An Ultra-Lightweight Design for Imperceptible Plastic Electronics. *Nature*, **2013**, *499*, 458–463.

[7] Jambeck, J.R.; Geyer, R.; Wilcox, C.; Siegler, T.R.; Perryman, M.; Andrady, A.; Narayan, R.; Law, K.L. Plastic Waste Inputs from Land into the Ocean. *Science*, **2015**, *347*, 768–771.

[8] Rochman, C.M.; Browne, M.A.; Halpern, B.S.; Hentschel, B.T.; Hoh, E.; Karapanagioti, H.K.; Rios-Mendoza, L.M.; Takada, H.; Teh, S.; Thompson, R.C. Classify Plastic Waste as Hazardous. *Nature*, **2013**, *494*, 169.

[9] Daniel Touger. Mass of All the People on Earth https://hypertextbook.com/facts/2006/DanielTouger.shtml (accessed Jul 9, 2018).

[10] Toshiko Kaneda; Carl Haub. How Many People Have Ever Lived on Earth? https://www.prb.org/howmanypeoplehaveeverlivedonearth/ (accessed Jul 9, 2018).

[11] Zwaag, S. van der. An Introduction to Material Design Principles: Damage Prevention versus Damage Management. In *Self Healing Materials*; Springer Series in Materials Science; Springer, Dordrecht, **2007**; pp. 1–18.

[12] Nosonovsky, M.; Rohatgi, P.K. Thermodynamic Principles of Self-Healing Metallic Materials. In *Biomimetics in Materials Science*; Springer Series in Materials Science; Springer, New York, NY, **2012**; pp. 25–51.

[13] Speck, T.; Luchsinger, R.; Busch, S.; Rüggeberg, M.; Speck, O. Self-Healing Processes in Nature and Engineering: Self-Repairing Biomimetic Membranes for Pneumatic Structures. In; WIT Press, **2006**; Vol. 1, pp. 105–114.

[14] Kalfas, I.H. Principles of Bone Healing. *Neurosurg. Focus*, **2001**, *10*, 1–4.

[15] Jackson, M.D.; Mulcahy, S.R.; Chen, H.; Li, Y.; Li, Q.; Cappelletti, P.; Wenk, H.-R. Phillipsite and Al-Tobermorite Mineral Cements Produced through Low-Temperature Water-Rock Reactions in Roman Marine Concrete. *Am. Mineral.*, **2017**, *102*, 1435–1450.

[16] Cremaldi, J.C.; Bhushan, B. Bioinspired Self-Healing Materials: Lessons from Nature. *Beilstein J. Nanotechnol.*, **2018**, *9*, 907–935.

[17] Diesendruck, C.E.; Sottos, N.R.; Moore, J.S.; White, S.R. Biomimetic Self-Healing. *Angew. Chem. Int. Ed.*, **2015**, *54*, 10428–10447.

[18] Bhushan, B. Biomimetics: Lessons from Nature–an Overview. *Philos. Trans. R. Soc. Lond. Math. Phys. Eng. Sci.*, **2009**, *367*, 1445–1486.

[19] Harrington, M.J.; Speck, O.; Speck, T.; Wagner, S.; Weinkamer, R. Biological Archetypes for Self-Healing Materials. In *Self-healing Materials*; Advances in Polymer Science; Springer, Cham, **2015**; pp. 307–344.

[20] Gurtner, G.C.; Werner, S.; Barrandon, Y.; Longaker, M.T. Wound Repair and Regeneration. *Nature*, **2008**, *453*, 314.

[21] Janis, J.E.; Harrison, B. Wound Healing: Part I. Basic Science. *Plast. Reconstr. Surg.*, **2014**, *133*, 199e–207e.

[22] Schrödinger, E. *What Is Life?: With Mind and Matter and Autobiographical Sketches*; Cambridge University Press, **1992**.

[23] Lipmann, F. Metabolic Generation and Utilization of Phosphate Bond Energy. *Adv Enzym. Relat Areas Mol Biol*, **1941**, *1*, 99–162.

[24] Transeau, E.N. The Accumulation of Energy by Plants. **1926**.

[25] Zhu, D.Y.; Rong, M.Z.; Zhang, M.Q. Self-Healing Polymeric Materials Based on Microencapsulated Healing Agents: From Design to Preparation. *Prog. Polym. Sci.*, **2015**, *49–50*, 175–220.

[26] Samadzadeh, M.; Boura, S.H.; Peikari, M.; Kasiriha, S.M.; Ashrafi, A. A Review on Self-Healing Coatings Based on Micro/Nanocapsules. *Prog. Org. Coat.*, **2010**, *68*, 159–164.

[27] Van Tittelboom, K.; De Belie, N.; Van Loo, D.; Jacobs, P. Self-Healing Efficiency of Cementitious Materials Containing Tubular Capsules Filled with Healing Agent. *Cem. Concr. Compos.*, **2011**, *33*, 497–505.

[28] Van Tittelboom, K.; De Belie, N. Self-Healing in Cementitious Materials—A Review. *Materials*, **2013**, *6*, 2182–2217.

[29] Grabowski, B.; Tasan, C.C. Self-Healing Metals. In *Self-healing Materials*; Advances in Polymer Science; Springer, Cham, **2016**; pp. 387–407.

[30] Dijk, N. van; Zwaag, S. van der. Self-Healing Phenomena in Metals. *Adv. Mater. Interfaces*, *0*, 1800226.

[31] Nosonovsky, M.; Amano, R.; M. Lucci, J.; K. Rohatgi, P. Physical Chemistry of Self-Organization and Self-Healing in Metals. *Phys. Chem. Chem. Phys.*, **2009**, *11*, 9530–9536.

[32] Nosonovsky, M.; Bhushan, B. Thermodynamics of Surface Degradation, Self-Organization and Self-Healing for Biomimetic Surfaces. *Philos. Trans. R. Soc. Lond. Math. Phys. Eng. Sci.*, **2009**, *367*, 1607–1627.

[33] Wool, R.P. Self-Healing Materials: A Review. *Soft Matter*, **2008**, *4*, 400–418.

[34] Yang, Y.; Urban, M.W. Self-Healing Polymeric Materials. *Chem. Soc. Rev.*, **2013**, *42*, 7446–7467.

[35] Yang, Y.; Urban, M.W. Thermodynamics of Self-Healing in Polymeric Materials. In *Healable Polymer Systems*; Polymer Chemistry Series; **2013**; pp. 126–148.

[36] Wang, Y.; Pham, D.T.; Zhang, Z.; Li, J.; Ji, C.; Liu, Y.; Leng, J. Sustainable Self-Healing at Ultra-Low Temperatures in Structural Composites Incorporating Hollow Vessels and Heating Elements. *Open Sci.*, **2016**, *3*, 160488.

[37] Yuan, Y.C.; Rong, M.Z.; Zhang, M.Q.; Chen, J.; Yang, G.C.; Li, X.M. Self-Healing Polymeric Materials Using Epoxy/Mercaptan as the Healant. *Macromolecules*, **2008**, *41*, 5197–5202.

[38] Pingkarawat, K.; Wang, C.H.; Varley, R.J.; Mouritz, A.P. Self-Healing of Delamination Cracks in Mendable Epoxy Matrix Laminates Using Poly[Ethylene-Co-(Methacrylic Acid)] Thermoplastic. *Compos. Part Appl. Sci. Manuf.*, **2012**, *43*, 1301–1307.

[39] Meure, S.; Wu, D.Y.; Furman, S. Polyethylene-Co-Methacrylic Acid Healing Agents for Mendable Epoxy Resins. *Acta Mater.*, **2009**, *57*, 4312–4320.

[40] Niu, G.; Guo, X.; Wang, L. Review of Recent Progress in Chemical Stability of Perovskite Solar Cells. *J. Mater. Chem. A*, **2015**, *3*, 8970–8980.

[41] Hintz, H.; Egelhaaf, H.-J.; Lüer, L.; Hauch, J.; Peisert, H.; Chassé, T. Photodegradation of P3HT–A Systematic Study of Environmental Factors. *Chem. Mater.*, **2011**, *23*, 145–154.

[42] Neugebauer, H.; Brabec, C.; Hummelen, J.C.; Sariciftci, N.S. Stability and Photodegradation Mechanisms of Conjugated Polymer/Fullerene Plastic Solar Cells. *Sol. Energy Mater. Sol. Cells*, **2000**, *61*, 35–42.

[43] Schaer, M.; Nüesch, F.; Berner, D.; Leo, W.; Zuppiroli, L. Water Vapor and Oxygen Degradation Mechanisms in Organic Light Emitting Diodes. *Adv. Funct. Mater.*, *11*, 116–121.

[44] Vitoratos, E.; Sakkopoulos, S.; Dalas, E.; Paliatsas, N.; Karageorgopoulos, D.; Petraki, F.; Kennou, S.; Choulis, S.A. Thermal Degradation Mechanisms of PEDOT:PSS. *Org. Electron.*, **2009**, *10*, 61–66.

[45] Brabec, C.J.; Hauch, J.A.; Schilinsky, P.; Waldauf, C. Production Aspects of Organic Photovoltaics and Their Impact on the Commercialization of Devices. *MRS Bull.*, **2005**, *30*, 50–52.

[46] Zhu, M.; Rong, M.Z.; Zhang, M.Q. Self-healing Polymeric Materials towards Non-structural Recovery of Functional Properties. *Polym. Int.*, **2014**, *63*, 1741–1749.

[47] Ahner, J.; Bode, S.; Micheel, M.; Dietzek, B.; Hager, M.D. Self-Healing Functional Polymeric Materials. In *Self-healing Materials*; Advances in Polymer Science; Springer, Cham, **2015**; pp. 247–283.

[48] Huynh, T.-P.; Sonar, P.; Haick, H. Advanced Materials for Use in Soft Self-Healing Devices. *Adv. Mater.*, *29*, 1604973.

[49] Ocheje, M.U.; Charron, B.P.; Nyayachavadi, A.; Rondeau-Gagné, S. Stretchable Electronics: Recent Progress in the Preparation of Stretchable and Self-Healing Semiconducting Conjugated Polymers. *Flex. Print. Electron.*, **2017**, *2*, 043002.

[50] Chen, J.; Huang, Y.; Ma, X.; Lei, Y. Functional Self-Healing Materials and Their Potential Applications in Biomedical Engineering. *Adv. Compos. Hybrid Mater.*, **2018**, *1*, 94–113.

[51] Tan, Y.J.; Wu, J.; Li, H.; Tee, B.C.K. Self-Healing Electronic Materials for a Smart and Sustainable Future. *ACS Appl. Mater. Interfaces*, **2018**, *10*, 15331–15345.

[52] Zhao, Y.; Wei, J.; Li, H.; Yan, Y.; Zhou, W.; Yu, D.; Zhao, Q. A Polymer Scaffold for Self-Healing Perovskite Solar Cells. *Nat. Commun.*, **2016**, *7*, 10228.

[53] Lang, F.; Nickel, N.H.; Bundesmann, J.; Seidel, S.; Denker, A.; Albrecht, S.; Brus, V.V.; Rappich, J.; Rech, B.; Landi, G.; Neitzert, H.C. Radiation Hardness and Self-Healing of Perovskite Solar Cells. *Adv. Mater.*, *28*, 8726–8731.

[54] Nie, W.; Blancon, J.-C.; Neukirch, A.J.; Appavoo, K.; Tsai, H.; Chhowalla, M.; Alam, M.A.; Sfeir, M.Y.; Katan, C.; Even, J.; Tretiak, S.; Crochet, J.J.; Gupta, G.; Mohite, A.D. Light-Activated Photocurrent Degradation and Self-Healing in Perovskite Solar Cells. *Nat. Commun.*, **2016**, *7*, 11574.

[55] Bode, S.; Enke, M.; Hernandez, M.; Bose, R.K.; Grande, A.M.; Zwaag, S. van der; Schubert, U.S.; Garcia, S.J.; Hager, M.D. Characterization of Self-Healing Polymers: From Macroscopic Healing Tests to the Molecular Mechanism. In

Self-healing Materials; Advances in Polymer Science; Springer, Cham, **2015**; pp. 113–142.

[56] Vega, J.M.; Grande, A.M.; van der Zwaag, S.; Garcia, S.J. On the Role of Free Carboxylic Groups and Cluster Conformation on the Surface Scratch Healing Behaviour of Ionomers. *Eur. Polym. J.*, **2014**, *57*, 121–126.

[57] Wu, D.Y.; Meure, S.; Solomon, D. Self-Healing Polymeric Materials: A Review of Recent Developments. *Prog. Polym. Sci.*, **2008**, *33*, 479–522.

[58] Geitner, R.; Legesse, F.-B.; Kuhl, N.; Bocklitz, T.W.; Zechel, S.; Vitz, J.; Hager, M.; Schubert, U.S.; Dietzek, B.; Schmitt, M.; Popp, J. Do You Get What You See? Understanding Molecular Self-Healing. *Chem. – Eur. J.*, *24*, 2493–2502.

[59] Zedler, L.; Hager, M.D.; Schubert, U.S.; Harrington, M.J.; Schmitt, M.; Popp, J.; Dietzek, B. Monitoring the Chemistry of Self-Healing by Vibrational Spectroscopy – Current State and Perspectives. *Mater. Today*, **2014**, *17*, 57–69.

[60] Geitner, R.; Kötteritzsch, J.; Siegmann, M.; Bocklitz, T.W.; Hager, M.D.; Schubert, U.S.; Gräfe, S.; Dietzek, B.; Schmitt, M.; Popp, J. Two-Dimensional Raman Correlation Spectroscopy Reveals Molecular Structural Changes during Temperature-Induced Self-Healing in Polymers Based on the Diels–Alder Reaction. *Phys. Chem. Chem. Phys.*, **2015**, *17*, 22587–22595.

[61] Geitner, R.; Kötteritzsch, J.; Siegmann, M.; Fritzsch, R.; Bocklitz, T.W.; Hager, M.D.; Schubert, U.S.; Gräfe, S.; Dietzek, B.; Schmitt, M.; Popp, J. Molecular Self-Healing Mechanisms between C60-Fullerene and Anthracene Unveiled by Raman and Two-Dimensional Correlation Spectroscopy. *Phys. Chem. Chem. Phys.*, **2016**, *18*, 17973–17982.

[62] Tepper, R.; Bode, S.; Geitner, R.; Jäger, M.; Görls, H.; Vitz, J.; Dietzek, B.; Schmitt, M.; Popp, J.; Hager, M.D.; Schubert, U.S. Polymeric Halogen-Bond-Based Donor Systems Showing Self-Healing Behavior in Thin Films. *Angew. Chem. Int. Ed.*, *56*, 4047–4051.

[63] Kupfer, S.; Zedler, L.; Guthmuller, J.; Bode, S.; Hager, M.D.; Schubert, U.S.; Popp, J.; Gräfe, S.; Dietzek, B. Self-Healing Mechanism of Metallopolymers Investigated by QM/MM Simulations and Raman Spectroscopy. *Phys. Chem. Chem. Phys.*, **2014**, *16*, 12422–12432.

[64] Ahner, J.; Pretzel, D.; Enke, M.; Geitner, R.; Zechel, S.; Popp, J.; Schubert, U.S.; Hager, M.D. Conjugated Oligomers as Fluorescence Marker for the Determination of the Self-Healing Efficiency in Mussel-Inspired Polymers. *Chem. Mater.*, **2018**, *30*, 2791–2799.

[65] Gupta, S.; Zhang, Q.; Emrick, T.; Balazs, A.C.; Russell, T.P. Entropy-Driven Segregation of Nanoparticles to Cracks in Multilayered Composite Polymer Structures. *Nat. Mater.*, **2006**, *5*, 229–233.

[66] Rifaie-Graham, O.; Apebende, E.A.; Bast, L.K.; Bruns, N. Self-Reporting Fiber-Reinforced Composites That Mimic the Ability of Biological Materials to Sense and Report Damage. *Adv. Mater.*, *30*, 1705483.

[67] Hu, M.; Peil, S.; Xing, Y.; Döhler, D.; Silva, L.C. da; Binder, W.H.; Kappl, M.; Bannwarth, M.B. Monitoring Crack Appearance and Healing in Coatings with Damage Self-Reporting Nanocapsules. *Mater. Horiz.*, **2018**, *5*, 51–58.

[68] Dahlke, J.; Zechel, S.; Hager, M.D.; Schubert, U.S. How to Design a Self-Healing Polymer: General Concepts of Dynamic Covalent Bonds and Their Application for Intrinsic Healable Materials. *Adv. Mater. Interfaces*, **2018**, *5*, 1800051.

[69] Roy, N.; Bruchmann, B.; Lehn, J.-M. DYNAMERS: Dynamic Polymers as Self-Healing Materials. *Chem. Soc. Rev.*, **2015**, *44*, 3786–3807.

[70] Lehn, J.-M. Supramolecular Chemistry - Scope and Perspectives Molecules - Supermolecules - Molecular Devices. In *Nobel Lectures in Chemistry 1981-1990*; World Scientific Publishing Co.: Singapore, **1993**.

[71] Lehn, J.-M. Dynamers: Dynamic Molecular and Supramolecular Polymers. *Prog. Polym. Sci.*, **2005**, *30*, 814–831.

[72] Ciferri, A. *Supramolecular Polymers*; CRC press, **2005**.

[73] Liu, Y.-L.; Chuo, T.-W. Self-Healing Polymers Based on Thermally Reversible Diels-Alder Chemistry. *Polym. Chem.*, **2013**, *4*, 2194–2205.

[74] Kötteritzsch, J.; Stumpf, S.; Hoeppener, S.; Vitz, J.; Hager, M.D.; Schubert, U.S. One-Component Intrinsic Self-Healing Coatings Based on Reversible Crosslinking by Diels-Alder Cycloadditions. *Macromol. Chem. Phys.*, **2013**, *214*, 1636–1649.

[75] Roy, N.; Lehn, J.-M. Dynamic Covalent Chemistry: A Facile Room-Temperature, Reversible, Diels–Alder Reaction between Anthracene Derivatives and N-Phenyltriazolinedione. *Chem. – Asian J.*, **2011**, *6*, 2419–2425.

[76] Craven, J.M. Cross-Linked Thermally Reversible Polymers Produced from Condensation Polymers with Pendant Furan Groups Cross-Linked with Maleimides. US3435003A, March 25, **1969**.

[77] Chen, X.X.; Wudl, F.; Mal, A.K.; Shen, H.B.; Nutt, S.R. New Thermally Remendable Highly Cross-Linked Polymeric Materials. *Macromolecules*, **2003**, *36*, 1802–1807.

[78] Chen, X.X.; Dam, M.A.; Ono, K.; Mal, A.; Shen, H.B.; Nutt, S.R.; Sheran, K.; Wudl, F. A Thermally Re-Mendable Cross-Linked Polymeric Material. *Science*, **2002**, *295*, 1698–1702.

[79] Klán, P.; Wirz, J. *Photochemistry of Organic Compounds: From Concepts to Practice*; John Wiley & Sons, **2009**.

[80] Ono, T.; Fujii, S.; Nobori, T.; Lehn, J.-M. Optodynamers: Expression of Color and Fluorescence at the Interface between Two Films of Different Dynamic Polymers. *Chem. Commun.*, **2007**, 4360–4362.

[81] Wojtecki, R.J.; Meador, M.A.; Rowan, S.J. Using the Dynamic Bond to Access Macroscopically Responsive Structurally Dynamic Polymers. *Nat. Mater.*, **2010**, *10*, 14.

[82] Braslavsky, S.E. Glossary of Terms Used in Photochemistry, 3rd Edition (IUPAC Recommendations 2006). *Pure Appl. Chem.*, **2007**, *79*, 293–465.

[83] Wöhrle, D.; Tausch, M.W.; Stohrer, W.-D. *Photochemie: Konzepte, Methoden, Experimente*; John Wiley & Sons, **2012**.

[84] Turro, N.J.; Ramamurthy, V.; Scaiano, J.C. *Principles of Molecular Photochemistry: An Introduction*; University Science Books, **2009**.

[85] Flynn, G.W.; Parmenter, C.S.; Wodtke, A.M. Vibrational Energy Transfer. *J. Phys. Chem.*, **1996**, *100*, 12817–12838.

[86] Schrader, B. *Infrared and Raman Spectroscopy: Methods and Applications*; John Wiley & Sons, **2008**.

[87] Thomas Elsaesser; Wolfgang Kaiser. Vibrational and Vibronic Relaxation of Large Polyatomic Molecules in Liquids. *Annu. Rev. Phys. Chem.*, **1991**, *42*, 83–107.

[88] Henry, W.; Coates, C.G.; Brady, C.; Ronayne, K.L.; Matousek, P.; Towrie, M.; Botchway, S.W.; Parker, A.W.; Vos, J.G.; Browne, W.R.; McGarvey, J.J. The Early Picosecond Photophysics of Ru(II) Polypyridyl Complexes: A Tale of Two Timescales. *J. Phys. Chem. A*, **2008**, *112*, 4537–4544.

[89] Benkö, G.; Kallioinen, J.; Korppi-Tommola, J.E.I.; Yartsev, A.P.; Sundström, V. Photoinduced Ultrafast Dye-to-Semiconductor Electron Injection from Nonthermalized and Thermalized Donor States. *J. Am. Chem. Soc.*, **2002**, *124*, 489–493.

[90] Dirac, P.A.M. The Quantum Theory of the Emission and Absorption of Radiation. *Proc. R. Soc. Lond. Ser. A*, **1927**, *114*, 243.

[91] Englman, R.; Jortner, J. The Energy Gap Law for Radiationless Transitions in Large Molecules. *Mol. Phys.*, **1970**, *18*, 145–164.

[92] Freed, K.F. Radiationless Transitions in Molecules. *Acc. Chem. Res.*, **1978**, *11*, 74–80.

[93] Mundt, R.; Villnow, T.; Ziegenbein, C.T.; Gilch, P.; Marian, C.; Rai-Constapel, V. Thioxanthone in Apolar Solvents: Ultrafast Internal Conversion Precedes Fast Intersystem Crossing. *Phys. Chem. Chem. Phys.*, **2016**, *18*, 6637–6647.

[94] Penfold, T.J.; Gindensperger, E.; Daniel, C.; Marian, C.M. Spin-Vibronic Mechanism for Intersystem Crossing. *Chem. Rev.*, **2018**.

[95] Strickler, S.J.; Berg, R.A. Relationship between Absorption Intensity and Fluorescence Lifetime of Molecules. *J. Chem. Phys.*, **1962**, *37*, 814–822.

[96] H. Kandori; Y. Shichida; T. Yoshizawa. Photoisomerization in Rhodopsin. *Biochem. Mosc.*, **2001**, *66*, 1197–1209.

[97] Ryseck, G.; Villnow, T.; Hugenbruch, S.; Schaper, K.; Gilch, P. Strong Impact of the Solvent on the Photokinetics of a 2(1H)-Pyrimidinone. *Photochem. Photobiol. Sci.*, **2013**, *12*, 1423–1430.

[98] Nome, R.A. Ultrafast Dynamics of Solvation: The Story so Far. *J. Braz. Chem. Soc.*, **2010**, *21*, 2189–2204.

[99] Bagchi, B.; Jana, B. Solvation Dynamics in Dipolar Liquids. *Chem. Soc. Rev.*, **2010**, *39*, 1936–1954.

[100] Horng, M.L.; Gardecki, J.A.; Papazyan, A.; Maroncelli, M. Subpicosecond Measurements of Polar Solvation Dynamics: Coumarin 153 Revisited. *J. Phys. Chem.*, **1995**, *99*, 17311–17337.

[101] Kasha, M. Characterization of Electronic Transitions in Complex Molecules. *Discuss. Faraday Soc.*, **1950**, *9*, 14–19.

[102] Stranius, K.; Börjesson, K. Determining the Photoisomerization Quantum Yield of Photoswitchable Molecules in Solution and in the Solid State. *Sci. Rep.*, **2017**, *7*, 41145.

[103] Salin, F. How to Manipulate and Change the Characteristics of Laser Pulses. In *Femtosecond Laser Pulses*; Advanced Texts in Physics; Springer, New York, NY, **2005**; pp. 175–194.

[104] Huber, R.; Satzger, H.; Zinth, W.; Wachtveitl, J. Noncollinear Optical Parametric Amplifiers with Output Parameters Improved by the Application of a White Light Continuum Generated in CaF2. *Opt. Commun.*, **2001**, *194*, 443–448.

[105] Ziolek, M.; Naskrecki, R.; Karolczak, J. Some Temporal and Spectral Properties of Femtosecond Supercontinuum Important in Pump–Probe Spectroscopy. *Opt. Commun.*, **2004**, *241*, 221–229.

[106] Rullière, C.; Amand, T.; Marie, X. Spectroscopic Methods for Analysis of Sample Dynamics. In *Femtosecond Laser Pulses*; Springer, Berlin, Heidelberg, **1998**; pp. 203–259.

[107] Ruckebusch, C.; Sliwa, M.; Pernot, P.; de Juan, A.; Tauler, R. Comprehensive Data Analysis of Femtosecond Transient Absorption Spectra: A Review. *J. Photochem. Photobiol. C Photochem. Rev.*, **2012**, *13*, 1–27.

[108] Kübel, J. Light-Induced Dynamics in Photoactive Metal Complexes with Secondary Chromophores. PhD Thesis, Jena, **2018**.

[109] B. Dietzek; T. Pascher; V. Sundström; A. Yartsev. Appearance of Coherent Artifact Signals in Femtosecond Transient Absorption Spectroscopy in Dependence on Detector Design. *Laser Phys. Lett.*, **2007**, *4*, 38.

[110] Loefroth, J.E. Time-Resolved Emission Spectra, Decay-Associated Spectra, and Species-Associated Spectra. *J. Phys. Chem.*, **1986**, *90*, 1160–1168.

[111] Berera, R.; van Grondelle, R.; Kennis, J.T.M. Ultrafast Transient Absorption Spectroscopy: Principles and Application to Photosynthetic Systems. *Photosynth. Res.*, **2009**, *101*, 105–118.

[112] Berlman, I.B. 4 - COMPOUNDS. In *Handbook of Fluorescence Spectra of Aromatic Molecules (Second Edition)*; Academic Press, **1971**; pp. 67–95.

[113] Adams, M.J.; Highfield, J.G.; Kirkbright, G.F. Determination of Absolute Fluorescence Quantum Efficiency of Quinine Bisulfate in Aqueous Medium by Optoacoustic Spectrometry. *Anal. Chem.*, **1977**, *49*, 1850–1852.

[114] Lakowicz, J.R. *Principles of Fluorescence Spectroscopy*; 3rd ed.; Springer: New York, **2006**.

[115] Porrès, L.; Holland, A.; Pålsson, L.-O.; Monkman, A.P.; Kemp, C.; Beeby, A. Absolute Measurements of Photoluminescence Quantum Yields of Solutions Using an Integrating Sphere. *J. Fluoresc.*, **2006**, *16*, 267–273.

[116] FluorTools. *DecayFit - Fluorescence Decay Analysis Software 1.4*; **2014**.

[117] Koti, A.S.R.; Krishna, M.M.G.; Periasamy, N. Time-Resolved Area-Normalized Emission Spectroscopy (TRANES): A Novel Method for Confirming Emission from Two Excited States. *J. Phys. Chem. A*, **2001**, *105*, 1767–1771.

[118] Bunz, U.H.F. Synthesis and Structure of PAEs. In *Poly(arylene etynylene)s: From Synthesis to Application*; Weder, C., Ed.; Springer Berlin Heidelberg: Berlin, Heidelberg, **2005**; pp. 1–52.

[119] Grimsdale, A.C. The Synthesis of Electroluminescent Polymers. In *Organic Light Emitting Devices*; Wiley-Blackwell, **2006**; pp. 215–243.

[120] Swager, T.M.; Zheng, J. Poly(Arylene Ethynylene)s in Chemosensing and Biosensing. In *Poly(arylene etynylene)s: From Synthesis to Application*; Weder,

C., Ed.; Advances in Polymer Science; Springer Berlin Heidelberg: Berlin, Heidelberg, **2005**; pp. 151–179.

[121] James, P.V.; Sudeep, P.K.; Suresh, C.H.; Thomas, K.G. Photophysical and Theoretical Investigations of Oligo(p-Phenyleneethynylene)s: Effect of Alkoxy Substitution and Alkyne–Aryl Bond Rotations. *J. Phys. Chem. A*, **2006**, *110*, 4329–4337.

[122] Chu, Q.; Pang, Y.; Ding, L.; Karasz, F.E. Synthesis, Chain Rigidity, and Luminescent Properties of Poly[(1,3-Phenyleneethynylene)-Alt-Tris(2,5-Dialkoxy-1,4-Phenyleneethynylene)]s. *Macromolecules*, **2002**, *35*, 7569–7574.

[123] Ahner, J.; Micheel, M.; Kotteritzsch, J.; Dietzek, B.; Hager, M.D. Thermally Triggered Optical Tuning of π-Conjugated Graft Copolymers Based on Reversible Diels-Alder Reaction. *RSC Adv.*, **2016**, *6*, 98221–98227.

[124] Breul, A.M.; Hager, M.D.; Schubert, U.S. Fluorescent Monomers as Building Blocks for Dye Labeled Polymers: Synthesis and Application in Energy Conversion, Biolabeling and Sensors. *Chem. Soc. Rev.*, **2013**, *42*, 5366–5407.

[125] Schäfer, J.; Breul, A.; Birckner, E.; Hager, M.D.; Schubert, U.S.; Popp, J.; Dietzek, B. Fluorescence Study of Energy Transfer in PMMA Polymers with Pendant Oligo-Phenylene-Ethynylenes. *ChemPhysChem*, **2013**, *14*, 170–178.

[126] Vieira, A.A.; Cristiano, R.; Bortoluzzi, A.J.; Gallardo, H. Luminescent 2,1,3-Benzothiadiazole-Based Liquid Crystalline Compounds. *J. Mol. Struct.*, **2008**, *875*, 364–371.

[127] Ricci, F.; Elisei, F.; Foggi, P.; Marrocchi, A.; Spalletti, A.; Carlotti, B. Photobehavior and Nonlinear Optical Properties of Push–Pull, Symmetrical, and Highly Fluorescent Benzothiadiazole Derivatives. *J. Phys. Chem. C*, **2016**, *120*, 23726–23739.

[128] Mundt, R.; Torres Ziegenbein, C.; Fröbel, S.; Weingart, O.; Gilch, P. Femtosecond Spectroscopy of Calcium Dipicolinate—A Major Component of Bacterial Spores. *J. Phys. Chem. B*, **2016**, *120*, 9376–9386.

[129] Duvanel, G.; Grilj, J.; Schuwey, A.; Gossauer, A.; Vauthey, E. Ultrafast Excited-State Dynamics of Phenyleneethynylene Oligomers in Solution. *Photochem. Photobiol. Sci.*, **2007**, *6*, 956–963.

[130] Sudeep, P.K.; James, P.V.; Thomas, K.G.; Kamat, P.V. Singlet and Triplet Excited-State Interactions and Photochemical Reactivity of Phenyleneethynylene Oligomers. *J. Phys. Chem. A*, **2006**, *110*, 5642–5649.

[131] Lessing, H.E.; Von Jena, A.; Reichert, M. Triplet Yield Determination and Heavy-Atom Effect from Ground-State Repopulation Kinetics. *Chem. Phys. Lett.*, **1976**, *42*, 218–222.

[132] Roy, K.; Kayal, S.; Ariese, F.; Beeby, A.; Umapathy, S. Mode Specific Excited State Dynamics Study of Bis(Phenylethynyl)Benzene from Ultrafast Raman Loss Spectroscopy. *J. Chem. Phys.*, **2017**, *146*, 064303.

[133] Roy, K.; Kayal, S.; Ravi Kumar, V.; Beeby, A.; Ariese, F.; Umapathy, S. Understanding Ultrafast Dynamics of Conformation Specific Photo-Excitation: A Femtosecond Transient Absorption and Ultrafast Raman Loss Study. *J. Phys. Chem. A*, **2017**.

[134] Breul, A.; Schäfer, J.; Pavlov, G.M.; Teichler, A.; Hoppener, S.; Weber, C.; Nowotny, J.; Blankenburg, L.; Popp, J.; Hager, M.D.; Dietzek, B.; Schubert, U.S. Synthesis and Characterization of Polymethacrylates Containing Conjugated Oligo(Phenylene Ethynylene)s as Side Chains. *J. Polym. Sci. Part -Polym. Chem.*, **2012**, *50*, 3192–3205.

[135] Winters, M.U.; Kärnbratt, J.; Eng, M.; Wilson, C.J.; Anderson, H.L.; Albinsson, B. Photophysics of a Butadiyne-Linked Porphyrin Dimer: Influence of Conformational Flexibility in the Ground and First Singlet Excited State. *J. Phys. Chem. C*, **2007**, *111*, 7192–7199.

[136] Toyota, S. Rotational Isomerism Involving Acetylene Carbon. *Chem. Rev.*, **2010**, *110*, 5398–5424.

[137] Lin, T.-S. EPR Measurements of the Phosphorescent State of 2,1,3-Benzothiadiazole. *Chem. Phys. Lett.*, **1976**, *43*, 338–343.

[138] Köhler, A.; Wilson, J.S.; Friend, R.H.; Al-Suti, M.K.; Khan, M.S.; Gerhard, A.; Bässler, H. The Singlet–Triplet Energy Gap in Organic and Pt-Containing Phenylene Ethynylene Polymers and Monomers. *J. Chem. Phys.*, **2002**, *116*, 9457–9463.

[139] Valeur, B.; Berberan-Santos, M.N. *Molecular Fluorescence: Principles and Applications*; Second.; Wiley-VCH Verlag GmbH & Co. KGaA: Weinheim, Germany, **2012**.

[140] Birnie, D.P. Rational Solvent Selection Strategies to Combat Striation Formation during Spin Coating of Thin Films. *J. Mater. Res.*, **2011**, *16*, 1145–1154.

[141] Bunz, U.H.F. Poly(Aryleneethynylene)s. *Macromol. Rapid Commun.*, **2009**, *30*, 772–805.

[142] Linnros, J.; Lalic, N.; Galeckas, A.; Grivickas, V. Analysis of the Stretched Exponential Photoluminescence Decay from Nanometer-Sized Silicon Crystals in SiO2. *J. Appl. Phys.*, **1999**, *86*, 6128–6134.

[143] Green, N.S.; Reisler, E.; Houk, K.N. Quantitative Evaluation of the Lengths of Homobifunctional Protein Cross-Linking Reagents Used as Molecular Rulers. *Protein Sci. Publ. Protein Soc.*, **2001**, *10*, 1293–1304.

[144] Nitao, L.K.; Reisler, E. Actin and Temperature Effects on the Cross-Linking of the SH1-SH2 Helix in Myosin Subfragment 1. *Biophys. J.*, **2000**, *78*, 3072–3080.

[145] Ying, H.; Zhang, Y.; Cheng, J. Dynamic Urea Bond for the Design of Reversible and Self-Healing Polymers. *Nat. Commun.*, **2014**, *5*, 3218.

[146] Jian, X.; Hu, Y.; Zhou, W.; Xiao, L. Self-Healing Polyurethane Based on Disulfide Bond and Hydrogen Bond. *Polym. Adv. Technol.*, **2018**, *29*, 463–469.

[147] Zechel, S.; Geitner, R.; Abend, M.; Siegmann, M.; Enke, M.; Kuhl, N.; Klein, M.; Vitz, J.; Gräfe, S.; Dietzek, B.; Schmitt, M.; Popp, J.; Schubert, U.S.; Hager, M.D. Intrinsic Self-Healing Polymers with a High *E*-Modulus Based on Dynamic Reversible Urea Bonds. *NPG Asia Mater.*, **2017**, *9*, e420.

[148] Li, M.; Zhang, R.; Li, X.; Wu, Q.; Chen, T.; Sun, P. High-Performance Recyclable Cross-Linked Polyurethane with Orthogonal Dynamic Bonds: The Molecular Design, Microstructures, and Macroscopic Properties. *Polymer*, **2018**, *148*, 127–137.

[149] Ahner, J.; Micheel, M.; Enke, M.; Zechel, S.; Schubert, U.S.; Dietzek, B.; Hager, M.D. Directed Orientation of Oligo(Phenylene Ethynylene)s Using Ureas or Urethanes in Rod–Coil Copolymers. *Macromol. Chem. Phys.*, **2017**, *218*, 1700343.

[150] McQuade, D.T.; McKay, S.L.; Powell, D.R.; Gellman, S.H. Indifference to Hydrogen Bonding in a Family of Secondary Amides. *J. Am. Chem. Soc.*, **1997**, *119*, 8528–8532.

[151] Ahner, J.; Micheel, M.; Geitner, R.; Schmitt, M.; Popp, J.; Dietzek, B.; Hager, M.D. Self-Healing Functional Polymers: Optical Property Recovery of Conjugated Polymer Films by Uncatalyzed Imine Metathesis. *Macromolecules*, **2017**, *50*, 3789–3795.

[152] Wei, Z.; Hai Yang, J.; Zhou, J.; Xu, F.; Zrínyi, M.; H. Dussault, P.; Osada, Y.; Mei Chen, Y. Self-Healing Gels Based on Constitutional Dynamic Chemistry and Their Potential Applications. *Chem. Soc. Rev.*, **2014**, *43*, 8114–8131.

[153] Kathan, M.; Kovaříček, P.; Jurissek, C.; Senf, A.; Dallmann, A.; Thünemann, A.F.; Hecht, S. Control of Imine Exchange Kinetics with Photoswitches to Modulate Self-Healing in Polysiloxane Networks by Light Illumination. *Angew. Chem. Int. Ed.*, **2016**, *55*, 13882–13886.

[154] Petrus, M.L.; Morgenstern, F.S.F.; Sadhanala, A.; Friend, R.H.; Greenham, N.C.; Dingemans, T.J. Device Performance of Small-Molecule Azomethine-Based Bulk Heterojunction Solar Cells. *Chem. Mater.*, **2015**, *27*, 2990–2997.

[155] Işık, D.; Santato, C.; Barik, S.; Skene, W.G. Charge-Carrier Transport in Thin Films of π-Conjugated Thiopheno-Azomethines. *Org. Electron.*, **2012**, *13*, 3022–3031.

[156] Sicard, L.; Navarathne, D.; Skalski, T.; Skene, W.G. On-Substrate Preparation of an Electroactive Conjugated Polyazomethine from Solution-Processable Monomers and Its Application in Electrochromic Devices. *Adv. Funct. Mater.*, **2013**, *23*, 3549–3559.

[157] Hindson, J.C.; Ulgut, B.; Friend, R.H.; Greenham, N.C.; Norder, B.; Kotlewski, A.; Dingemans, T.J. All-Aromatic Liquid Crystal Triphenylamine-Based Poly(Azomethine)s as Hole Transport Materials for Opto-Electronic Applications. *J. Mater. Chem.*, **2010**, *20*, 937–944.

[158] Sharma, G.D.; Sandogaker, S.G.; Roy, M.S. Electrical and Photoelectrical Properties of Poly(Phenyl Azomethine Furane) Thin Films Devices. *Thin Solid Films*, **1996**, *278*, 129–134.

[159] Lizin, S.; Passel, S.V.; Schepper, E.D.; Maes, W.; Lutsen, L.; Manca, J.; Vanderzande, D. Life Cycle Analyses of Organic Photovoltaics: A Review. *Energy Environ. Sci.*, **2013**, *6*, 3136–3149.

[160] Liu, R.S.; Asato, A.E. The Primary Process of Vision and the Structure of Bathorhodopsin: A Mechanism for Photoisomerization of Polyenes. *Proc. Natl. Acad. Sci.*, **1985**, *82*, 259–263.

[161] Berbasova, T.; Santos, E.M.; Nosrati, M.; Vasileiou, C.; Geiger, J.H.; Borhan, B. Light-Activated Reversible Imine Isomerization: Towards a Photochromic Protein Switch. *Chembiochem Eur. J. Chem. Biol.*, **2016**, *17*, 407–414.

[162] Lehn, J.-M. Conjecture: Imines as Unidirectional Photodriven Molecular Motors—Motional and Constitutional Dynamic Devices. *Chem. – Eur. J.*, **2006**, *12*, 5910–5915.

[163] Greb, L.; Eichhöfer, A.; Lehn, J.-M. Synthetic Molecular Motors: Thermal N Inversion and Directional Photoinduced C⌡N Bond Rotation of Camphorquinone Imines. *Angew. Chem. Int. Ed.*, **2015**, *54*, 14345–14348.

[164] Greb, L.; Lehn, J.-M. Light-Driven Molecular Motors: Imines as Four-Step or Two-Step Unidirectional Rotors. *J. Am. Chem. Soc.*, **2014**, *136*, 13114–13117.

[165] Barik, S.; Skene, W.G. Turning-on the Quenched Fluorescence of Azomethines through Structural Modifications. *Eur. J. Org. Chem.*, **2013**, *2013*, 2563–2572.

[166] Olmsted, J. Effect of Refractive Index on Molecular Radiative Lifetimes. *Chem. Phys. Lett.*, **1976**, *38*, 287–292.

[167] McHugh, A.J.; Gouterman, M. Oscillator Strengths for Electronic Spectra of Conjugated Molecules from Transition Gradients III. Polyacenes. *Theor. Chim. Acta*, **1969**, *13*, 249–258.

[168] Knox, R.S. Dipole and Oscillator Strengths of Chromophores in Solution ¶. *Photochem. Photobiol.*, **2003**, *77*, 492–496.

[169] Suzuki, K.; Kobayashi, A.; Kaneko, S.; Takehira, K.; Yoshihara, T.; Ishida, H.; Shiina, Y.; Oishi, S.; Tobita, S. Reevaluation of Absolute Luminescence Quantum Yields of Standard Solutions Using a Spectrometer with an Integrating Sphere and a Back-Thinned CCD Detector. *Phys. Chem. Chem. Phys.*, **2009**, *11*, 9850–9860.

[170] Montalti, M.; Credi, A.; Prodi, L.; Gandolfi, M.T. *Handbook of Photochemistry, Third Edition*; CRC Press, **2006**.

[171] Knöpke, L.R.; Spannenberg, A.; Brückner, A.; Bentrup, U. The Influence of Substituent Effects on Spectroscopic Properties Examined on Benzylidene Aniline-Type Imines. *Spectrochim. Acta. A. Mol. Biomol. Spectrosc.*, **2012**, *95*, 18–24.

[172] Chang-Shik Choi; Ki-Seok Jeon; Ki-Hwan Lee. Reversible Trans-Cis Photoisomerization of N,N'-Di(p-Methylaniline)Benzald-1,4-Diimine. *J. Photoscience*, **2005**, *12*, 135–136.

[173] Luo, Y.; Utecht, M.; Dokić, J.; Korchak, S.; Vieth, H.-M.; Haag, R.; Saalfrank, P. Cis–Trans Isomerisation of Substituted Aromatic Imines: A Comparative Experimental and Theoretical Study. *ChemPhysChem*, **2011**, *12*, 2311–2321.

[174] Guarìn, S.A.P.; Bourgeaux, M.; Dufresne, S.; Skene, W.G. Photophysical, Crystallographic, and Electrochemical Characterization of Symmetric and Unsymmetric Self-Assembled Conjugated Thiopheno Azomethines. *J. Org. Chem.*, **2007**, *72*, 2631–2643.

[175] Tsang, D.; Bourgeaux, M.; Skene, W.G. Demystifying the Triplet State and the Quenching Mechanism of Self-Assembled Fluorenoazomethines. *J. Photochem. Photobiol. Chem.*, **2007**, *192*, 122–129.

[176] Hill, M.G.; Mann, K.R.; Miller, L.L.; Penneau, J.F. Oligothiophene Cation Radical Dimers. An Alternative to Bipolarons in Oxidized Polythiophene. *J. Am. Chem. Soc.*, **1992**, *114*, 2728–2730.

[177] Zhang, Y.; Kupfer, S.; Zedler, L.; Schindler, J.; Bocklitz, T.; Guthmuller, J.; Rau, S.; Dietzek, B. In Situ Spectroelectrochemical and Theoretical Study on the

Oxidation of a 4H-Imidazole-Ruthenium Dye Adsorbed on Nanocrystalline TiO2 Thin Film Electrodes. *Phys. Chem. Chem. Phys.*, **2015**, *17*, 29637–29646.

[178] Berlin, A.; Grimoldi, S.; Zotti, G.; Osuna, R.M.; Ruiz Delgado, M.C.; Ortiz, R.P.; Casado, J.; Hernández, V.; López Navarrete, J.T. Synthesis and Characterization of a Novel Terthiophene-Based Quinodimethane Bearing a 3,4-Ethylenedioxythiophene Central Unit. *J. Phys. Chem. B*, **2005**, *109*, 22308–22318.

[179] Schnabel, W. Photodegradation of Polymers in Solution as Studied by Laser Flash Photolysis. *Polym. Eng. Sci.*, **1980**, *20*, 688–691.

[180] Tagawa, S.; Schnabel, W.; Washio, M.; Tabata, Y. Picosecond Pulse Radiolysis and Laser Flash Photolysis Studies on Polymer Degradation of Polystyrene and Poly-α-Methylstyrene. *Radiat. Phys. Chem. 1977*, **1981**, *18*, 1087–1095.

[181] Tagawa, S.; Schnabel, W. On the Mechanism of the Photolysis of Polystyrene in Chloroform Solution. Laser Flash Photolysis Studies. *Makromol. Chem. Rapid Commun.*, **1980**, *1*, 345–350.

[182] Shirota, Y. Organic Materials for Electronic and Optoelectronic Devices. *J. Mater. Chem.*, **2000**, *10*, 1–25.

[183] Sirringhaus, H.; Tessler, N.; Friend, R.H. Integrated Optoelectronic Devices Based on Conjugated Polymers. *Science*, **1998**, *280*, 1741–1744.

[184] Günes, S.; Neugebauer, H.; Sariciftci, N.S. Conjugated Polymer-Based Organic Solar Cells. *Chem. Rev.*, **2007**, *107*, 1324–1338.

[185] Coakley, K.M.; McGehee, M.D. Conjugated Polymer Photovoltaic Cells. *Chem. Mater.*, **2004**, *16*, 4533–4542.

[186] Domínguez, I.F.; Distler, A.; Lüer, L. Stability of Organic Solar Cells: The Influence of Nanostructured Carbon Materials. *Adv. Energy Mater.*, *7*, 1601320.

[187] Williams, K.A.; Boydston, A.J.; Bielawski, C.W. Towards Electrically Conductive, Self-Healing Materials. *J. R. Soc. Interface*, **2007**, *4*, 359–362.

[188] Blanksby, S.J.; Ellison, G.B. Bond Dissociation Energies of Organic Molecules. *Acc. Chem. Res.*, **2003**, *36*, 255–263.

[189] Ingold, C.K.; Piggott, H.A. CCCXVI.-The Additive Formation of Four-Membered Rings. Part II. The Conditions Which Confer Stability on the Dimethinediazidines. *J. Chem. Soc. Trans.*, **1923**, *123*, 2745–2752.

[190] Tóth, G.; Pintér, I.; Messmer, A. Mechanism of the Exchange Reaction of Aromatic Schiff Bases. *Tetrahedron Lett.*, **1974**, *15*, 735–738.

[191] Ciaccia, M.; Di Stefano, S. Mechanisms of Imine Exchange Reactions in Organic Solvents. *Org. Biomol. Chem.*, **2015**, *13*, 646–654.

[192] Burland, M.C.; Meyer, T.Y.; Baik, M.-H. Proton as the Simplest of All Catalysts for [2 + 2] Cycloadditions: DFT Study of Acid-Catalyzed Imine Metathesis. *J. Org. Chem.*, **2004**, *69*, 6173–6184.

[193] Brocks, G.; Tol, A. Small Band Gap Semiconducting Polymers Made from Dye Molecules: Polysquaraines. *J. Phys. Chem.*, **1996**, *100*, 1838–1846.

[194] van Mullekom, H.A.M.; Vekemans, J.A.J.M.; Havinga, E.E.; Meijer, E.W. Developments in the Chemistry and Band Gap Engineering of Donor–Acceptor Substituted Conjugated Polymers. *Mater. Sci. Eng. R Rep.*, **2001**, *32*, 1–40.

[195] Bourgeaux, M.; Skene, W.G. Photophysics and Electrochemistry of Conjugated Oligothiophenes Prepared by Using Azomethine Connections. *J. Org. Chem.*, **2007**, *72*, 8882–8892.

[196] Li, H.; Bai, J.; Shi, Z.; Yin, J. Environmental Friendly Polymers Based on Schiff-Base Reaction with Self-Healing, Remolding and Degradable Ability. *Polymer*, **2016**, *85*, 106–113.

[197] Kim, Y.H.; Park, J.H.; Lee, M.; Kim, Y.-H.; Park, T.G.; Kim, S.W. Polyethylenimine with Acid-Labile Linkages as a Biodegradable Gene Carrier. *J. Controlled Release*, **2005**, *103*, 209–219.

[198] Micheel, M.; Ahner, J.; Frey, M.; Neumann, C.; Hager, M.D.; Dietzek, B. Photophysics of a Bis-Furan-Functionalized 4,7-Bis(Phenylethynyl)-2,1,3-Benzothiadiazole: A Building Block for Dynamic Polymers. *ChemPhotoChem*, **2019**, *3*, 54–60.

Selbstständigkeitserklärung

Ich erkläre, dass ich die vorliegende Arbeit selbstständig und unter Verwendung der angegebenen Hilfsmittel, persönlichen Mitteilungen und Quellen angefertigt habe.

Mathias Micheel 29.07.2019 Jena . . . . . .

Appendix

Im Folgenden sind Änderungen der elektronisch und bei der Thulb eingereichten Fassung dieser Arbeit im Vergleich zur ursprünglich bewerteten Arbeit protokolliert. Alle Änderungen sind rein kosmetischer Natur und ändern nichts am Inhalt der Arbeit. Seitenzahlen beziehen sich auf die ursprüngliche Nummerierung der Arbeit in der eingereichten Fassung.

VII — Änderung der Literaturangaben zu Publikation 1 nach endgültiger Veröffentlichung. Dies betrifft auch Referenz 198 in der Bibliography. Einfügen eines Links zum ORCID-Profil des Autors.

S. 12 — Einzug am Seitenanfang entfernt.

S. 20 — Eq. 10 war fehlerhaft. Die ursprünglich angegebene Formel lautete:

$$\Phi_R = \frac{-m}{\varepsilon d}\frac{P\,\lambda_{ex}\,N_A}{h\,c_0\,V} \qquad \text{Eq. 10}$$

S. 22 — Eq. 11 war ein Duplikat von Eq. 13. Die ursprünglich angegebene Formel lautete:

$$M_{ij} = IRF \otimes \sum_n DAS_n \cdot \exp\left(-t_j/\tau_n\right) \qquad \text{Eq. 11}$$

S. 29 — Der Farbcode in Figure 3.2B wurde geändert, um mit dem in Figure 3.1 etablierten Farbcode übereinzustimmen. Die ursprüngliche Abbildung sah aus wie folgt:

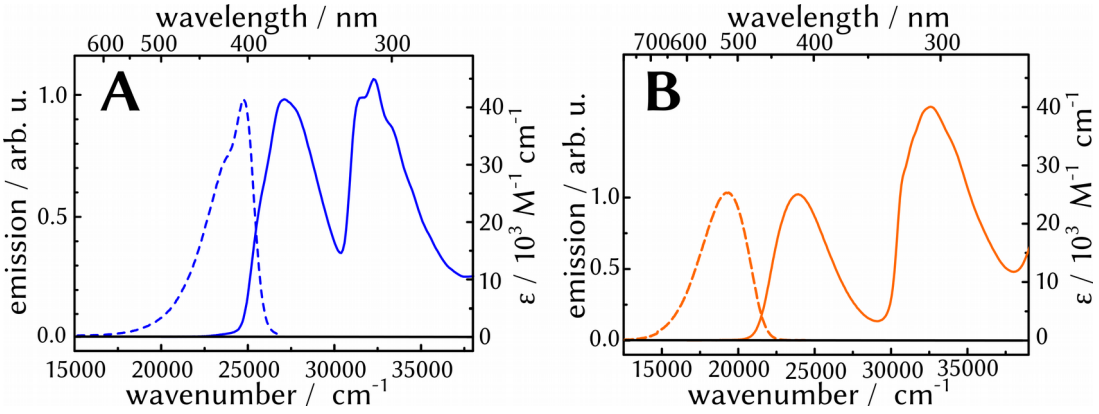

S. 33 — Verweis auf Figure 3.5 in Text eingefügt.

S. 34 Einzug am Seitenanfang entfernt. Verweis auf Figure 3.6A in Text eingefügt.

S. 35 Verweis auf Figure 3.6B in Text eingefügt.

S. 36/37 Einfügen eines geschützten Bindestrichs in “multi-exponential”.

S. 37 Im Einschub in Figure 3.7B waren die Datenpunkte für Dichlormethan (DCM) und Chloroform ($CHCl_3$) vertauscht. An der Schlussfolgerung, dass der Zusammenhang zwischen Emissionslebenszeit und Stokes-Verschiebung systematisch ist, ändert dies nichts. Die ursprüngliche Abbildung sah aus wie folgt:

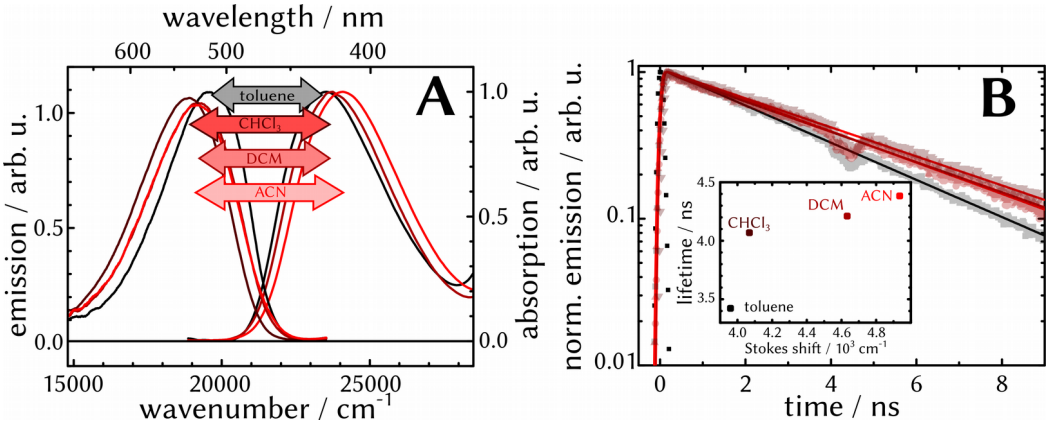

S. 39 Verweis auf Figure 3.9 in Text eingefügt.

S. 42 In Figure 3.11A wurde die Beschriftung einer Kurve von “A1-SC-P” zu “A1-MC-P” geändert. Die ursprüngliche Abbildung sah aus wie folgt:

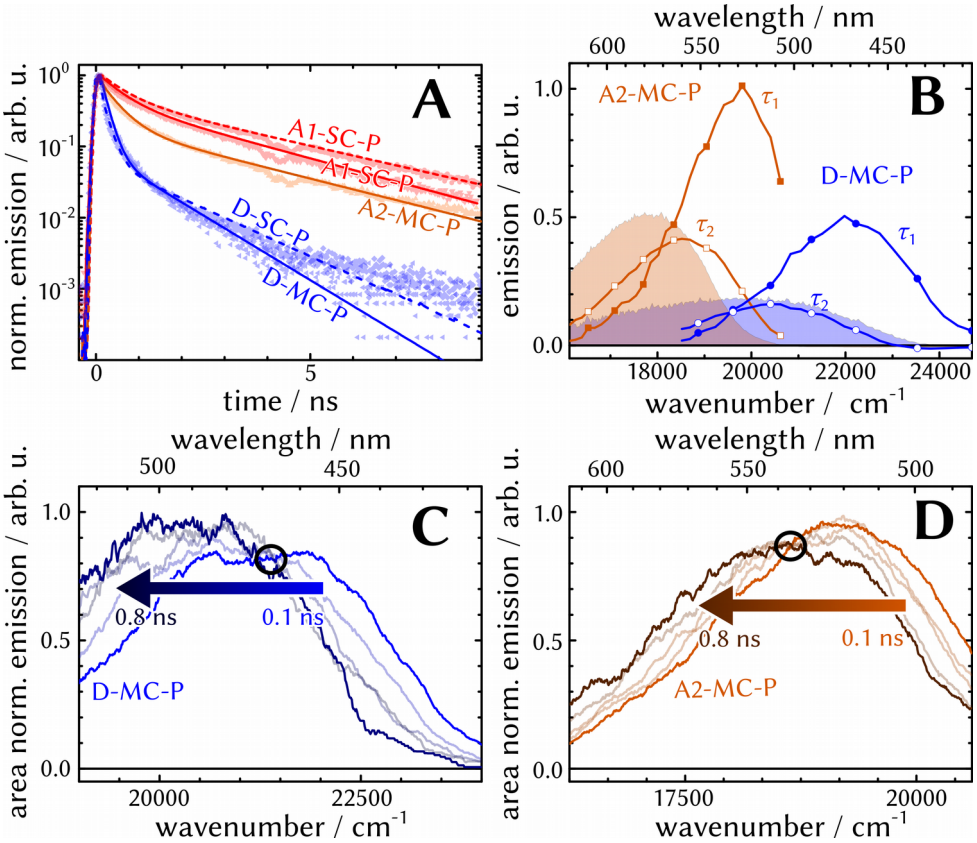

S. 43 Verweise auf Figure 3.12 und Figure 3.13 in Text eingefügt.

S. 45 Korrigierte Großschreibung. "… state. **T**he colors …"

S. 47 Verweis auf Figure 3.15 in Text eingefügt.

S. 49 Der Einschub aus Figure 3.16 wurde entfernt. Die ursprüngliche Abbildung sah aus wie folgt:

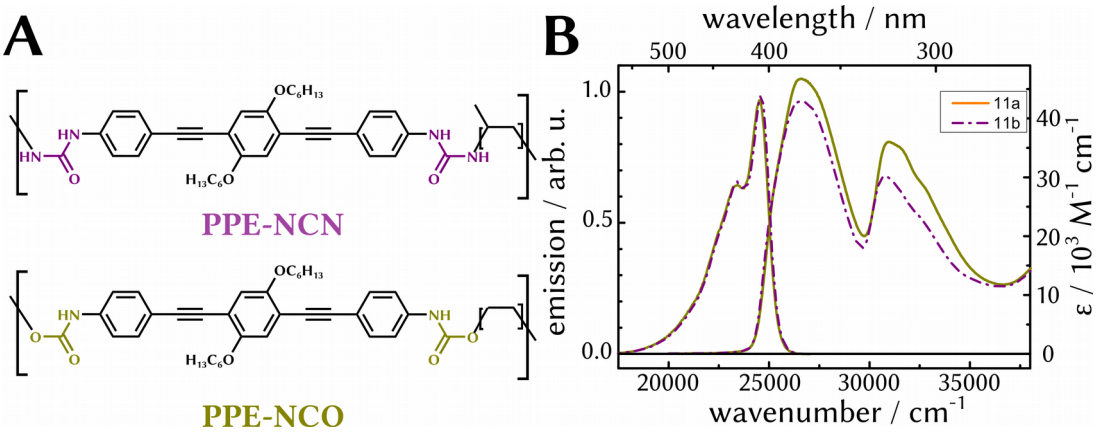

S. 66 In der Beschriftung zu Figure 4.9 wurde ein "of" eingefügt. "Comparison [of] absorbance …"

S. 87 In Abbildung 7.1C wurde der englische Begriff "Hetero-Dynamers" mit "Hetero-Dynamere" ersetzt.

S. 89 Im Original war Abbildung 7.2 komplett unübersetzt. Es wurde eine übersetzte Version eingefügt.

S. 110 Entfernung des Lebenslaufs.

neu Einführung eines Appendix.